Skoltech
Skolkovo Institute of Science and Technology

MACHINE LEARNING ENHANCEMENT OF MICRO-CT BASED MICROMECHANICS OF COMPOSITE MATERIALS

by Radmir KARAMOV

I hereby declare that the work presented in this thesis was carried out by myself as a part of the Agreement for Joint Supervision of Doctoral Student at Skolkovo Institute of Science and Technology, Moscow, and KU Leuven, Leuven, except where due acknowledgement is made, and has not been submitted for any other degree.

Radmir Karamov (Candidate)

Prof. Ivan Sergeichev (Supervisor, Skoltech)

Prof. Stepan Lomov (Supervisor, KU Leuven)

Prof. Yentl Swolfs (Co-supervisor, KU Leuven)

Acknowledgements

The thesis is the result of not only my efforts and hard work but also the invaluable contributions of numerous individuals. I am profoundly grateful to those who have played crucial roles in shaping this research.

First of all, I am deeply grateful for the invaluable guidance and supervision I received from my esteemed supervisors, Prof. Stepan Lomov, Prof. Ivan Sergeichev and Prof. Yentl Swolfs. Prof. Lomov's unwavering support and his role as my main source of knowledge and motivation have been crucial in my academic journey, encouraging me to work with a spark in my eyes. Prof Sergeichev, in addition to imparting knowledge in the field of research, has also shared valuable experiences that have significantly enriched my professional growth. Prof Swolfs has also given me a deep understanding of collaborative teamwork and how to excel in it. Also, I would like to thank Prof. Iskander Akhatov for his early guidance in my research. Each of them has played a unique and invaluable role in shaping my academic journey.

I would also like to express my gratitude to my fellow PhD students and researchers whose contributions have enriched this thesis. Kirill Minchenkov and Anastasiia Moskaleva broadened my research views through insightful discussions and fostering camaraderie. Stepan Konev and Boris Voloskov made invaluable contributions to mechanical testings of composite materials. Rui Guo's discussions during my academic trips to KU Leuven, especially in the context of machine learning, improved the quality of the developed algorithms. I am grateful for Thanasis Chatziathanasiou's work with KU Leuven's micro-CT system on my specimens. Christian Breite's engaging discussions on fibre break identification were valuable in improving the overall quality of the final chapter of this thesis.

Abstract

The development, design, and optimisation of composite materials require accurate material characterisation and modelling of their mechanical behaviour. Accurate models are critical to understanding how composite parts will behave in various structural applications. There are several techniques available for material characterisation and model building for finite element simulations. X-ray computed tomography has become popular in recent decades for obtaining experimental data in the form of three-dimensional images of the internal microstructure. However, CT imaging has some limitations. Images can have low contrast and artefacts, but the most important limitation is the trade-off between sample size and spatial resolution. The minimum size of a physical descriptor that can be distinguished is typically about 3-5 times larger than the pixel size. Therefore, to investigate small features such as carbon fibres or cracks, the sample must be smaller than 4mm. This requirement can be challenging when inspecting many types of composites as the specimen may be too large to meet this criterion.

To simulate the mechanical behaviour of composite materials, researchers use CT-based representative volume elements (RVE), which are small volumes capable of fully describing the material. However, one of the challenges of this approach is the handling of boundary conditions. Periodic boundary conditions (PBCs) are commonly used in simulations of various microstructures because they assume that the RVE is part of an infinite periodic lattice, which can help avoid boundary effects and reduce computational costs. However, using PBCs for RVEs obtained from experimental data, such as those from CT, can be challenging due to irregularities in the microstructure. If the RVE is too small, PBCs may introduce periodicity errors.

This thesis aims to address these challenges by developing, analysing, and verifying deep learning algorithms for CT image processing. This includes the development of algorithms for

structure generation and image quality enhancement, as well as the analysis of existing segmentation algorithms. The proposed algorithms will then be verified by generating periodic representative volumes of short fibre composites and enabling automated fibre break detection in unidirectional composites.

An inpainting generative adversarial neural network (GAN) was developed as a generation algorithm to generate missing regions in CT scans. Three encoder-decoder neural network architectures with different numbers of convolutional layers were developed and evaluated. The algorithms were able to accurately generate the missing parts based on known information about the microstructure of the material, as indicated by calculated physical and image-based metrics. As a result of the architecture comparison, the deepest neural network performed best, but consumed a large amount of GPU memory, making it unsuitable for inpainting large CT images.

A three-dimensional super-resolution deep learning algorithm has been developed to enhance the quality of CT images of composite materials. This algorithm employs techniques such as Enhanced Super-Resolution GAN and CycleGAN to not only improve the resolution of the images but also to replace denoising, contrast enhancement and other procedures that contribute to the overall image quality. By learning the relationship between high- and low-resolution images, the algorithm produces images with significantly improved visual precision of fibre and void boundaries and can improve the identification of physical parameters.

To improve the identification of physical descriptors of composite materials, deep learning, machine learning (ML) and non-ML techniques were compared for enhancing the segmentation quality of composite CT images. The segmentation tools were evaluated using both visual comparison and pixel accuracy metrics. The results showed that the deep learning segmentation algorithm was the most accurate tool with a fast execution time, although it requires GPU

hardware. In addition, the use of probability maps was introduced as a replacement for CT images, providing a more accurate form of material microstructure representation.

To demonstrate the potential of deep learning in the field of composites, a modified inpainting algorithm was used to generate periodic RVE of a short fibre composite. This was achieved by developing periodic layers and periodicity loss. Two finite element models were created based on the periodic RVE with voxel and tetrahedral meshes. The elastic behaviour of the models was simulated using PBC. It was found that the periodic RVE exhibited periodic behaviour at the boundaries, while the original RVE exhibited non-physical stress and strain fluctuations at the boundaries. In image-based simulation periodic boundaries cannot be accurately applied to the original RVE.

This research also presents a verification of the super-resolution algorithm. The algorithm was trained on high- and low-resolution scans of a carbon fibre composite and tested on a larger low-resolution image of another composite. The algorithm produces images with accurate fibre and void boundaries and enables automated identification of fibre breaks using void locations and fibre trajectories. The method can provide faster fibre break identification for strength models using low-resolution, in-situ CT scans.

This research demonstrates the potential of using deep learning methods to process CT images of composite materials. The algorithms developed are versatile and can be applied to a wide range of materials in various fields.

Samenvatting
Abstract

De ontwikkeling, het ontwerp en de optimalisatie van composietmaterialen vereisen nauwkeurige materiaalkarakterisering en modellering van hun mechanisch gedrag. Nauwkeurige modellen zijn van cruciaal belang om te begrijpen hoe composietonderdelen zich zullen gedragen in verschillende structurele toepassingen. Er zijn verschillende technieken beschikbaar voor materiaalkarakterisering en modelbouw voor eindige-elementensimulaties. X-stralen-computertomografie is de afgelopen decennia populair geworden voor het verkrijgen van experimentele gegevens in de vorm van 3D beelden van de interne microstructuur. CT-beeldvorming heeft echter enkele beperkingen. Afbeeldingen kunnen artefacten en een laag contrast hebben, maar de belangrijkste beperking is de interactie tussen monstergrootte en ruimtelijke resolutie. De minimale grootte van een fysieke kernmerk die kan worden onderscheiden, is doorgaans ongeveer 3-5 keer groter dan de pixelgrootte. Daarom moet het monster kleiner zijn dan 4 mm om kleine kenmerken zoals koolstofvezels of scheuren te onderzoeken. Deze vereiste kan een uitdaging zijn bij het inspecteren van composieten, aangezien het monster mogelijk te groot is om aan dit criterium te voldoen.

Om het mechanische gedrag van composietmaterialen te simuleren, gebruiken onderzoekers CT-gebaseerde representatieve volume-elementen (RVE), kleine volumes die het materiaal volledig kunnen beschrijven. Een van de uitdagingen van deze aanpak is echter het omgaan met randvoorwaarden. Periodieke randvoorwaarden (PRV's) worden vaak gebruikt in simulaties van verschillende microstructuren omdat ze ervan uitgaan dat de RVE deel uitmaakt van een oneindig periodiek rooster, wat grenseffecten kan helpen voorkomen en rekentijd kan

verlagen. Het gebruik van PRV's voor RVE's die zijn verkregen uit experimentele gegevens, zoals die van CT, kan echter een uitdaging zijn vanwege onregelmatigheden in de microstructuur. Als de RVE te klein is, kunnen PRV's periodiciteitsfouten introduceren.

Dit proefschrift heeft tot doel deze uitdagingen aan te pakken door deep learning-algoritmen voor CT-beeldverwerking te ontwikkelen, analyseren en verifiëren. Dit omvat de ontwikkeling van algoritmen voor het genereren van structuren en verbetering van de beeldkwaliteit, evenals de analyse van bestaande segmentatie-algoritmen. De voorgestelde algoritmen zullen vervolgens geverifieerd worden door periodieke RVE's van kortevezelcomposieten te genereren en geautomatiseerde vezelbreukdetectie in unidirectionele composieten mogelijk te maken.

Een inschilder generatief adversarieel neuraal netwerk (GAN) werd ontwikkeld als een generatiealgoritme om ontbrekende gebieden in CT-scans te genereren. Drie encoder-decoder neurale netwerken met verschillende aantallen convolutionele lagen werden ontwikkeld en geëvalueerd. De algoritmen waren in staat om de ontbrekende onderdelen nauwkeurig te genereren op basis van bekende informatie over de microstructuur van het materiaal, zoals aangegeven door berekende fysieke en op afbeeldingen gebaseerde statistieken. Het diepste neurale netwerk presteerde het beste, maar verbruikte een grote hoeveelheid GPU-geheugen, waardoor het ongeschikt was om grote CT-afbeeldingen in te schilderen.

Er werd een 3D superresolutie deep learning-algoritme ontwikkeld om de kwaliteit van CT-beelden van composietmaterialen te verbeteren. Dit algoritme maakt gebruik van technieken zoals Enhanced Super-Resolution GAN en CycleGAN om niet alleen de resolutie van de afbeeldingen te verbeteren, maar ook om ruisonderdrukking, contrastverbetering en andere procedures die bijdragen aan de algemene beeldkwaliteit te vervangen. Door de relatie tussen

afbeeldingen met een hoge en lage resolutie te leren, produceert het algoritme afbeeldingen met een aanzienlijk verbeterde visuele precisie van vezel- en porositeitsgrenzen en kan het de identificatie van fysieke parameters verbeteren.

Om de identificatie van fysieke kenmerken van composietmaterialen te verbeteren, werden deep learning, machine learning (ML) en niet-ML-technieken vergeleken om de segmentatiekwaliteit van composiet CT-beelden te verbeteren. De segmentatietools werden geëvalueerd met behulp van zowel visuele vergelijking als pixelnauwkeurigheidsstatistieken. De resultaten toonden aan dat het deep learning-segmentatie-algoritme de meest nauwkeurige tool was met een snelle uitvoeringstijd, hoewel het GPU-hardware vereist. Bovendien werd het gebruik van probabiliteitsskaarten geïntroduceerd als vervanging voor CT-beelden, waardoor een nauwkeurigere vorm van microstructuurrepresentatie werd verkregen.

Om het potentieel van deep learning op het gebied van composieten te demonstreren, werd een aangepast inschilder-algoritme gebruikt om periodieke RVE van een composiet met korte vezels te genereren. Dit werd bereikt door het ontwikkelen van periodieke lagen en periodiciteitsverlies. Er zijn twee eindige-elementenmodellen gemaakt op basis van de periodieke RVE met een voxel- en tetraëdrische mesh. Het elastische gedrag van de modellen werd gesimuleerd met behulp van PRV's. Er werd vastgesteld dat de periodieke RVE ook periodiek gedrag vertoonde aan zijn grenzen, terwijl de originele RVE niet-fysieke spannings- en rekfluctuaties vertoonde aan de grenzen. Dit suggereert dat periodieke grenzen niet nauwkeurig kunnen worden toegepast op de oorspronkelijke RVE.

Dit onderzoek presenteert ook een verificatie van het superresolutie-algoritme. Het algoritme is getraind op scans met hoge en lage resolutie van een koolstofvezelcomposiet en getest op een groter beeld met lage resolutie van een ander composiet. Het algoritme produceert beelden

met nauwkeurige vezel- en lege grenzen en maakt geautomatiseerde identificatie van vezelbreuken mogelijk met behulp van lege locaties en vezeltrajecten. De methode kan zorgen voor een snellere identificatie van vezelbreuken voor sterktemodellen met behulp van in-situ CT-scans met een lage resolutie.

Dit onderzoek demonstreert het potentieel van het gebruik van deep learning-methoden om CT-beelden van composietmaterialen te verwerken. De ontwikkelde algoritmen zijn veelzijdig en kunnen worden toegepast op een breed scala aan materialen op verschillende onderzoeksdomeinen.

Publications

1. Karamov R, Lomov S V, Sergeichev I, Swolfs Y, Akhatov I. Inpainting micro-CT images of fibrous materials using deep learning. Comput Mater Sci 2021;197:110551. https://doi.org/10.1016/j.commatsci.2021.110551.

2. Karamov R, Breite C, Lomov S V., Sergeichev I, Swolfs Y. Super-resolution processing of synchrotron CT images for automated fibre break analysis of unidirectional composites. Polymers 2023, 15(9), 2206. https://doi.org/10.3390/polym15092206.

Contents

XV

List of abbreviations

ANN – artificial neural network

BVP – boundary value problem

CT – computed tomography

DL – deep learning

FEA – finite element analysis

GAN – generative adversarial network

GPU – graphical processing unit

HR – high resolution

LR – low resolution

ML – machine learning

MSE – mean squared error

PBC – periodic boundary condition

PSNR – peak signal-to-noise ratio

ROI – region of interest

RVE – representative volume element

SSIM – structural similarity index measure

SGFC – short glass fibre composite

SRCT – synchrotron radiation computed tomography

UD – unidirectional

List of symbols

σ – stress tensor [Pa]

ε – strain tensor

L_{RVE} – characteristic size of representative volume element

R_{learn} – parametric reconstruction algorithm

θ – trainable parameter in neural networks

Θ – set of all trainable parameters

f – cost function to measure the error between the input and desired output

$g(\theta)$ – the regularisation function to prevent overfitting of trainable parameters

$D(\cdot)$ – output of discriminator network

$G(\cdot)$ – the generator network output

λ_{rec} – weight of reconstruction loss

λ_{adv} – weight of adversarial loss

L_{GAN} – total loss function of generative adversarial network

$\boldsymbol{p}$ – unit orientation vector

C_{ijkl} – stiffness tensor [Pa]

U_{ipq} – pseudo-displacement

$\sigma_{ij}^{(kl)}$ – pseudo-stress [Pa]

$\widehat{U}_j^k$ – reference point displacement

E_{ii} – elastic modulus [GPa]

ν_{ij} – Poisson ratio

G_{ij} – shear modulus [GPa]

List of figures

XIX

List of tables

Chapter 1. Introduction and motivation.

1.1 Composite materials

Composite materials are a class of heterogeneous materials which are formed by combining two or more distinct constituents. The goal of combining different materials into one is to use the unique properties of each constituent material to engineer a novel material with specific desired properties which could not be achieved with homogenous materials. Composite materials typically consist of two primary components: a matrix and reinforcements. The reinforcements are inclusions that impact strength and stiffness to the composite. The matrix functions as a continuous medium that facilitates the transmission of stresses and strains between the reinforcements, thereby binding the inclusions together. Depending on the desired properties of the composite, the type and material of the reinforcements can vary and may include unidirectional fibres, randomly oriented short fibres or particles composed of glass, carbon, or natural materials. An optimal selection of the reinforcement material, its type and volume fraction in combination with the matrix allows designing composites that meet specific application requirements for strength, stiffness, and weight. The high strength-to-weight ratio exhibited by fibre-reinforced polymer composites makes them particularly advantageous for use in aerospace and automotive applications. Furthermore, composite materials can offer environmental benefits, such as reduced fuel consumption and emissions due to lighter vehicles, and some composites are made from natural and renewable sources that can reduce the carbon footprint.

1.2 Microstructure of composites

The microstructure of composite materials, which refers to the distribution and arrangement of their constituents at the microscopic level, plays a crucial role in determining their properties. As composites are heterogeneous, their microstructure can have a significant impact on

various mechanical characteristics such as strength, stiffness, or toughness. For instance, composites reinforced with randomly oriented short fibres have very complex microstructures which are challenging to predict and analyse. Accurate determination of geometrical parameters such as orientation, volume fraction and distribution of reinforcing fibres and voids throughout the composite volume is critical for their characterisation. Similarly, analysis of textile composites requires knowledge of the unit cell parameters such as fabric wrinkles, resin pockets, delamination, debonding and other associated features. There are several experimental techniques for obtaining such parameters.

1.3 Micro-computed tomography.

X-ray computed tomography (CT) is one of the most widely used methods for the qualitative and quantitative assessment of the microstructure of composite materials. This non-destructive imaging technique uses a penetrating form of high-energy electromagnetic radiation to capture a sequence of object projections at multiple angles, and subsequently reconstructs a three-dimensional (3D) image of the object using computer algorithms. Modern lab-scale CT systems allow researchers to obtain high-resolution 3D images of material microstructures. The ability to perform non-destructive three-dimensional scanning is a key advantage of CT over other imaging techniques, such as optical microscopy and scanning electron microscopy, which are often destructive and limited to 2D imaging but may have higher resolution. While both lab CT and synchrotron radiation-based CT can provide 3D images of composites during mechanical or other experiments [1], synchrotron radiation-based CT has the advantage of providing even higher quality images due to its monochrome parallel beam. This allows in-situ analysis of defect evolution over time, including fibre breakage under tensile stress.

2

Despite its many advantages, CT has some limitations. One such limitation is the constant trade-off between resolution and specimen size: it is not feasible to acquire high-resolution 3D images of the internal structure of large specimens. Consequently, the resolution of CT images may not always be sufficient to identify microstructural descriptors within the large region of interest: the resolution of the 3D image is determined by the size of the X-ray beam and the resolution of the detector. In addition, acquiring high-resolution images can require a significant amount of scanning time. Another limitation of CT is the low contrast between fibres and matrix in certain composite materials, which makes it difficult to accurately distinguish between constituents.

CT images can be used to construct an accurate geometric representation of a material's microstructure. This geometry is used to generate representative volume elements, which are essential for finite element modelling to predict the properties and behaviour of materials.

1.4 Representative volume element

Representative volume elements (RVE) are small volumes that are able to fully characterize a given material. RVE are created using CT data to investigate the physical descriptors of composite materials and model their behaviour [2]. One approach to generating such models is using the retrieved geometric parameters to construct an RVE representing the structure of the material. Geometric modelling provides a relatively simple method of introducing an idealised microstructure morphology in the form of a repeating unit cell, where the microstructure is approximated as periodic: in periodic RVE structures, opposite faces match, allowing the application of periodic boundary conditions. The application of periodic boundary conditions results in a seamless transition from one side of the RVE to the other, effectively presenting a continuous microstructural replication. This design principle assumes that the inherent properties

3

and behaviour of the material exhibit periodicity. However, geometry-based models may lack important characteristics of the material, such as variations in material properties (e.g., random fibre packing, misaligned fibres or pronounced curvature) or defects introduced during manufacturing. An idealised geometric representation may not be sufficiently accurate to capture the natural behaviour of the material under real-world conditions.

As a result of these factors, data-driven models have gained increasing attention due to their ability to provide a more accurate representation of material microstructure (and corresponding behaviour) in comprehensive real-world situations [3]. However, data-driven models also have certain limitations: for instance, mathematically rigorous homogenisation requires the RVE to be represented as periodic, but the majority of microstructures observed in engineering materials are non-periodic and boundary stress and strain fluctuations may occur during their simulation. This presents difficulties in accurately applying periodic boundary conditions (PBC) to such data-driven models, as these materials lack the required periodicity. This research addresses this issue using machine and deep learning techniques.

1.5 Deep learning for CT image processing

Deep learning is a branch of machine learning that uses neural networks with a significant number of trainable parameters. In the field of image processing, convolutional layers can be used to enable the neural network to learn specific image features. Neural networks that consist of multiple hidden convolutional layers (i.e., deep neural networks) are capable of automatically extracting features and patterns from images and can effectively process complex image data. This methodology is suitable for a wide range of image processing tasks, including but not limited to image classification, image segmentation, object detection and image generation. Following the recent integration of three-dimensional convolutional operations into mainstream machine

4

learning frameworks, these techniques are increasingly being used to improve image quality and segmentation of CT images. However, the implementation of these techniques is still in development and deep learning is increasingly being applied to composite materials [4]. Figure 1 shows how the use of machine learning in composite materials has increased in recent years, thanks to significant advancements in the field of computer sciences. To effectively implement a deep learning model for CT image processing of composite materials, it is essential to have enough high-quality data and a neural network model architecture that can extract features relevant to the task from the microstructures of complex materials.
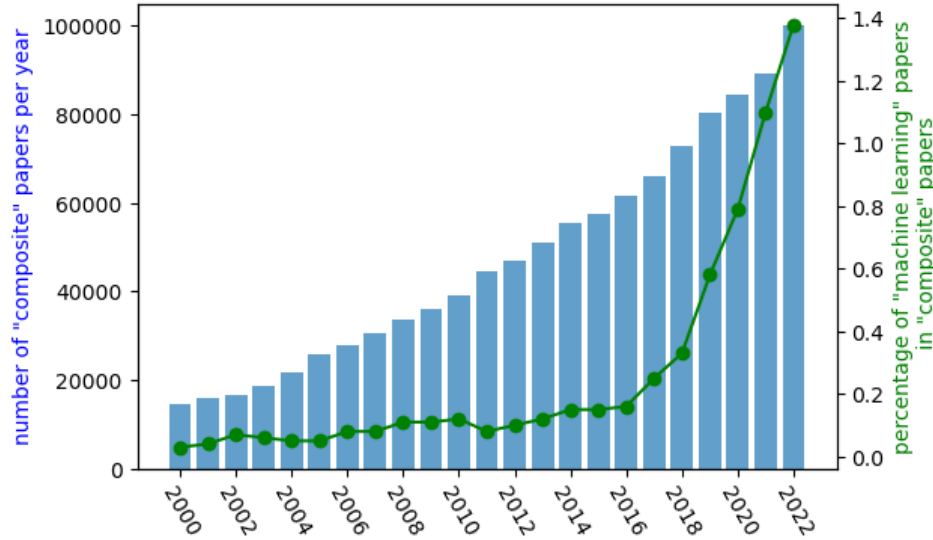
Figure 1 – Analysis of bibliographic data from the Scopus database using the search criteria 'composite* material*' (blue bars) and 'composite* material* and machine learning*'. The results (green line) are represented as a percentage (%) of the total number of papers on 'composite* material*' for each year

The main advantage of deep learning is that it can extract image features without requiring human intervention and can process substantial amounts of data at a faster rate to produce the desired results. It can also be used to generate accurate and fast three-dimensional images, which was previously unachievable. However, the use of deep learning requires a significant amount of training data, which can be a challenge when trying to generate data that does not exist in the real

world. In addition, the training process can be difficult and time-consuming, representing a drawback of this approach. Nevertheless, deep learning can perform CT image processing tasks more accurately and efficiently and even make previously unachievable procedures, such as image generation, possible.

1.6 Outline

The goal of this PhD thesis is to develop a methodology to implement machine learning techniques for CT imaging of composite materials to extract more accurate material descriptors and generate more robust RVEs for finite element modelling and mechanical property prediction. The research is focused on fibre-reinforced composite materials, including both short random and long unidirectional fibre composites. However, the methodology may apply to composites or heterogeneous materials in general. The work was motivated by deficiencies in the direct use of CT images for creation of digital twins of composite material using existing software such as VoxTex, Avizo or GeoDict. This study endeavours to prepare RVEs of composite materials by improving CT image quality, generating periodic structures and precisely segmenting fibres and matrices for a fast and correct assessment of physical descriptors, and accurate material assignment in subsequent finite element modelling.

The dissertation is organised as follows: Chapter 2 presents a literature review on methods and challenges of CT implementation for micromechanics of composites and how machine learning is used for heterogeneous materials investigation. Chapter 3 provides a concise but detailed problem statement of the PhD project. The materials and methods used in this work are described in Chapter 4, along with the resulting datasets used during the research. Chapter 5 provides a comprehensive description of the machine learning methods developed, as well as their validation. Chapter 6 is dedicated to the demonstration of the complete pipeline of RVE

preparation of short fibre composites for mechanical modelling using voxel-based and fibre identification approaches to predict their mechanical properties. Lastly, chapter 7 concludes the dissertation by summarising the achieved outcomes and discussing potential future developments.

Chapter 2. State of the art of micro-CT based mechanics and machine learning for composite materials.

Micromechanics is a field that helps to understand and predict the mechanical properties of composite materials by studying the properties of their constituents and their effect on the overall behaviour of the material. Homogenisation micromechanics makes it possible to understand how and to what extent local properties and constituent arrangements affect the macroscopic behaviour of materials, as well as the behaviour of complex structures made from such materials [5]. Analytical and numerical homogenisation methods can help to calculate various engineering properties of composite materials, such as stiffness, strength, and fracture toughness. These methods also allows the investigation of local properties such as stress/strain fields and damage initiation and development. This knowledge can then be used to design and optimise composite materials for various applications in a more cost-effective manner.

In the last few decades, numerical methods in particular have become widely used due to the large increase in available computing power and the development of specialised software packages. The numerical methods can handle complex geometries and nonlinearities but require mesh generation and can be computationally expensive when detailed structures or large deformations are analysed [6,7]. Numerical modelling is particularly useful when analysing data-driven geometries because of the complex structure of composites.

There are different levels of approximation of such structures: idealised geometry, data-driven geometry, and stochastic models when large variations in properties are taken into account. The most widely used approach to perform numerical mechanical simulation is to acquire a representative volume element of the material with some level of approximation [2], transform it into a finite element model and predict the effective properties of the material. This method is

supposed to be used when the composite material can be represented by an equivalent homogeneous material with the same mechanical properties as the material under investigation.

In recent years, machine learning techniques have also been used to predict the behaviour of composite materials or to complement existing solutions [8,9]. They can be used to directly predict mechanical properties or enable faster and more accurate computation. These methods are designed to reduce the need for expensive experiments to optimise or gain new insights for future composites. The state-of-the-art review of the investigated deep learning methods such as inpainting, super-resolution and segmentation will be discussed in detail in introductions to each developed method.

The focus of this chapter is to present an overview of current approaches to calculating effective properties of composite materials using X-ray computed tomography, and ways to perform CT-based simulations: current and upcoming methods and what challenges they experience. Firstly, the process of homogenization in micromechanics is introduced to make to facilitate further discussion. This chapter then discusses how to obtain data for this process and outlines CT-based model generation and its limitations. A brief but important discussion on boundary conditions is also provided. In the second part of the chapter, the role of machine learning in researching, designing, and optimizing composite materials is discussed.

2.1 Current challenges of X-ray computed tomography for micromechanics

2.1.1   Homogenization

Micromechanics involves the study of the properties of heterogeneous materials at both macroscopic and microscopic scales. The macroscopic description is used to calculate the effective properties of the material and the microscopic description scale covers the properties of its heterogeneities [5]. The homogenisation process is devoted to deriving a homogenised description

of the material at the macroscopic scale, based on the governing mass, momentum and energy conservation equations and laws, and the assumption that the volume of the studied material is statistically sufficient to capture the property distributions of the heterogeneous material. In a simple case with no rigid inclusions or voids, the homogenisation procedure which formulates a homogenised constitutive law in terms of averaged stress and strain can be described at any point in time by [5]:

$$\sigma_{ij}^h = \frac{1}{|V|} \int \sigma_{ij}^\mu dy = \langle \sigma_{ij}^\mu \rangle \tag{1}$$

and

$$\varepsilon_{ij}^h = \frac{1}{|V|} \int \varepsilon_{ij}^\mu dy = \langle \varepsilon_{ij}^\mu \rangle \tag{2}$$

where σ^h, ε^h are stress and strain tensors at the macroscopic scale L^M, σ^μ, ε^μ – stress and strain tensors at the microscopic scale L^μ, V is the volume under investigation. At a more general microscopic level, the problem is defined by the partial differential equations dictating momentum and energy, as well as the corresponding compatibility equations and constitutive law.

According to the review of Bostanabad et al [10] micromechanical models must have three main characteristics: firstly, the ability to incorporate complex microstructures with multiphase elements; secondly, the ability to utilise elastic, plastic, visco- and other constitutive relationships at the local phase level; and thirdly, the ability to provide closed-form constitutive equations for a range of mechanical multiaxial loads. As mentioned earlier, there are two main approaches to the creation of such mathematical models and their micromechanical analyses: analytical and numerical (computational).

The analytical methods [11] of obtaining effective properties for a material using mathematical formulae or models, such as Eshelby theory [12] and the Mori-Tanaka mean field

scheme [13], are in some cases based on assumptions and simplifications and are not always applicable to complex anisotropic composites [14]. The analytical methods should be used with caution: they have a high degree of approximation and may have constraints on inclusion shape, phase volume fraction and other physical descriptors, and may provide accurate results only when low volume fractions are considered [2,15].

Computational approaches use numerical methods such as finite element analysis to estimate the effective properties of heterogeneous materials of any size or geometry, but these methods can be computationally expensive, and some physical phenomena are difficult to model numerically due to their complexity and randomness.

2.1.2 X-ray computed tomography

The analytical and numerical approaches require data on the material microstructure or a reliable representative volume element. For analytical methods, physical descriptors should be provided: shape, size or orientation of inclusions for analytical solution [16], number of fibre breaks of unidirectional composite to predict its strength [17], etc. For numerical methods it is possible to create a full-size RVE knowing the physical descriptors with idealised microstructure [18–20], but in recent years a data-driven representation of the real microstructure is becoming more common [21,22]. There are several techniques to extract information about physical descriptors or internal microstructure. One of the most popular methods for acquiring this data is X-ray computed tomography [23–25].

X-ray CT is a unique imaging technique capable of providing reliable information on continuities, porosity, distribution, and other internal microstructural descriptors without destroying the specimen [23]. The method is based on obtaining 2D projections of the specimen at many different angles using penetrating, high-energy X-rays, and reconstructing a 3D image

using computational reconstruction of thousands of projections (Figure 2). The use of CT allows the complex composition and structure of composites to be investigated, often requiring 3D evaluation. Some CT systems (particularly synchrotron-based) can perform in-situ measurements: interrupted, involving pauses in the experiment for scanning, and uninterrupted (time-resolved), where scanning occurs continuously without experiment interruption; it is essential to understand the initiation and progression of defects to ensure the structural integrity of the composite. For more detailed information on the principles of how CT works and its implementations for materials science, the reader is referred to [26,27]. This section is dedicated to discussing the use of CT for imaging composite materials.
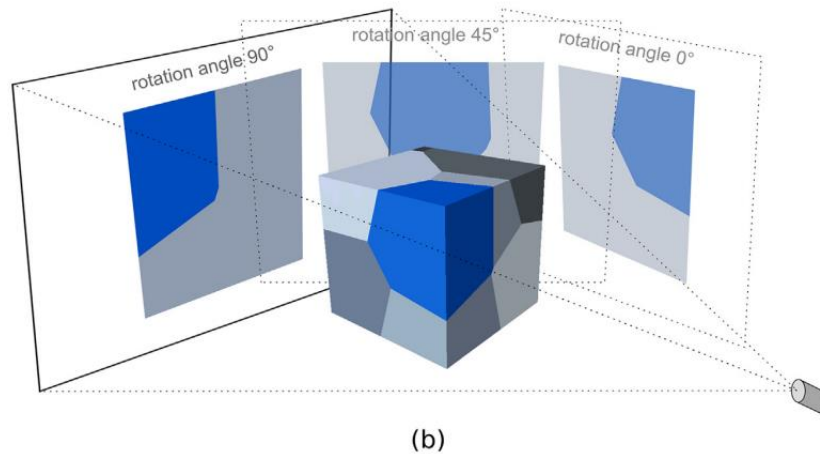
Figure 2 – Illustration of a process of CT acquiring material projections for further 3D image reconstruction (reprinted from [2])

Although CT has great advantages for 3D imaging of materials compared to two-dimensional techniques, it has crucial limitations that must always be taken into account [23]. The first limitation concerns image quality: image artefacts and low contrast. CT images may have low contrast between constituents, in our case between inclusions, defects (or damage) and matrix (Figure 3a). This may be the case if the constituents are made of materials with similar linear

attenuation coefficients. If low atomic number materials are used, there are limitations in the identification of fibre/matrix edges and small narrow defects [28,29]. Also, CT images of materials can have various artefacts that can affect the quality and accuracy of the images: beam hardening (Figure 3b), ring artefacts (Figure 3c), streak artefacts and noise.
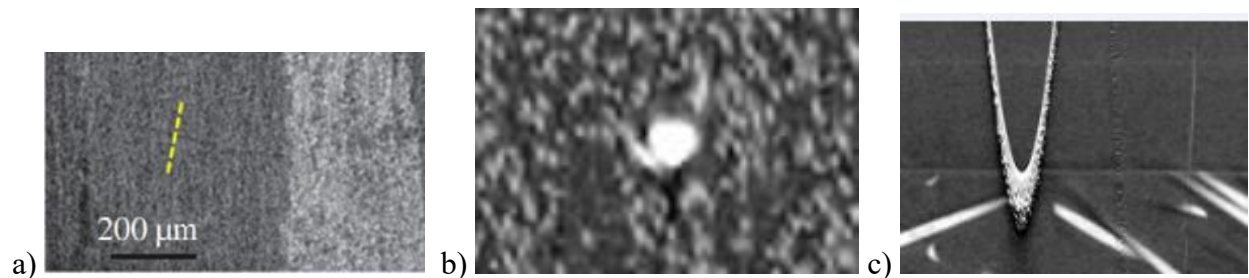
Figure 3 – Image quality related limitations of CT technique: a) low contrast between the matrix and crack introduces difficulties in crack identification (reprinted from [23] with Elsevier permission); b) beam hardening may appear at the end of fibres; c) ring artefacts due to specimen rotation.

The second limitation is a trade-off between sample size and spatial resolution, measured as the minimum distance between two points that can still be identified as separate entities. The spatial resolution affects the amount of image detail that can be distinguished: typically, the minimum size of an object that can be distinguished is about 3-5 times larger than the pixel size [30]. This limits the pixel size of the objects to be examined. However, the entire sample must be within the field of view of the detector for reconstruction. Considering the size limit of 2000-4000 pixels in one dimension, the sample size should be more than 1000-2000 times larger than the features of interest [23]. This introduces significant specimen size restriction for composite materials.

When small features are investigated (carbon fibres or cracks), the specimen usually must be smaller than few millimetres or even smaller, such a volume is justified for damage investigation, but extensive additional discussion is required to translate the properties of such specimens to the macroscopic properties of the material. This argument is particularly relevant for

woven textile composites, where the specimen may be too large to identify the physical descriptors [31] (e.g. pores within yarns may be indistinguishable). This also led to conclusion that it is not always possible to use CT imaging to examine specimens from standardised mechanical tests, where the specimen may be of much larger dimensions or low-resolution scans in an industrial environment.

2.1.3 Qualitative and quantitative assessments using CT imaging

CT techniques are used for both qualitative and quantitative assessments to understand the mechanics of composites, gain insight and obtain physical descriptors for analytical homogenisation models. The qualitative assessment allows researchers to investigate the presence of defects during manufacturing, inclusion interactions and the occurrence of damage during mechanical testing. For a more quantitative analysis, the CT images can be subjected to image processing to segment the objects of interest, and from the identified objects it is possible to obtain their attributes. The segmentation process is technically difficult and often requires human intervention. These issues are discussed in detail in chapter 5.3. By evaluating physical descriptors (Figure 4), it is possible to obtain information about fibres [32] (diameter, orientation, yarns in textile composite, etc.), manufacturing defects [33,34] (voids, fibre misalignment, etc.) and damage [35,36] (fibre breaks, matrix cracks, etc.).
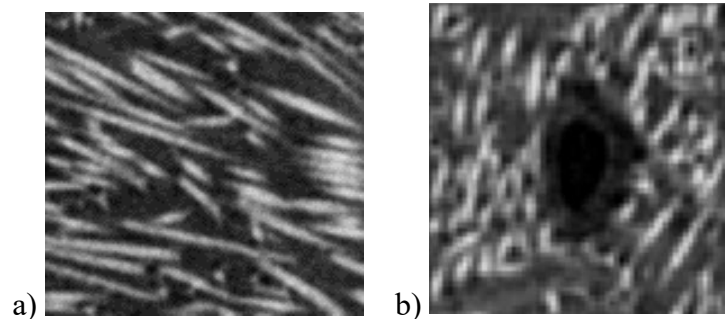
Figure 4 – CT representation of physical descriptors of composite materials: a) fibres in random short fibre composites; b) a void in a similar composite

There are methods to reliably identify fibres in each CT slice and to perform fibre tracking for individual fibre identification [22]. To perform such a procedure, the CT scan should be high resolution (HR), where the fibre diameter is equivalent to at least 5-10 pixels. For densely packed fibres in high fibre volume fraction composites, the process of segmentation is more difficult, but methods to extract information from such materials are already emerging [37,38]. While fibre orientation usually also requires HR images, statistical evaluation methods are available to extract information from grey scale gradients and calculate fibre orientation, for example using structure tensor analysis [39].

The more complex architecture of 2D or 3D textile composites is also assessed by CT [40] and the following physical descriptors are obtained: tow parameters, tow spacing, tow cross-sectional shape, etc. However, due to the trade-off between sample size and resolution, only mesoscale descriptors are usually used and fibre interactions within the tows are either assumed or calculated with other experiments [41]. Methods are being developed to detect flaws and calculate flaw population and damage distribution.

One of the current trends is the identification of fibre break development [42–44]. In these papers, the scanning is performed in situ using synchrotron light sources to obtain the highest quality CT images. The results obtained from these CT images are well received and can be used in damage development models, but some of the fibre breaks were identified manually, and the authors mention how time-consuming such a process can be. In other cases [23], some of the small defects cannot be properly detected again due to the resolution limitation, and also due to the low contrast, for example, mode II matrix cracks may have the same average grey scale values as the matrix.

Even with recent major advances in both laboratory-scale and synchrotron-based CT techniques, 3D images often cannot be produced with sufficient resolution for automated analysis of, for instance, fibre breaks [43].

2.1.4 RVE generation

The ability to obtain a highly detailed microstructure of a composite material leads to a different approach to micromechanics analysis by creating a 3D geometry for a representative volume element and applying numerical methods to predict its mechanical behaviour. X-ray CT techniques allow researchers not only to create a realistic numerical representation of the material, but also to calibrate and validate such models using the retrieved physical descriptors [23]. Due to the trade-off between resolution and sample size, it is more appropriate to analyse RVE at the mesoscale (tow level) and micro-scale (fibre level) than at the macroscale (specimen level).

In micromechanics, the RVE is a volume of material that is statistically representative enough to describe the effective behaviour of a heterogeneous material as a whole [2]. In general, the size of the RVE is scaled between its smallest physical descriptor (fibre or void) at the microscale and the characteristic size of the macroscale object, so it should satisfy the following condition: $L^{\mu} \ll L^{RVE} \ll L^{M}$, where L^{RVE} is characteristic size of RVE. It is important to discuss the RVE for each simulation individually. Computational homogenisation of RVEs can provide a local stress-strain field in the region of interest and also enables the investigation of damage and failure, which is not fully possible with analytical mean-field approaches.

There are two main approaches to selecting the RVE size: experimental and numerical. The experimental approach involves measuring the physical descriptors of the material to match the expected or observed microstructure. For computational homogenisation, it is not possible to specify in advance a specific RVE size that will be able to statistically correct the calculation of

effective properties. The numerical approach involves carrying out a convergence study [45–47]. During this study, the RVE size is incrementally increased, and the effective properties are calculated for each size until convergence is achieved. The minimum size that gives stable and consistent results can be considered the appropriate size for this material.

Approaches to RVE generation can be divided into three categories [2]:

1) data-driven generation from experimental characterisation of the microstructure [3,48,49], including data from CT imaging;

2) geometry-based methods [50,51], where the RVE is generated with idealised material morphology;

3) physics-based microstructure generation, where additional formation simulations are performed to obtain the RVE structure [52–54].

While the first approach provides a true, most accurate representation of the material's microstructure, 3D imaging techniques can introduce some inaccuracies (e.g., from CT artefacts), just like any other experimental measurement. In addition, a detailed representation can be computationally intensive, making it difficult to identify features of interest, and usually requires expensive equipment.

Geometry-based models are less detailed and may not account for all features of the real material, but they can be used extensively [55], for example when the material is still under development and experimental acquisition is not possible or too costly and time-consuming. Such models have been developed for a relatively long time and are already widely used for both predicting elastic properties and performing damage simulations (Figure 5). Physics-based models gave quite good results, but physics-based models require even higher computational power to calculate the physics: the kinematics of the deformations of tows as an example [54]. CT imaging

can also be used to calibrate and validate the second and third methods by measuring physical descriptors.
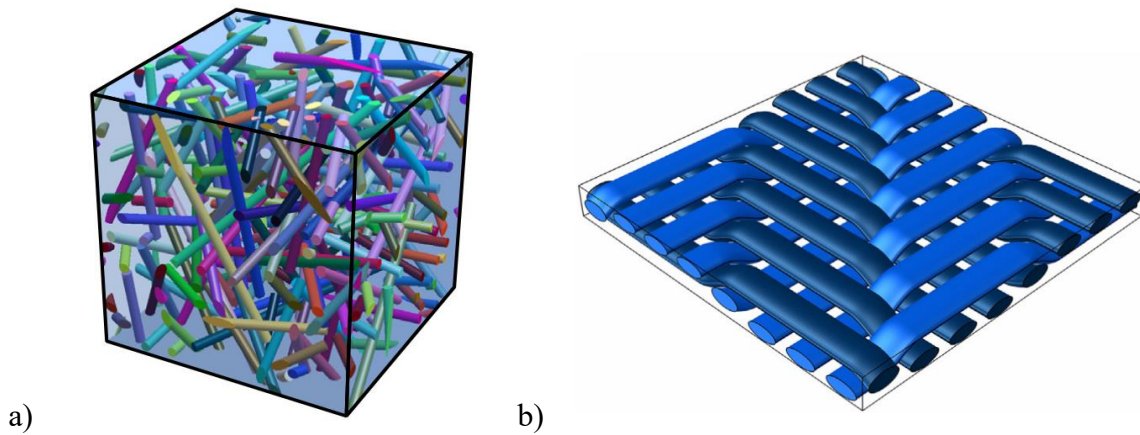
Figure 5 – RVE generated: a) cylindrical inclusions with a volume fraction of 10% (reprinted from [20]); b) with twill weave fabric (reprinted from [56]).

The data-driven approach has become increasingly popular in recent years, and the increasing availability of advanced imaging techniques has made the approach more feasible and cost-effective. For each composite material, an RVE should be generated according to its microstructure and mechanical properties obtained during experimental procedures. For example, a good development of the data-driven approach can be seen with mesoscale modelling [57] and microscale modelling of textile [58–60] or unidirectional (UD) composites [61].

A direct data-driven approach is presented by Madra et al. [21], where they transfer CT data to a finite element model by segmenting tows in images and section-by-section reconstruction of a 3D finite element model based on dual kriging as geometric interpolation (Figure 6a). There are also voxel-based data-driven models, which have also been used extensively and achieved good results: one of the methods to create voxel models was presented in [39]. Naouar et al. [3] investigate the use of CT scan in combination with voxel models to analyse textile composites and mesoscale (Figure 6b); with this method, the mechanical properties can be accurately analysed

with CT data. Their voxel model required a large number of elements to generate the model and limits damage simulation due voxel-based stress concentration, but the great advantage of voxel models is their easy mesh implementation.

a)   b)
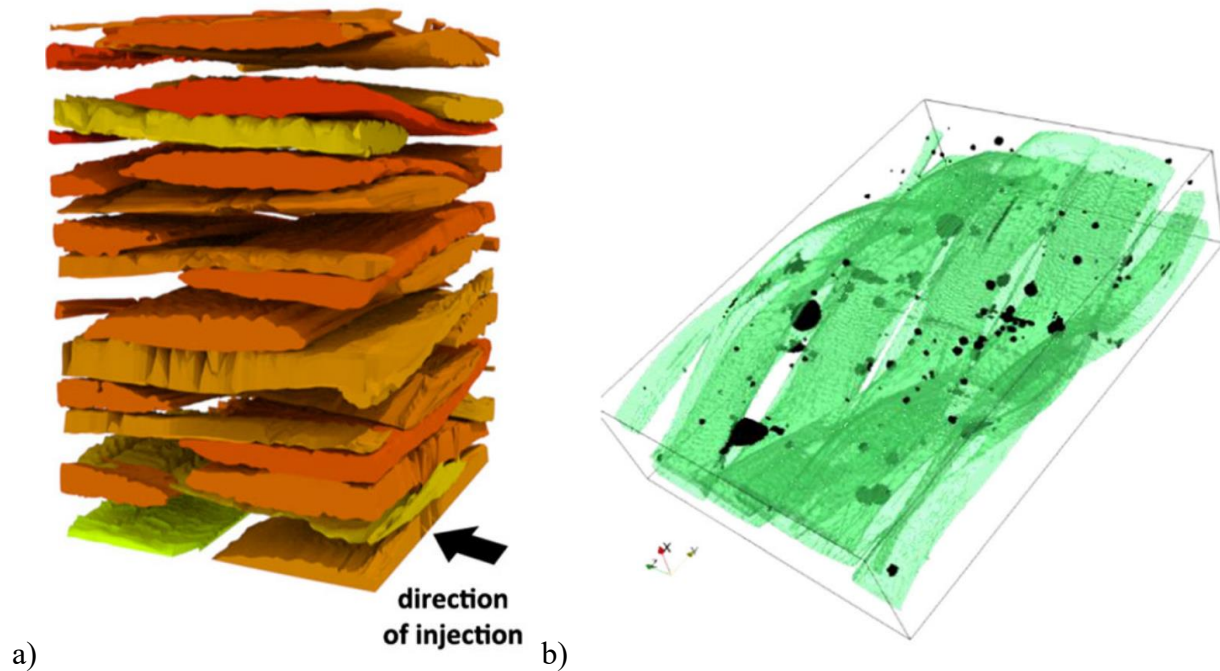
Figure 6 – Data-driven models: a) of woven reinforcements using kriging to smooth the outward surface of fibre tows [21]; b) of impregnated 3D warp interlock using structure tensor technique [3].

There are also CT applications for random short fibre composites. Mostly they face difficulties due to the microscale analysis requirements and the complex microstructure with considerable variation in fibre length and orientation in a material [62]. There are works on geometrical RVE generation, e.g. with RSA (random sequential adsorption) or similar methods, but they struggle to generate structures with high volume fraction [63]. Data-driven approaches have only been developed in the last few years. Hessman et al. [64] performed a comprehensive analysis of the internal microstructure of short glass fibre-reinforced thermoplastics by implementing an iterative single fibre segmentation and merging procedure. Mechanical properties of short basalt fibre-reinforced polyamide 6,6 composites were predicted by reconstructing a 3D

RVE with all composite components including fibres, matrix, and voids. Also, a comparison of analytical solutions and numerical schemes was carried out by [65] for predicting elastic properties of injection moulded short glass fibre reinforced thermoplastic composites, where they used finite element analysis of RVE with periodic boundary conditions as a reference.

2.1.5   Periodic boundary conditions

Another important issue to be addressed in the CT-based RVE simulation of composites is the application of appropriate boundary conditions, which require periodic microstructure (see Figure 7). The choice of boundary conditions must satisfy the Hill-Mandel condition [5,66] for correct homogenization. There are at least five boundary conditions that can satisfy the Hill-Mandel condition:

(1) fully prescribed deformation over the entire RVE;

(2) fully prescribed stress vectors over the entire RVE;

(3) prescribed deformation on the boundaries;

(4) prescribed stresses on the boundaries;

(5) periodic boundary conditions.

Kanit et al (2003) [47] found that the use of PBC leads to faster convergence when predicting effective properties, compared to Dirichlet and Neumann boundary conditions. Many researchers favour PBC for finite element analysis of models with complex microstructure [2,5,7,45,47,56,62,67–72]. However, such boundaries can be tedious to achieve and, in some cases, cannot be achieved due to the difficulties of RVE generation. For example, the use of PBC for CT-based RVE is considered almost impossible [2,23] because the natural structure does not have perfect periodicity, especially for random structures such as random fibre composites. Some works that criticise the use of perfect PBC: the process of applying such boundary conditions is a

cumbersome task as it is mentioned by Schneider et al. [73]. However, even in cases where other boundary conditions are applied, the authors try to use periodic structures in the comparison and advise the use of approximate periodic boundary conditions to avoid tedious PBC generation, as other boundary conditions may give overly stiff or overly soft responses.
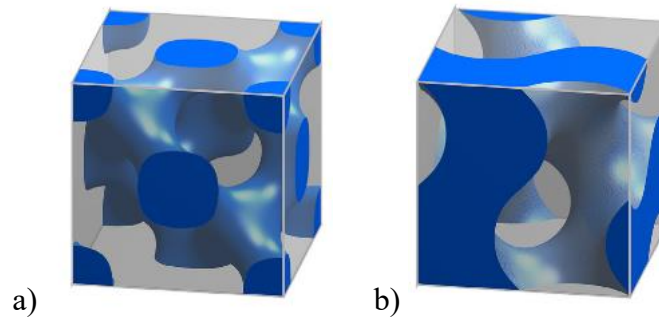
Figure 7 – Example of geometry based RVE with perfect periodicity enables applying PBC (reprinted from [2]): a) and b) surface-based bicontinuous composite microstructure.

There is also the problem of meshing such RVEs. The use of tetrahedral elements allows the discretisation of the most complicated structures but is more computationally expensive than hexahedral elements [74]. Neither element guarantees a perfectly periodic structure. An alternative approach is to use voxel discretisation, which is easy to generate, but is limited to accurate calculation of elastic properties only, since voxels produce non-physical stress concentrations, but they are ways to smooth these stress concentrations [75,76].

2.1.6 Segmentation of CT images of composite materials

One of the other problems researchers are struggling with is performing image segmentation (Figure 8) to accurately identify constituents and further assign properties for simulations [77–79]. Microscale modelling requires the segmentation of individual fibres, which is an additional challenge when using fine inclusions such as carbon fibres, which have relatively small fibre diameter and low contrast with the matrix. It is mentioned that the existing 2D

segmentation methods cannot be easily applied to 3D CT image [2,80]. However, the development of newer 3D tools is underway, including techniques based on machine learning [81–83].
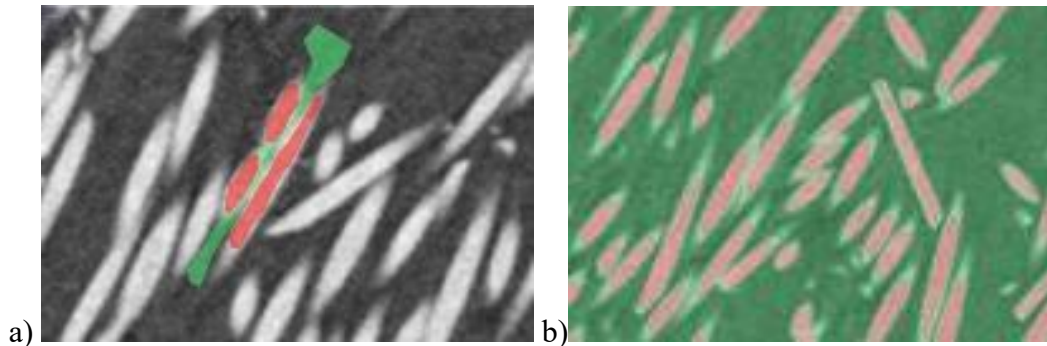
Figure 8 – Image segmentation of fibre in random short fibre composites using Weka segmentation software: a) training the algorithm; b) segmented image.

Overall, the researchers found a good correlation between the microstructure morphology of CT-based materials and their mechanical properties using homogenisation techniques [84].

2.2 Machine learning for heterogeneous materials investigation

Advances in computational power and technology have led to a rapid increase in the use of machine learning (ML) in various fields. This technology has also been significantly applied to computational materials science, including composites, in recent years [4,8,85–87]. Machine learning techniques are based on a complex set of algorithms that can improve themselves automatically and independently by learning data. As a result, ML algorithms can be used to perform tasks that involve making descriptive, predictive, or prescriptive decisions [88].

Machine learning algorithms can be divided into four categories based on their requirements for input and output data: supervised, unsupervised, semi-supervised and reinforcement learning. Supervised learning receives labelled training data and establishes a relationship between the input and output data [89], while unsupervised learning uses unlabelled data to discover patterns independently [90]. Semi-supervised learning combines both types of

data, and reinforcement learning uses input data from a dynamic environment to improve adaptation strategies [91].

Machine learning algorithms can also be broadly categorised into shallow learning and deep learning methods. Shallow learning methods include support vector machines, naive Bayes classifiers, decision trees, and simple artificial neural networks (ANN) [88]. The field in general leaning towards ANN because of its performance on large amounts of data, its ability to approximate complex relationships, and its access to advanced open-source libraries [92]. ANN aims to simulate the functioning of a human brain and its structure consists of input, hidden and output layers. Deep learning (DL) algorithms are based on ANN, but with significantly different structures within the hidden layers. There is a wide variety of deep learning architectures for different applications, such as convolutional neural networks (CNN) for image processing, recurrent neural networks (RNN) for sequential data processing, generative adversarial networks for data generation, and others [93].

Despite the very recent emergence of such methods, they have already applied for heterogeneous materials as aid for constitutive approaches [9] or in multiscale modelling, for mechanical properties prediction (homogenization).

2.2.1   Machine learning for constitutive laws

One of interesting approaches is discovering unknown constitutive laws, where ML based methods handle the increasing complexity of nonlinear mechanisms. Data-driven computational mechanics have been developed to construct predictive models directly from experimental material datasets, as it is shown in Figure 9 [8,9]. For example, Le et al. [94] presented a neural network-based approach for approximating the surface response of heterogeneous materials, which enables the determination of the corresponding effective potential, homogenized stress, and effective

tangent modulus at a macroscopic level. Yang et al [95] used a deep learning method that did not require detailed information on physical descriptors to predict the microscale elastic strain field within a 3D voxel-based microstructure of a two-phase composite. The outcomes revealed that deep learning techniques can learn important information about local neighbourhood details implicitly.
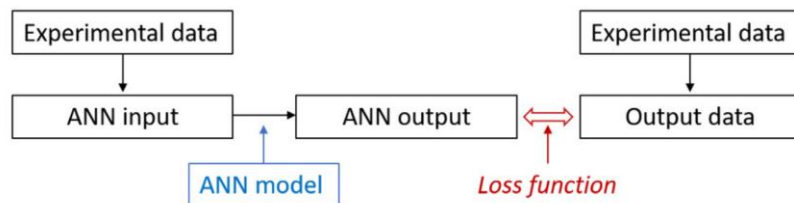
Figure 9 – Scheme of ANN usage for constitutive laws to predict mechanical properties of composite materials (reprinted from [8])

There are also few works devoted to the use of indirect data derived through physics-based models to train an ANN model for predicting mechanical properties. These methods have the advantage of obtaining more data from the same experiment and forcing the models to obey certain physical constraints. For example, in [96], Wang et al. proposed a novel approach that integrates supervised machine learning-based models with classical constitutive models to simulate porous materials associated with pores of different sizes, and the results showed significantly improved computational efficiency compared to conventional methods. However, there are still challenges in the approach to discovering unknown constitutive laws: lack of training data (a large number of full-scale mechanical tests are needed) and difficulties in coupling ML methods with mechanical models [97].

2.2.2   Machine learning for finite element analysis and representative volume generation

The second approach to using machine learning in composite micromechanics is to accelerate FEA by applying ML and DL models for numerical calculations. Generally, in this implementation, ANN models are trained on generated datasets and embedded in the FEA software to reduce the computation time. One of the works by Le et al. [98] performed several RVE analyses with periodic boundary conditions to generate training data for the construction of a constitutive model of nonlinear elastic material behaviour. The input parameters included macroscopic strains and certain microstructural properties, while the output was calculated as the effective potential of the composite obtained by homogenisation analysis. Studies of this approach vary in their use of machine learning varies to improve the accuracy and speed of finite element analysis, but the main challenge is that data generation and model training could be as time-consuming as the actual FEA. Also, there is no physical interpretability of the classical ML models [99].

There are also few ML techniques for generating new models or improving RVEs for numerical simulations and other analyses of heterogeneous materials. Chun et al. [100] presented a deep learning approach to generate ensembles of synthetic microstructures that can be used for simulations. The authors claim that they can control the micromechanical parameters of the generated RVEs by adjusting the input data. This stochastic RVE generation algorithm can be used for the statistical simulation of different loads. In a very recent work, Wei et al. [101] integrated a deep material network into FEA software for structural analysis of short fibre-reinforced composites. The network in this work recognises the characteristics of the studied material and transfers only essential morphologies in the finite element model. The method can generate accurate and efficient data-driven models and reduce computational time by orders of magnitude. Kamrava et al. [102] described a method for improving images of shale formations using a hybrid

approach that combines stochastic and deep learning algorithms. The presented method was able to improve the quality and accuracy of the images to better understand the characteristics of shale formations. Significant work has also been done by Mao et al. [103], where they acquire hundreds of periodic unit cells of a porous material using GAN (Figure 10), but this generation was only done for a 2D representation of the material due to data limitations.
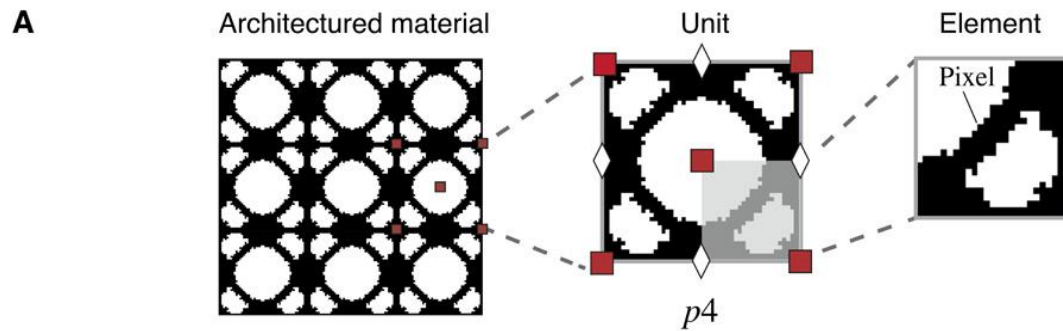
Figure 10 – Illustration of pixel-wise 2D RVE (unit cells) generated using GAN of architectured material (reprinted from [103])

2.2.3 Deep learning for image segmentation

As mentioned above, image segmentation is a crucial tool in the CT-based simulation of composite materials. Fibre detection in CT images is one of the major challenges in image processing. There are a handful of existing segmentation algorithms based on classical image processing. However, new algorithms based on deep learning are emerging [104,105], but have not yet been widely adopted for the analysis of heterogeneous materials.

There are few open sources and easy-to-use segmentation algorithms for two-dimensional images, including machine learning based [106] and deep learning based ones [107]. One of the exemplary 2D implementations was performed by Badran et al. [37]: phases in a ceramic unidirectional composite were successfully segmented slice by slice in CT images obtained during in-situ tensile loading of the composite (Figure 11). An example of 3D image segmentation is

given in [108], where the researchers used human-segmented tomograms to train a CNN to automatically detect sub-micron 3D features. They found that the trained model performed similarly or better than human detection due to the three-dimensionality of the algorithm, "machine-detected" human segmentation errors, and robustness to artefact-rich tomograms. It is worth mentioning that the author used a large database of human labelled data with about 65000 initial and segmented 2D images.
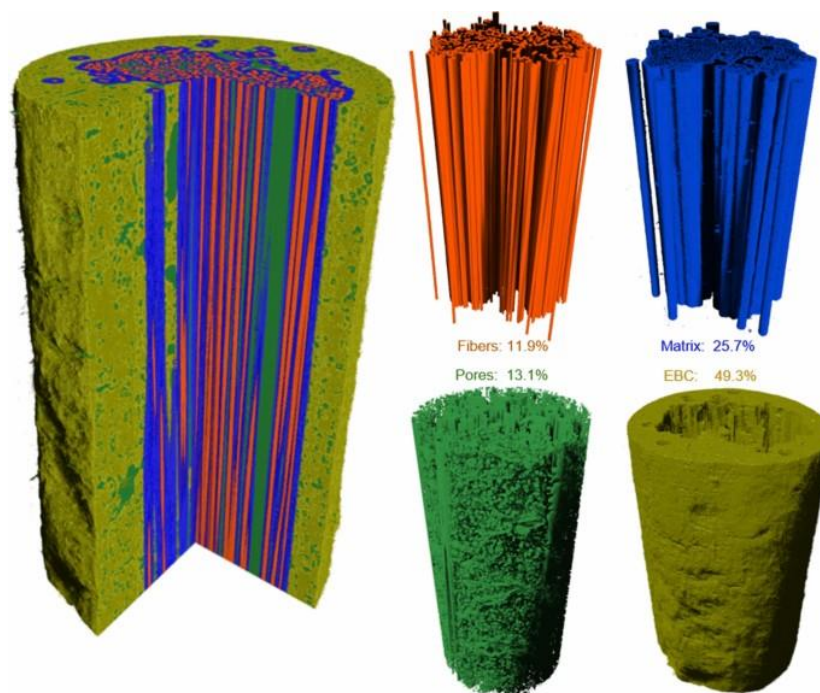
Figure 11 – Example of 3D image segmentation of SiC-SiC unidirectional composite using deep learning techniques [37]

Despite the high development of segmentation for 2D images of any application, including materials science, the field experiences a lack of easy-to-use and reliable 3D image segmentation software packages.

2.3 Summary

Data-driven approaches to calculating the mechanical properties of composite materials are becoming increasingly common. X-ray CT is one of the main imaging techniques used to acquire 3D data on the internal microstructure of heterogeneous materials. CT imaging can be used to obtain physical descriptors for analytical models and to construct an RVE for numerical simulations. However, CT imaging has limitations: low contrast for constituents with similar linear attenuation coefficients; possible image artefacts which may lead to difficulties in object identification; a trade-off between sample size and spatial resolution, which can limit the size of the sample to be investigated for composite materials.

There are geometric and physical approaches to generating RVEs based on an idealised analytical representation of material microstructure, but these models do not always incorporate essential features and can lead to inaccurate results. Data-driven models created from CT data can predict mechanical properties more accurately as they have a more detailed representation of the microstructure but can be time-consuming and computationally intensive.

One of the challenges of using RVEs for composite simulation is the application of periodic boundary conditions, which is not possible for real materials, which do not have perfect periodicity. The use of PBC is favoured by researchers because it leads to faster convergence and produces the most reliable results compared to other boundary conditions. Another challenge that remains is a fast and accurate segmentation algorithm for reliable object identification.

One of the technologies that can assist to solve these challenges is machine learning, which can be used as a highly advanced image processing tool. ML is already used not only for the prediction of mechanical properties of heterogeneous materials, but also for more difficult tasks such as microstructure feature detection, CT image segmentation and even stochastic RVE

generation. With its ability to learn from large datasets and make predictions based on patterns and trends, ML is becoming an increasingly popular tool in the field of materials science and engineering.

Chapter 3. Problem statement for the PhD research.

The existing literature highlights that the composite materials field is exploring the potential of using CT imaging for data-driven characterization of composite materials. But the field currently faces challenges related to the lack of tools to process CT data and generate periodic microstructures to apply periodic boundary conditions, which are required for modelling purposes. In addition, there are CT limitations due to the constant trade-off between specimen size vs. resolution and possible image artefacts. The goal of this PhD thesis is to develop methods for the analysis of X-ray CT images of composite materials to facilitate the prediction of their micromechanics. The research aims to incorporate image processing techniques based on machine and deep learning to develop generative, super-resolution methods and analyse segmentation algorithms to prepare RVEs for finite element models that predict effective mechanical properties.

The thesis presents a multi-step approach. The first step involves the acquisition of CT images of the materials, where possible image artefacts are removed and periodic RVE is generated. Super-resolution techniques can be used to improve the quality of the images. Segmentation algorithms are then used to identify the constituents of the composite. Finally, finite element models are generated from the segmented images to simulate the mechanical behaviour of the material under different loading conditions.

And the first objective of this research is to develop so-called inpainting techniques for 3D images of fibrous materials: generative algorithms that are capable of regenerating part of the input volume. Thereby the inpainting algorithm can be used to remove image artefacts and material defects in the 3D images. Additionally, these algorithms can be used to modify the representation of the material's microstructure, such as extending the input microstructure to create a periodic structure.

The second objective is to develop a super-resolution algorithm which allows a significant image quality enhancement of CT images. This algorithm aims to address the trade-off limitations of CT imaging techniques, where the acquisition of a larger region of interest typically results in reduced resolution and lower image quality. The algorithm allows the acquisition of larger regions of interest with less scanning time, but with similar image quality without introducing mechanical artefacts. The application of super-resolution algorithms for CT image quality improvement can lead to more accurate data analysis and modelling of composite materials.

The third objective is to analyse existing segmentation algorithms applicable to CT image processing. Reliable segmentation algorithms are important for the CT investigation of composite materials. They accurately isolate and identify different constituents of the material microstructure, such as fibres, matrix, and voids. Analysis of existing segmentation algorithms helps to select the most appropriate one for specific research objectives and CT imaging data. Accurate identification and analysis of the different components of composite materials are essential for the data-driven prediction of mechanical properties.

The fourth objective is to verify the deep learning algorithms. The development of a modified inpainting algorithm plays a crucial role in preparing periodic data-driven RVE from CT images of composite materials for finite element analysis. The main aim of this research component is to use the initial CT image of the material's microstructure and, while preserving its physical description, generate a larger volume to achieve an RVE with periodic microstructure. This approach allows the implementation of periodic boundary conditions in finite element analyses, which leads to faster convergence of the computations and more accurate calculations of effective properties.

By utilizing the developed super-resolution and existing machine learning segmentation algorithms, this research enables the development of automated algorithms for identifying fibre breaks in time-resolved synchrotron-based CT scans. Usually, identifying the objects of interest in low-resolution in-situ CT images required a time-consuming manual inspection process. The enabled automated algorithms would offer a faster and more efficient alternative for identifying fibre breaks, allowing researchers to analyse a larger volume of data in less time. This part of the research also introduces the possible adaptability of machine learning models, highlighting their capability to be trained and set up with one material and subsequently applied to another.

Overall, this research aims to push the boundaries of data-driven analysis and modelling of composite materials, with potential applications in the broader field of materials science and engineering: from an experimental investigation of various composite materials to advanced simulation techniques. The proposed methods are expected to provide a more accurate and efficient approach for analysing CT images of composite materials. This can have significant implications for designing and manufacturing composite structures, leading to more reliable and robust designs.

Chapter 4. Experimental equipment studied materials and datasets.

4.1 Materials

4.1.1   Short fibre composites

The material used to investigate the inpainting process is a random short glass fibre composite (SGFC) "Constaphtor 1000P", manufactured by the compression moulding process and supplied by "Constanta-2" Ltd, Volgograd, Russia. It consists of a polyphenylene sulphide matrix and has an average glass fibre length of 120 μm with an average fibre diameter of 17 μm. The material has an average fibre content of 32% by weight and a fibre volume fraction of 20%. The microstructure is random, and has no periodically repeating elements, which is the most challenging case for inpainting. The panel was manufactured in the shape of a flat, circular table measuring 30 cm in diameter.

The choice of a short-fibre composite with a relatively high fibre volume was motivated by the need to address the limitations of conventional methods, which struggle to generate RVEs with such high-volume fractions. Additionally, random fibre composite materials lack periodicity, making it exceedingly challenging to create accurate models for such composite materials.

A second short glass fibre composite "Constaphtor 1000C" was used for super-resolution and boundary condition generation. It was also supplied by "Constanta-2" Ltd, Volgograd, Russia, and was manufactured by injection moulding a mixture of POK M330 matrix (propene with carbon monoxide and ethene) and short fibres under pressure. The material has a fibre mass fraction of 25% or 14% by volume and the fibres are 250-400 μm long with a diameter of approximately 10-12 μm, these parameters were measured by the manufacturer. This material was also a panel made in the shape of a flat, circular table measuring 30 cm in diameter.

The 1000C material has been characterised by mechanical testing for another project in Skoltech by Stepan Konev. A total of 10 plates were subjected to analysis, with each plate providing one specimen for tensile, shear, and flexural testing. Due to the circular shape of the plates, the orientation of the specimens was not fixed. The tests were performed in accordance with ISO or ASTM standards. The Instron 5969 testing machine was employed to conduct the tests. During the tensile tests, the average strain was measured using an extensometer, while for the shear tests, a DIC (Digital Image Correlation) system was utilized to obtain accurate and reliable strain measurements. Table 1 shows the mechanical properties of the material, including both mean values and standard deviations. The data for the constituent materials were obtained from the manufacturers' data sheets, where only tensile properties were indicated.

Table 1 – Mechanical properties of the 1000C short fibre composite with 10 repetitions of each measurement.

Property	Composite (coef. of variation, %)	Matrix	Glass fibre	Standard
Tensile elastic modulus, GPa	6.24 ± 0.31 (5%)	1.5	70	ISO 527-4
Tensile strength, MPa	73.7 ± 4.2 (6%)	60	2500	
Poisson's ratio	0.44 ± 0.03 (7%)	0.44	0.22	
Elongation at break, %	3.6 ± 0.4 (11%)	300	-	
Shear modulus, GPa	1.62 ± 0.16 (10%)	-	-	ASTM D7078/D7078M

4.1.2   Unidirectional carbon fibre composites

Two unidirectional (UD) cross-ply carbon fibre laminates were used in this study: one for neural network training and another for validation by implementing automated fibre break identification. The UD materials were obtained during research of Breite et al. [43]. The use of cross-ply laminates allowed for the efficient loading of microscale specimens within the in-situ loading rig, and the presence of 90° plies in the layup did not affect the measured longitudinal fibre breaks.

The first UD material was produced from prepregs manufactured at KU Leuven in a hot melt drum winder. The T700SC-12K-50C carbon fibres (Toray Industries) were impregnated with Sicomin SR8500 KTA313 epoxy resin. The composite had a $[90/0]_s$ layup.

The second UD material was made from Grafil 34-700WD-24 K-1.4%A carbon fibres (Mitsubishi Chemical) and proprietary 736LT epoxy resin at North Thin Ply Technology (Switzerland). For this material a $[90_4/0_4]_s$ layup was produced. The prepreg was cured in KU Leuven's computer-controlled autoclave according to the manufacturer's recommendations [109,110].

Miniaturised double-edge-notched tensile specimens were fabricated from the cured materials using a water-jet cutter. The dimensions of the specimens were in accordance with the specifications illustrated in Figure 12. Bonding of the end tabs prior to water jet cutting ensured excellent alignment of the end tabs, which is crucial to avoid any flexure during the tensile testing.
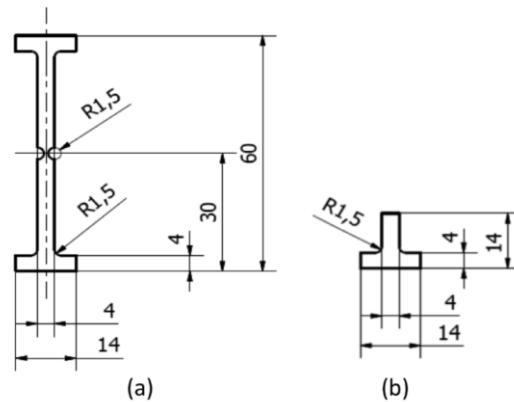
Figure 12 – Double-edge-notched tensile specimen design for SRCT measurements: (a) the specimen itself and (b) the aluminium end tab. All dimensions are in mm. (reprinted from [43] with permission from Elsevier)

4.2 Equipment

4.2.1   Lab-scaled micro-computed tomography systems

Two lab-scale X-ray computed tomography systems were used in this study: the GE Phoenix CT System v|tome|×L240 and the TeScan Unitom HR.

The GE Phoenix v|tome|×L240 CT System, located at Skoltech, features dual-tube technology, one tube with nanofocus up to 180kV and another with microfocus up to 300kV. The system is equipped with a 14-bit GE DXR-250 flat panel detector with a size of 2048×2048 pixels^2. The system is mainly designed for industrial applications, but due to the dual tube technology, it can provide high-quality images with a voxel size of up to 2 microns.

The TeScan Unitom HR, installed at KU Leuven, is a sub-micron X-ray CT system specifically designed for high-resolution and contrast imaging of small samples. It has two detectors: a 16-bit detector optimised for sharp, high-resolution images at lower kV (< 130 kV) with a size of 2916×2280 pixel^2, and the other is a 14-bit detector with 1920×1512 pixel^2 for fast scanning and high sample throughput with temporal resolutions of less than 10 seconds. The system also includes an in-situ kit for real-time experiments.

4.2.2   Synchrotron radiation computed tomography

This study uses datasets obtained by Breite et al. [111]. In-situ synchrotron radiation computed tomography (SRCT) was used with the TOMCAT beamline at the Swiss Light Source (SLS). It provides state-of-the-art technology and scientific expertise for fast, non-destructive, high-resolution, quantitative investigations on a wide variety of samples using synchrotron radiation. Absorption-based and phase contrast imaging are routinely performed on the system with isotropic voxel sizes ranging from 0.16 to 11 μm in an energy range of 8-45 keV.

4.3 Datasets

4.3.1   Short fibre composite at 2.2 µm/pixel.

To analyse the "1000P" material by X-ray technique, a cylinder of 2 mm diameter and 4 mm height was cut from the material using a computer numerical control machine from a flat compression moulded plate. The GE Phoenix CT system, equipped with a nanofocus tube, was used to acquire CT images of the SGFC at an accelerating voltage of 60 kV and a beam current of 220 µA. The scanning process involved 2400 projections with an integration time of 0.8 seconds for the detector, and a molybdenum target was used to accommodate low-absorbing samples. The optimization of CT scanning parameters was accomplished empirically based on the analysis of other composite materials on the same equipment. The sample was scanned at a resolution of 2.2 µm per pixel, resulting in a region of interest (ROI) size of $600{\times}600{\times}1800$ pixel^3 ($1320{\times}1320{\times}3960$ µm^3). However, to overcome the high graphics processing unit (GPU) memory requirements for deep learning of high-resolution scans (more details in Section 5.1.3) the CT image was downscaled to 4.4 µm per pixel (3-4 pixels per fibre diameter) using bicubic interpolation. This downscaling was employed to reduce the memory load, making it more manageable for the deep learning models, as high-resolution scans can demand substantial computational resources. The use of bicubic interpolation for this downscaling was chosen for its ability to generate more smooth, visually coherent transitions between pixels. The processed CT image was reduced to a size of $300{\times}300{\times}900$ pixel^3 and represented in Figure 13.
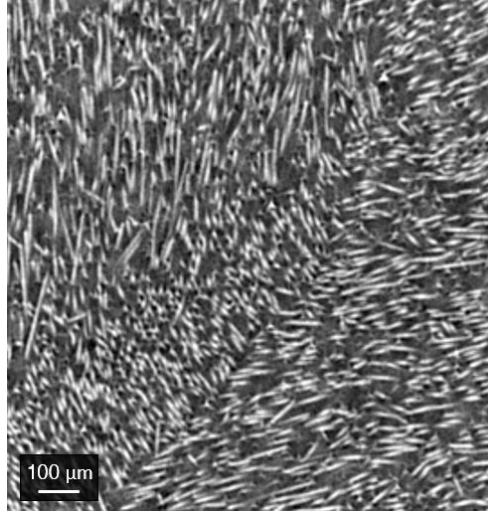
Figure 13 – CT image taken from the XY plane of "1000P" material panel manufactured by press moulding and prepared for deep learning analysis with downscaled to 4.4 μm per pixel resolution.

4.3.2 Short fibre composite at 1.0 and 4.0 μm/pixel.

To investigate the microstructure of the "1000C" material, a small $2\times2\times10$ mm^3 specimen was extracted and subjected to X-ray analysis for the purpose of deep learning processing. The TeScan Unitom HR system was utilised to acquire high and low-resolution CT images of the specimen using identical source parameters, including an acceleration voltage of 100 kV, a beam current of 50 μA, and 3000 projections with a detector exposure time of 0.65 seconds per projection. The source-to-specimen distances for the HR and LR scans were 10.1 mm and 40.4 mm, respectively. The rectangular specimen with a resolution of 1 μm per pixel resulted in an ROI size of $1984\times1848\times1972$ pixel^3 for HR images and $496\times462\times493$ pixel^3 for LR, yet both had the same physical dimensions of $1984\times1848\times1972$ μm^3. The HR and LR tomography slices are shown in Figure 14. To ensure that the same features were geometrically aligned and could be described by the same coordinate system, the images were registered in three dimensions with affine transformation using ImageJ software [112]. These CT images were used to generate periodic structures and implement the super-resolution algorithm.
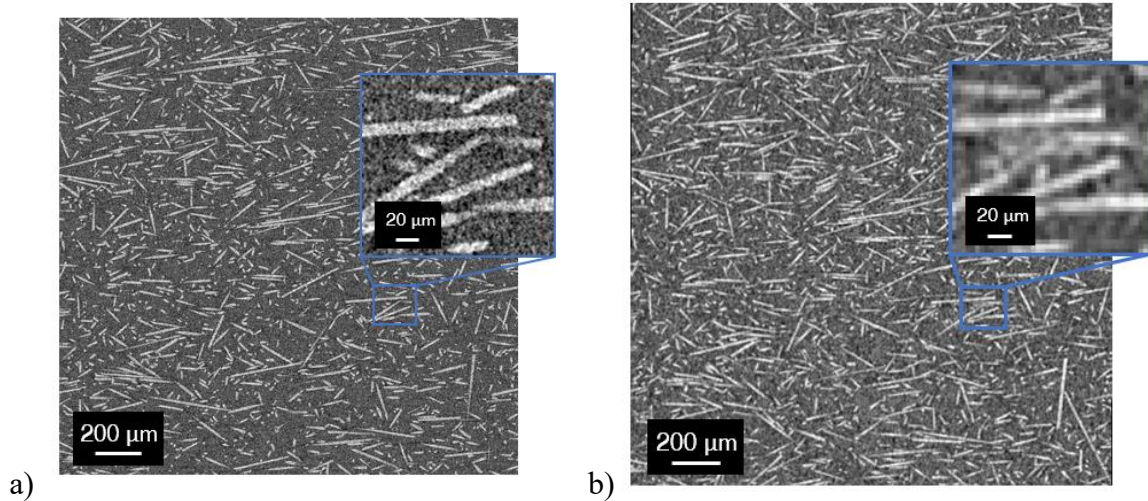
Figure 14 – CT image of "1000C" material prepared for deep learning analysis: a) HR with 1 μm/pixel resolution; b) LR with 4 μm/pixel resolution.

4.3.3 In-situ scans of unidirectional composites with fibre breaks

The dataset of in-situ scans of the UD carbon composites was obtained by Breite et al. [111]. Here, a brief description of the materials and data acquisition is given. For more detailed data specifications and access, the readers are referred to the corresponding data articles [113] and [114].

The dataset utilised in this study was obtained from two separate beamtimes performed at the TOMCAT beamline in Swiss Light Source (SLS). During the initial beamtime, the SRCT measurements were conducted collaboratively by KU Leuven, INSA Lyon, and the University of Southampton. INSA Lyon provided the tension-compression rig [115] for the in-situ experiments on the "34-700" composite, and continuous scanning was performed using the GigaFRoST camera [116]. In the second beamtime, Lund University and KU Leuven participated, and a customised Deben CT500 tension-compression rig was used. However, only static scans without loading were analysed in this study. The pco.EDGE camera was utilised to obtain high- and low-resolution images of the in-house produced material (T700SC). Although the high- and low-resolution scans

were obtained from a single specimen, minor variations in specimen position and microscope magnification occurred due to mechanical adjustments of the scanning system [117]. Table 2 describes all the essential acquisition parameters for the two SRCT datasets.

Table 2 – SRCT test and scan parameters for different purposes.

Purpose	Training set, stationary		Validation set, continuous loading
	High-resolution	Low-resolution	
Material	T700SC	T700SC	34-700
Sensor size (px^2)	2560×2160	2560×2160	2016×1716
Sensor pixel size (µm)	6.5	6.5	11.0
Energy (kV)	15	15	20
Exposure time (ms)	250	80	9
Microscope magnification	20×	4×	10×
Voxel size (µm)	0.325	1.625	1.1
Number of projections per volume	2000	2000	1000
Propagation distance (mm)	30	100	60
Displacement rate (µm/s)	-	-	1.4–1.6
Number of volumes acquired before failure	1	1	17
Testing time per scan (s)	500	160	9

The Gridrec algorithm [118] without optical distortion corrections was employed to reconstruct the absorption-based tomography. In total, one high- and one low-resolution volume of the T700SC specimen were prepared to train the super-resolution neural network as described in Section 5.2. Due to high memory consumption, the CT images were divided into small volumes to create a large training dataset (see details in Section 5.2.3). The low-resolution image was registered and interpolated to have a scale factor of 4 with the HR image, allowing the correct upscaling of 2^2. Moreover, the T700SC LR scan was adjusted to match the 34-700 LR scans in terms of average grey scale values, contrast, and sharpness. Four images were selected from 17 low-resolution scans of the 34-700 specimen with fibre break development under continuous load for fibre break analysis and verification of the super-resolution algorithm. These four images were

taken at different stages of loading: initial (0% load, where 100% load indicates failure of the specimen), intermediate load (75% load), high load (94% load) and before failure (98% load). Figure 15 illustrates the prepared images.
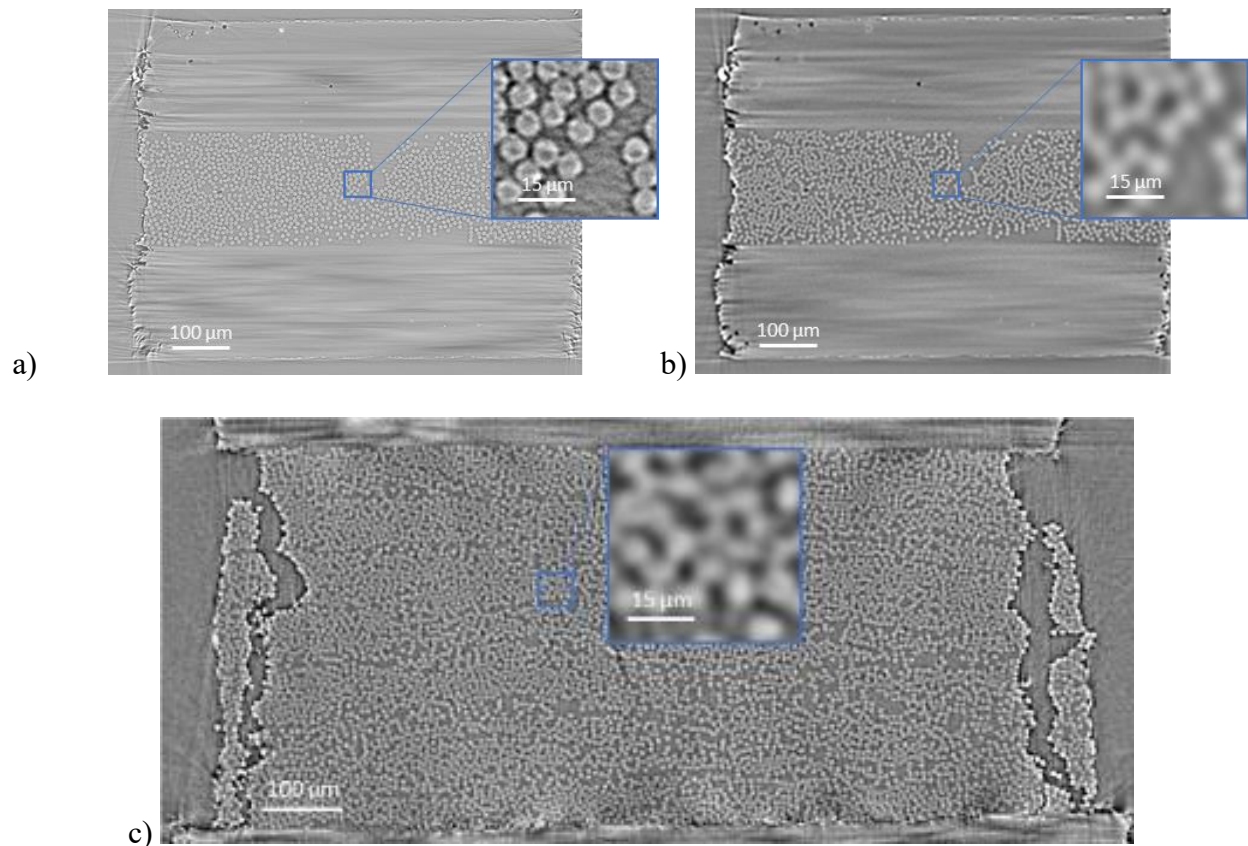
Figure 15 – Illustrations of middle slices of the CT scans of different materials in different resolutions: a) specimen of T700SC material in a high-resolution scan (0.325 µm); b) specimen of T700SC material in a LR scan (1.3 µm); c) specimen of 34-700 material in a low-resolution scan (1.1 µm).

Table 3 provides a summary of the datasets used in this PhD study: materials used, primary purpose of the dataset, X-ray equipment utilised for scanning, resolution and ROI size obtained.

Table 3 – Summary of datasets used in the research.

Name	Material	Purpose	Scanning equipment	Resolution, μm/pixel	ROI size, μm^3	Ref.
1000P	Short glass fibre composite	Inpainting	GE Phoenix v|tome|×L240	2.2	1320×1320×3960	[119]
1000C	Short glass fibre composite	SR, PBC	TeScan Unitom HR	1 and 4	1984×1848×1972	-
T700SC	UD carbon fibre composite	SR	SLS synchrotron	0.325 and 1.625	258×1040×878	[111]
34-700	UD carbon fibre composite	SR, fibre break analysis	SLS synchrotron	1.3	493×1143×1785	[111]

Chapter 5. Machine learning-based image processing of micro-CT images of composite materials.

CT imaging is a powerful and irreplaceable tool for obtaining 3D images of the internal microstructure of materials. However, the limitations of CT and 3D image processing tools have limited the full potential of CT analysis of composite materials. In recent years, machine learning techniques have emerged as a promising solution for image processing, offering advanced algorithms for image quality enhancement, including inpainting, super-resolution and segmentation. This chapter discusses the developed methods and their verifications that have the potential to greatly enhance the use of CT images for composite material analysis.

5.1 Inpainting: image restoration and generation

The description of the inpainting methods and their results are based on the published work of Karamov et al. [119].

5.1.1   Introduction

The first objective of this thesis is to develop an inpainting algorithm for CT images of composite materials. Inpainting is an image processing technique that allows the generation of missing or damaged areas in an image while preserving its overall integrity and accuracy. The algorithm can also be used to remove unwanted objects from an image. The term "inpainting" originated in the field of art restoration, where it is used to describe the process of restoring damaged paintings [120]. Bertalmio et al. pioneered the concept of inpainting in digital images [121], and now these methods are widely used in computer vision and have undergone significant development in recent years [122]. The inpainting tool can enhance the CT analysis of any material. Section 2.1 of the literature review described how CT analysis of composite materials has progressed and how new methods have been developed to transform CT images into finite

element models. A generative inpainting tool for CT data can have numerous possible applications such as artificially increasing the size of CT images to achieve an appropriate RVE size for future finite element modelling, generating the microstructure in macro-meso coupled models, and manipulating the material microstructure in various ways, e.g., removing the X-ray ring of beam hardening artefacts [123–127].

Inpainting techniques can be classified into two categories: sequential and machine learning-based methods. One of the earliest approaches to inpainting involved diffusion algorithms, which generated smooth image parts based on the data near the missing area, similar to liquid diffusion [121,128]. A further breakthrough came with patch-based sequential methods, also known as exemplar-based methods, which find the most appropriate example from the same image to fill the missing part [129,130]. However, these methods were primarily developed for 2D inpainting and are not easily applicable to 3D data such as CT images. When applied to 2D slices of CT images, they introduce slice-to-slice inconsistencies in the microstructure, and the randomness of the sequential algorithm may generate similar images differently [3,20], resulting in incomplete structure generation that is only suitable for capturing patterns and textures, but may struggle with complex images, such as images of random composite materials.

Table 4 summarises the advantages and limitations of each family of methods.

In the field of image synthesis and processing, deep learning has recently made significant progress. Compared to traditional techniques, deep neural networks demonstrate superior performance in terms of understanding the conceptual content of images [131]. Convolutional neural networks (CNNs) and generative adversarial networks (GANs), first introduced by Goodfellow et al. in 2014, are currently considered state-of-the-art methods for various image-related tasks [132–134].

Table 4 – Inpainting methods.

Method		Benefits	Limitations	Application to 3D	Ref.
Conventional approach	Diffusion	1) Easy to implement (only one equation). 2) Fast	1) Limited to elongated areas (lines). 2) Not suitable for complex images.	No implementations for 3D cases.	[121,128]
	Patch	1) Robust for simple and textured images.	1) Only for 2D case. 2) Not suitable for complex images.	No implementations for 3D cases.	[130,135]
Deep learning approach	CNN	1) Identifies data features. 2) Suitable for complex images.	1) Requires labelled image dataset for training. 2) Limitations in image generation.	Scalable to 3D case by applying 3D filters to the initial image.	[133,136]
	GAN	1) Designed for image generation. 2) No need for labelled data examples. 3) Works well with a lack of data.	1) High-resolution image training requires large GPU memory.	Straightforward extension to 3D CNN.	[134,137, 138]

Deep learning-based inpainting techniques have demonstrated remarkable achievements, particularly in the 2D domain [139–144]. However, the emerging field of 3D image generation and inpainting poses new challenges, such as the added dimensionality and the high demands on GPU memory, which make it difficult to handle higher-resolution data. Recent studies indicate the potential for the development of methods for 3D cases, including point cloud inpainting [145,146], shape inpainting of scanned real objects using a full convolutional volumetric autoencoder network

[147], and 3D encoder-decoder generative adversarial network [148]. These approaches are not suitable for images and are currently limited to 3D shapes and point clouds but are already being used for various applications [39,40]. Their effectiveness in the context of CT images of composite materials remains to be investigated.

The research community currently faces a challenge in the lack of established practices for 3D image inpainting, particularly in the CT field. This section describes a novel inpainting methodology that has been developed for CT images of fibrous materials, and its effectiveness has been demonstrated on random fibre composites. The proposed approach employs 3D encoder-decoder generative adversarial networks and incorporates the use of image-related and physics-related metrics that are relevant to the specified materials to assess the quality of inpainting. Three different neural network architectures were designed and evaluated, taking into account the level of generation detail, algorithm performance, and GPU memory usage. Notably, the proposed models are not intended to generate singularities which are not present in the used dataset (however, the models can be adapted to generate such singularities using a different dataset).

5.1.2   Deep learning for image processing

This subsection provides a brief explanation of how deep learning is implemented for image processing, to facilitate a better understanding of the following explanations.

Imaging system problems can be solved using machine learning and deep learning techniques. These problems consist of an operator R that uses images X to calculate outputs Y, which can be vectors of feature measurements or new images. In the learning approach, a set of initial images X and their corresponding results Y are known, and mathematically, any learning approach can be represented as a parametric reconstruction algorithm R_{learn} [133]:

$$R_{learn} = \arg\min_{R_\theta, \theta \in \Theta} \sum_{n=1}^{N} f(x_n, R_\theta(y_n)) + g(\theta) \qquad (3)$$

where $\{(x_n, R_\theta(y_n))\}_{n=1}^{N}$ is a training set of images and corresponding outputs respectively; Θ is the set of all trainable parameters θ; f – the cost function to measure the error between the input and desired output; and $g(\theta)$ – the regularisation function to prevent overfitting of trainable parameters. The purpose of the optimisation function $argmin$ is to minimise the sum of cost and regularisation measures across training sets by optimising the parameters θ of the algorithm R_θ.

Deep learning algorithms primarily utilize artificial neural networks with two and more hidden layers with the ability to learn features of the raw data Figure 16. For readers seeking a fundamental understanding of neural networks and hidden layers, it is recommended to consult [149] for further information.
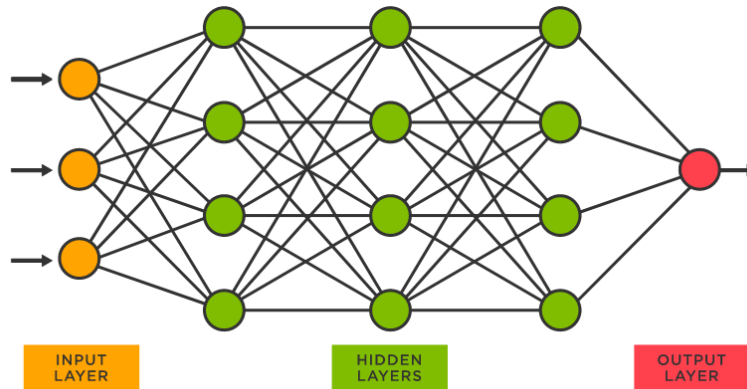
Figure 16 – An example of an artificial neural network with 3 nodes as input, 3 hidden layers with 4 neurons each and one output node, overall, it already has 60 trainable parameters.

The number of parameters of deep learning algorithms often exceeds millions, and the optimisation of these parameters is usually performed by the gradient descent process and its

modifications such as backpropagation. During backpropagation, the network's output error is propagated backwards through its layers, and the weights of the connections between neurons are updated proportionally to their contribution to the error, ultimately optimizing the model's performance. While further elaboration on these optimization algorithms is not within the scope of this work, readers are encouraged to refer to [150,151] for more comprehensive information.

5.1.2.1 Convolutional neural networks

One of the most robust examples of deep learning algorithms is the convolutional neural network (CNN) which was developed for image processing [133,152]. The convolutional layer is the core component of the CNN and serves as an extractor of image features. Unlike traditional fully connected feedforward neural network layers, in convolutional layers, the neurons are organised into groups of a certain size (receptive fields) that can overlap, and only one group is connected to the neuron of the next layer (Figure 17a). The groups are connected using the "parameter sharing" technique [153], where the corresponding neuron parameters (usually called weights) are constrained to be equal to each other in different groups ($w_1 = w_4, w_2 = w_5, w_3 = w_6$). Matrices of these weights are referred to as filters; each specific filter is intended to determine a specific feature of the image (straight lines, curves, etc.). To introduce nonlinearity to the system and increase its performance, resultant neurons are subjected to nonlinear function [154] (tanh, sigmoid, ReLU). In practice, to reduce the dimensionality of the network and thus the size of the input data, after a convolutional layer comes a pooling (subsampling) layer that outputs the maximum or average value from the set of neurons.

The feature maps [153] decoded by the convolutional layers can serve as input to the next convolutional or dense layer, or they can serve as the final layer, representing the feature vector or latent space. This feature vector is a compressed representation of the extracted features of the

image for the specific CNN architecture used (Figure 17b). There can be several CNN families in a network architecture. In the notation of equation (3), R_θ represents a network architecture (of one or many CNNs), while θ represents the weights to be learned during training. Methods based on CNN are remarkably diverse with respect to their architectures, which can vary widely in terms of the number of convolutional layers, filter sizes, nonlinearities, and other characteristics. CNNs can also be extended to 3D applications by constructing 3D receptive fields from the image [155].

a)

b)
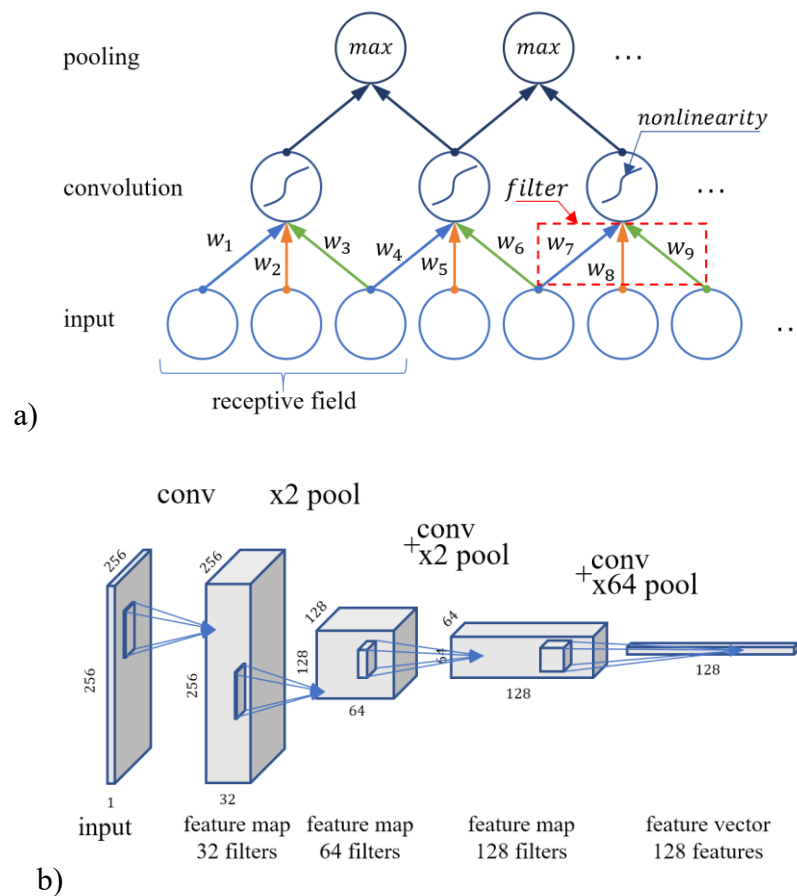
Figure 17 – Graphical representation of convolutional neural network:
a) basic elements of neural networks in layers; b) example of CNN architecture for 256x256 image.

5.1.2.2 Generative adversarial networks

The use of feature vectors, which contain the compressed image information, allows the regeneration of images as close as possible to the original ones, using reverse operations called

deconvolution [156]. Deep convolutional models with a neural network struggle to regenerate images correctly due to difficulties in selecting the loss function for estimating the validity of the obtained results (function $f()$ from (3) is non-trivial). To circumvent these difficulties Goodfellow et al. [157] proposed a generative adversarial nets framework that operates via an adversarial process and consists of two separate models: the generator (G) and the discriminator (D), typically implemented by deep neural networks. The generator reconstructs an image from the feature vector as close to the original as possible, while the discriminator determines whether the image is from an actual ground truth dataset or generated (Figure 18), and their purpose is to compete with each other. During this adversarial process, the neural networks learn and continuously enhance their abilities to generate and discriminate.

The optimisation of GAN trainable parameters corresponds to a two-player minimax game theory: the optimisation process stops when the minimum of the generator and the maximum of the discriminator are reached [158]. Various GAN models have been developed, demonstrating exceptional performance in diverse application areas such as image generation, object detection, facial attribute manipulation, and inpainting challenges [134]. GANs have proven to be versatile and powerful tools in many different fields due to their ability to produce high-quality results in a variety of tasks.
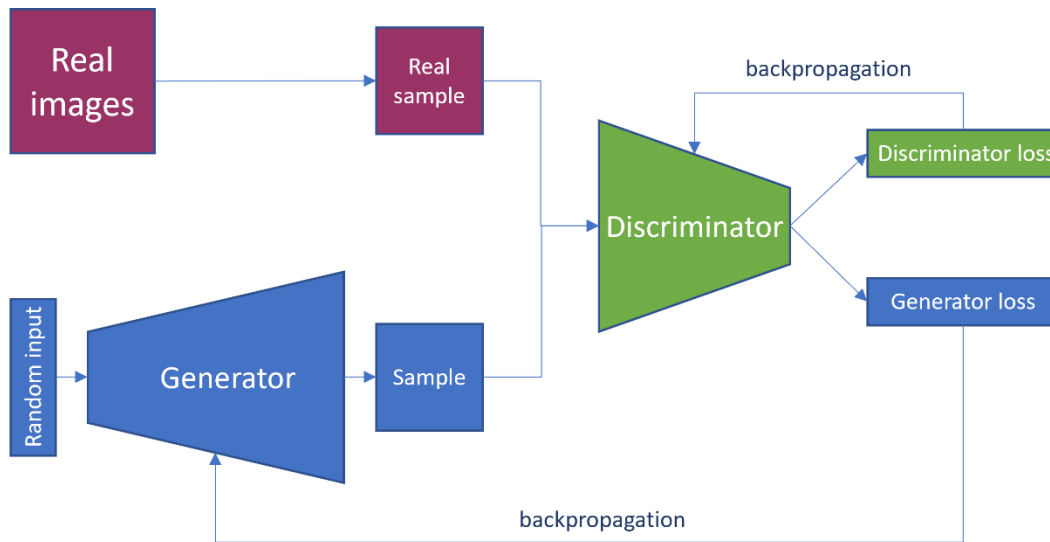
Figure 18 – Example of generative adversarial network architecture with random input

Inpainting GAN models were initially developed for 2D applications using conventional methods. One of the pioneering works in this field employed a combination of CNN and GAN to predict pixels based on contextual information, using an encoder-decoder pipeline [136]. Subsequent research built upon this approach, introducing innovations such as the use of arbitrary masks [139], global and local discriminators [138], and integration with the patch-match algorithm [142].

Although originally developed for 2D images, the principles of operation and deep learning architecture of inpainting GAN models make them potentially applicable to three-dimensional cases. Recently, there has been growing interest among researchers in exploring the possibilities of GANs for generating 3D shapes and images. For instance, some studies have described 3D deep learning models for the inpainting of point clouds [145,146], while others have transferred the methodology to the task of inpainting 3D shapes captured by 3D sensors [148]. In the latter work, a 3D encoder-decoder GAN was implemented to generate 3D shapes, given that the challenges of working with 3D data require a larger number of trainable neural network parameters and GPU

memory. The reconstructed shapes were further improved using long-term recurrent convolutional networks. Subsequent research proposed a 3D GAN with both local and global discriminators to address the issue of high GPU requirements [159].

5.1.3   Developed algorithms

In this study, deep learning techniques were utilized to generate new images based on initial images. Specifically, a GAN model was employed, which consisted of two separate models - a generator and a discriminator. The architecture of the developed GAN is depicted in Figure 19.
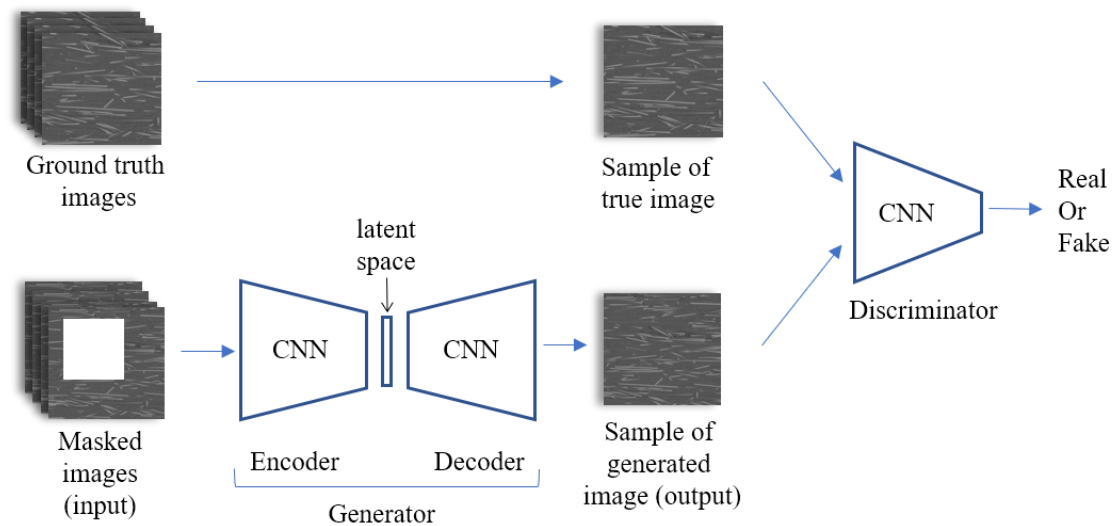
Figure 19 – Encoder-decoder generative adversarial network architecture for inpainting of 3D micro-CT slices of short fibre composites

The generator of the GAN model employed in this study consisted of two distinct parts, namely an encoder and a decoder, as illustrated in Figure 19. Following an empirical analysis of neural network architecture and its hyperparameters, the encoder was designed using 3D convolutional layers, in which neurons were locally connected and trained to identify image features and output them in a feature map. The weights of these neurons formed 3D filters, which were optimised during training to improve the performance of the model. To introduce non-linearity into the system and facilitate learning of complicated microstructure, the LeakyReLU

nonlinear activation function was employed for each layer [160]. LeakyReLU is chosen as the activation function for its ability to prevent the vanishing gradient problem, promoting more stable and efficient training. In addition, batch normalisation was applied to standardise the layer inputs for each batch, thereby increasing the stability and speeding up the learning process of the neural network [161]. Furthermore, the architecture was augmented with dilated convolutional layers [162], which utilize sparse filters to enable the analysis of larger volumes with the same number of parameters. Finally, the 3D image features were consolidated into a latent space using a final convolutional layer, which served as input to the decoder.

The decoder component of the GAN model was designed to generate a reconstructed image from the features stored in the latent space, without any missing regions or defects. It was constructed symmetrically to the encoder, containing transposed 3D convolution (deconvolution) layers, ReLU nonlinear activations, and batch normalizations. The final layer of the decoder component activated the output by utilizing the hyperbolic tangent function, which ensured that the final values were within the range of -1 to 1. This was done to maintain consistency with the data range of the original images and to facilitate easier interpretation and analysis of the generated images.

For investigation purposes, three generator models were developed, each with a similar structure but differing in depth and the number of trainable parameters. These models were denoted as CNN3, CNN5, and CNN7, indicating the number of convolutional layers before the latent space. Deeper neural networks, such as CNN9, were also under consideration; however, their substantial GPU memory requirements, coupled with hardware limitations, precluded their training during this research. The architecture with the highest complexity that could be accommodated within the GPU memory, namely CNN7, had seven convolutional layers before the latent space, and the

detailed parameters of this architecture are presented in Table 5. To obtain the CNN5 model, from 7 to 10 layers were removed from CNN7, resulting in a smaller latent space of size 8×8×8×256 (with a convolutional layer stride equal to one and an input size of 8×8×8×256), as shown in Figure 20. A similar approach was taken to derive the architecture with 3 convolution layers.
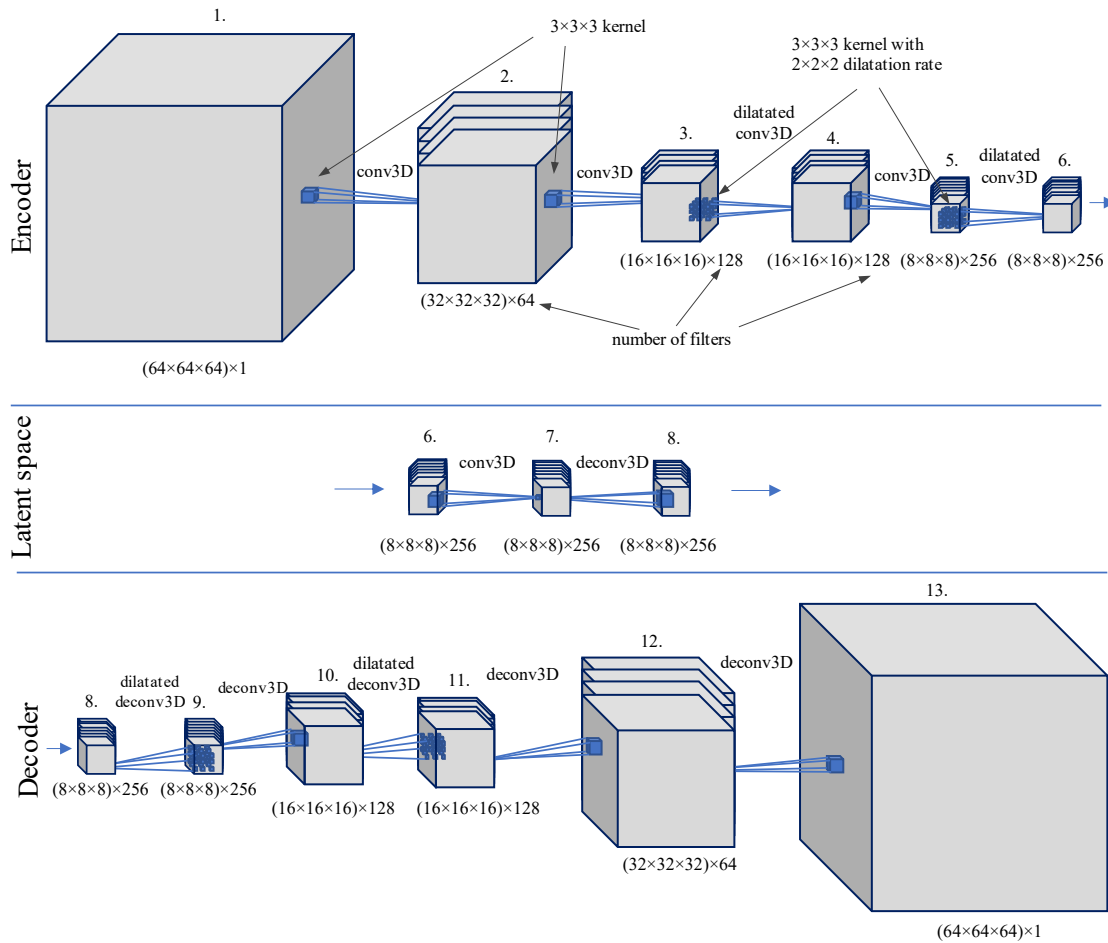
Figure 20 – Visual representation of the architecture of the CNN5 generator model designed to process 64×64×64 input images.

The discriminator in the GAN model was designed as a convolutional neural network classifier with a different number of convolutional layers for each generator type. While the discriminator structures were identical for all generator types, CNN7 had 4 convolutional layers,

CNN5 had 3, and CNN3 had 2. Each layer used LeakyReLU nonlinear activation and batch normalisation. The final feature map was flattened and fully connected to a single neuron that predicted whether the input was an original image or one generated by the generator.

All convolutional and deconvolutional layers in the network had a kernel size of 3, and the "same" padding was employed. The number of filters in convolutional and deconvolutional layers, that did not use a single stride, was doubled from layer to layer, starting with 64 filters. The strides of the layers are listed in Table 5.

Table 5 – Detailed parameters of the CNN7 generator and discriminator architectures.

№	Layer	Input	Stride	Activation	Output
The generator					
1.	Conv3D	64×64×64×1	2×2×2	LeakyReLU+BN	32×32×32×64
2.	Conv3D	32×32×32×64	2×2×2	LeakyReLU+BN	16×16×16×128
3.	Dil.conv3D	16×16×16×128	1×1×1	LeakyReLU+BN	16×16×16×128
4.	Conv3D	16×16×16×128	2×2×2	LeakyReLU+BN	8×8×8×256
5.	Dil.conv3D	8×8×8×256	1×1×1	LeakyReLU+BN	8×8×8×256
6.	Conv3D	8×8×8×256	2×2×2	LeakyReLU+BN	4×4×4×512
7.	Conv3D	4×4×4×512	1×1×1	LeakyReLU+BN	4×4×4×512
8.	Conv3D	4×4×4×512	1×1×1	LeakyReLU+BN	4×4×4×512
9.	Deconv3D	4×4×4×512	1×1×1	ReLU+BN	4×4×4×512
10.	Deconv3D	4×4×4×512	1×1×1	ReLU+BN	4×4×4×512
11.	Deconv3D	4×4×4×512	2×2×2	ReLU+BN	8×8×8×256
12.	Dil.deconv3D	8×8×8×256	1×1×1	ReLU+BN	8×8×8×256
13.	Deconv3D	8×8×8×256	2×2×2	ReLU+BN	16×16×16×128
14.	Dil.deconv3D	16×16×16×128	1×1×1	ReLU+BN	16×16×16×128
15.	Deconv3D	16×16×16×128	2×2×2	ReLU+BN	32×32×32×64
16.	Deconv3D	32×32×32×64	2×2×2	tanh	64×64×64×1

The discriminator					
1.	Conv3D	64×64×64×1	3×3×3	LeakyReLU+BN	32×32×32×32
2.	Conv3D	32×32×32×64	3×3×3	LeakyReLU+BN	16×16×16×64
3.	Conv3D	16×16×16×128	3×3×3	LeakyReLU+BN	8×8×8×128
4.	Conv3D	8×8×8×256	3×3×3	LeakyReLU+BN	4×4×4×256
5.	Flatten	4×4×4×512	–	LeakyReLU+BN	32768
6.	Dense	32768	–	Sigmoid	1

During the training process, the generator was optimized using reconstruction and adversarial loss functions, the discriminator relies only on adversarial loss. The reconstruction loss function aimed to ensure that the generator correctly captured the features of the ground truth images, but it also has the drawback of merging and averaging different microstructure features in the output. On the other hand, the adversarial loss function is used to focus the reconstruction on one specific microstructure type with pixel precision, thereby making the prediction look more realistic [136].

The mean squared error (MSE) was used for the reconstruction loss, which aimed to minimize the average pixel-wise error:

$$L_{rec} = \frac{1}{N}\sum_{n=1}^{N}(G(\mathbf{x})_i - x_i)^2 \,, \tag{4}$$

MSE is often preferred in GANs for its simplicity and sensitivity to small errors, making it suitable for fine-tuning the generator's output. It aligns well with the GAN objective of minimizing the discrepancy between real and generated data.

The adversarial loss was implemented using binary cross-entropy by adapting the GAN min-max optimisation method. For binary cross-entropy, each predicted probability of the discriminator

output was compared to the actual class output, which can be either 0 or 1 and can be expressed as:

$$L_{adv} = \mathbb{E}_{\mathbf{x} \sim \mathbf{X}}[\log(D(\mathbf{x})) + \log(1 - D(G(\mathbf{x}')))], \qquad (5)$$

where $\mathbf{x}'$ is a corrupted image of ground truth image $\mathbf{x}$ of dataset $\mathbf{X}$, and $\mathbb{E}_{\mathbf{x} \sim \mathbf{X}}$ denotes expectation over all the population images $\mathbf{x}$ in $\mathbf{X}$ dataset. N is the number of pixels in one 3D image, and x_i and $G(\mathbf{x})_i$ are representations of the i-th pixel of ground truth and reconstructed images, respectively. $D(\cdot)$ is the output of the discriminator network, $G(\cdot)$ – the generator network output. In the GAN training, where the generator and discriminator were trained jointly, the total loss function was a combination of the reconstruction and adversarial losses, weighted λ_{rec} and λ_{adv}, respectively:

$$L_{GAN} = \lambda_{rec} L_{rec} + \lambda_{adv} L_{adv}. \qquad (6)$$

5.1.4   Data processing and implementation

As described in Section 4.3.1, the GE Phoenix CT System was used to scan a cylindrical specimen made from the first random glass fibre composite. The micro-CT image obtained had a resolution of 2.2 μm per pixel and a pixel size of $600 \times 600 \times 1800$ pixel^3, corresponding to an actual scanned volume of $1320 \times 1320 \times 3960$ μm^3. However, deep learning of high-resolution scans required a large amount of GPU memory. Therefore, the micro-CT image was downscaled to 4.4 μm per pixel (3 pixels per fibre diameter) using bicubic interpolation. The processed micro-CT image was reduced to a size of $300 \times 300 \times 900$ pixel^3 for more efficient processing.

To prepare a training dataset for the neural network, the processed CT image of size $300 \times 300 \times 900$ was utilized. The image was represented as a 3D array of grey scale values that were normalised to a range of 0 to 1. The training dataset was composed of two types of volumes: ground truth (true) and masked (input) volumes, each containing N = $64 \times 64 \times 64$ pixels. Ground

truth volumes were randomly selected from the full image volume, while masked volumes were generated by applying a mask with a size of 32×32×32 pixel^3 to the ground truth volumes. Specifically, a random mask region covering one-quarter of the true volume was removed and replaced with a value of -1. This procedure enables a continuous and unique pairing of true and input images, resulting in a robust algorithm for generating training pairs for the neural network.

Python 3.8 and the TensorFlow 2.5 framework [92] were utilized to implement the deep learning architectures. The models were trained on GPU Nvidia RTX 3070 using the ADAM stochastic gradient descent solver [151] for trainable parameter optimisation with $\beta = 0.5$. To facilitate the training process, a batch size of 8 training examples was used for each training step. Following [148], the loss weights λ_{rec} and λ_{adv} were set to 0.999 and 0.001, respectively. Typically, the discriminator requires less training time than the generator because generating new data is a more complex task than distinguishing between real and reconstructed data [157,163]. To ensure that the training pace of both networks was comparable, the learning rates for the generator and discriminator were set to 10^{-4} and 10^{-6}, respectively, which determines the amount by which the weights of the neural networks are updated at each step.

We also performed a pre-training procedure on the generator, which consisted of 20000 training steps. In each step, we used the algorithm outlined in section 5.1.3 to obtain a true and fake image pair. The weights of the discriminator were updated separately for the true and fake portions of the batch in each iteration. In accordance with the methodology presented in [163], we restrained the training of the discriminator once it was able to accurately differentiate between real and fake pairs. Specifically, we only trained the discriminator if its prediction accuracy was below 90%. The generator was trained to regenerate masked regions in such a way that the discriminator would classify the generated images as true. In other words, the adversarial loss was minimised

without training the discriminator. We trained the GAN models until their respective losses reached a plateau, with a duration of about 24 hours for each model.

5.1.5 Validation and material-related criteria

From the processed CT image, five validation images were excluded and prepared for the validation procedure. As these volumes were not included in the generation of the training dataset, their features were not considered in the training process.

To assess the quality of generated volumes according to real-world scenario criteria, we employed peak signal-to-noise ratio (PSNR) and physical metrics such as materials anisotropy (difference of mean degree of anisotropy) and fibre orientation distribution (orientation tensor difference, degree of orientation and cosine similarity).

While MSE evaluates the level of distortion in the generated image compared to the true image during the training process, PSNR is a common metric that approximates human perception of image quality. The formula for PSNR is:

$$PSNR = 10 \cdot \log_{10}\left(\frac{max_I^2}{MSE}\right) = 20 \cdot \log_{10}\left(\frac{max_I}{\sqrt{MSE}}\right) \tag{7}$$

The value max_I represents the maximum value in the image, which is equal to 1 in the normalized images used in this paper. A higher PSNR value indicates a better image generation quality.

To calculate the physical metrics of composite materials, specifically the fibre orientation distribution (FOD) and the degree of anisotropy, we utilized the structure tensor analysis method [39] within the VoxTex software developed by KU Leuven, Belgium. This method allowed us to extract physical metrics even from low-resolution micro-CT images [3,60,164–168].

Fibre orientations are described using a spherical coordinate system as in Figure 21 (polar φ and azimuthal θ angles) as well as orientation tensors, an efficient and concise description of

FOD [169]. Second-order orientation tensors for an assembly of individual fibres $\{\boldsymbol{p}^k\}_{k=1}^n$ can be represented in the discretized form:

$$a_{ij} = \frac{1}{n}\sum_{k=1}^{n} a_{ij}^k = \frac{1}{n}\left(\sum_{k=1}^{n} p_i^k p_j^k\right), \tag{8}$$

where $\boldsymbol{p}$ is a unit orientation vector $\boldsymbol{p} = (p_1, p_2, p_3) = (\sin\theta\cos\varphi, \sin\theta\sin\varphi, \cos\theta)$ [169].
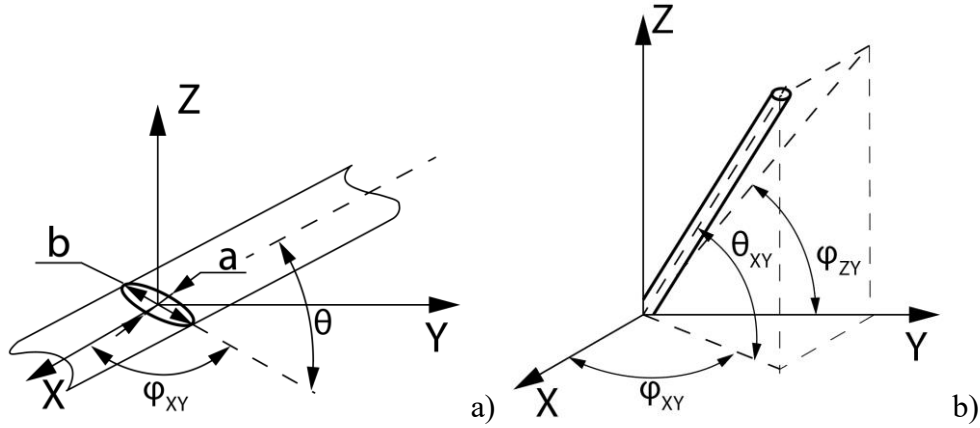
Figure 21 – Spherical coordinate system: (a) orientation angles of a single fibre and elliptical section of the fibre; (b) cross sections of micro-CT scans used for ellipsometry: main slices orthogonal to X axis are shown; (c) θ_{XY} angle can be reconstructed from φ_{XY} and φ_{ZY}.

Three measures were used to compare the orientation tensors: tensor difference, orientation degree and cosine similarity. The orientation tensor information can be compared as a whole using the tensor difference measure:

$$D_T = \sqrt{\sum_{i=1}^{3}\sum_{j=1}^{3}(a_{ij} - b_{ij})^2} \tag{9}$$

To compare how different the generated isotropic orientation distribution is from the original distribution, we use a measure of orientation degree. This measure calculates a value by normalising the largest eigenvalue λ_1^{OT} of the orientation tensor:

$$O_D = \frac{3}{2}\left(\lambda_1^{OT} - \frac{1}{3}\right) \tag{10}$$

Finally, the cosine similarity can be calculated using a dot product of the main direction vectors (V_1 and V_2) for the investigated orientation distributions or using the angle α between these main directions:

$$S_c = |V_1 \cdot V_2| = |\cos\alpha| \tag{11}$$

5.1.6   Results and discussion

Neural networks with three, five, and seven convolutional layers, referred to as CNN3, CNN5, and CNN7, respectively, were trained for 24 hours with a specific number of iterations. The decision to train for 24 hours was driven by the challenges in GAN training, as both analytical and adversarial metrics can plateau while image quality continues to improve. Additionally, to ensure an equitable comparison, an equivalent training duration was adopted for CNN3, CNN5, and CNN7, despite their distinct convergence times. The mean squared error (MSE) of the models decreased continuously during training until it reached a plateau, after which training was stopped. CNN7 was stopped immediately after reaching the plateau, while CNN5 and CNN3 were trained for some additional time on the plateau.

In Figure 22, the validation images with masked regions in the centre are shown, and the resulting inpainted images generated by the trained models are also displayed.
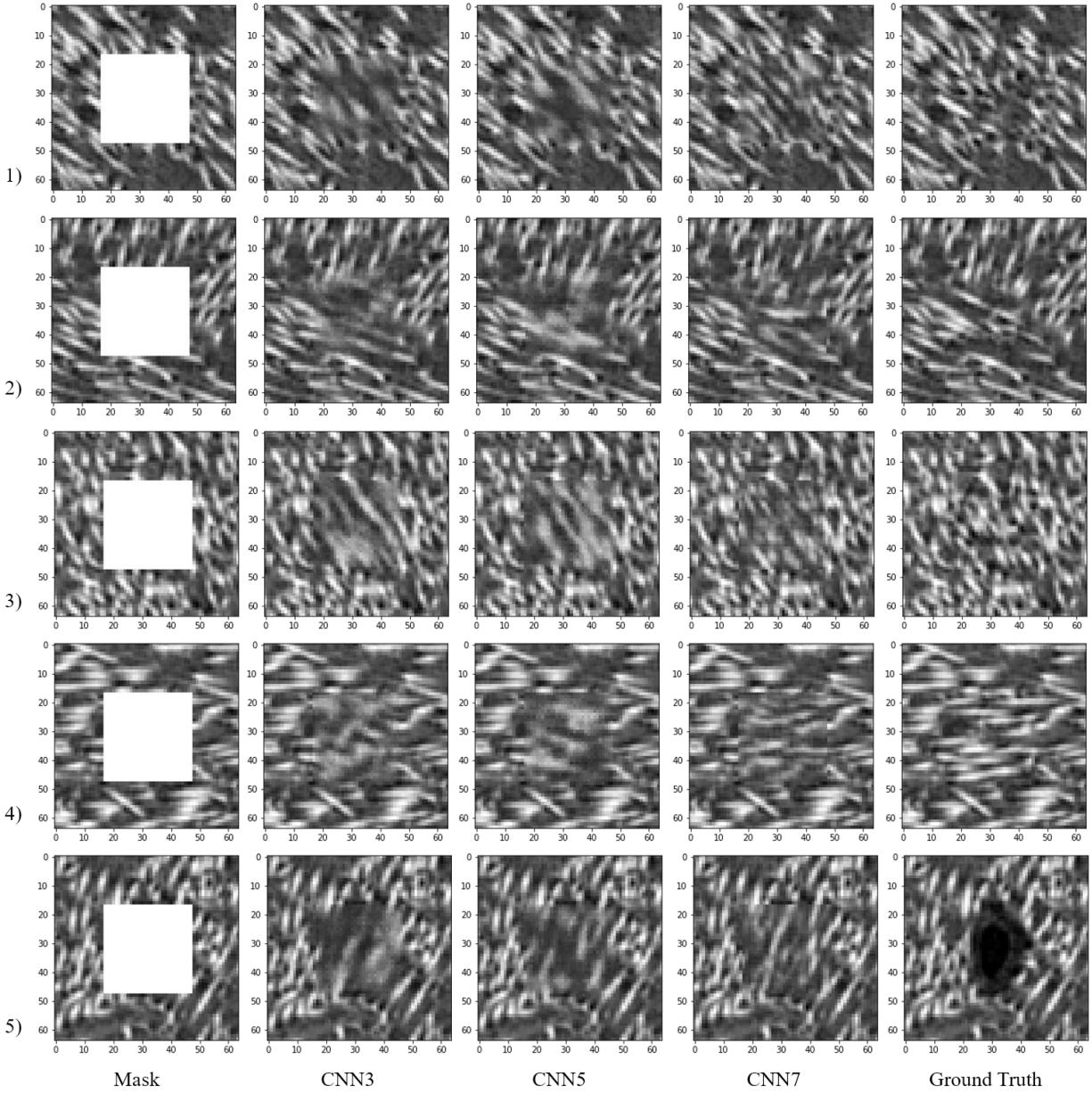
Figure 22 – Central slices of the regenerated validation images using three GAN models in five different locations: 1) predominant fibre direction; 2) two different fibre orientations; 3) vertical fibre orientation; 4) horizontal fibre orientation; 5) cavity. The validation images were not used in the training process. The pixel size was 4.4 μm.

Each row in the figure presents five examples of image generation, including 1) dominant in the material fibre direction; 2) fibre orientation transition; 3) prevalently vertical fibre

orientation; 4) prevalently horizontal fibre orientation; 5) cavity with the size of the mask. The models take less than one second to generate inpainted images once they are trained.

A visual comparison of the inpainted images produced by the neural networks shows that the CNN7 with the deepest architecture produced the most accurate reconstructions of the original images. The inpainted regions of the corrupted CT images were seamlessly integrated into the surrounding context. In the first example, the fibre sizes and orientations were accurately restored to match those of the original image. In the second example, the CNN7 model correctly recognised the location of the fibre orientation change. Similarly, in the other examples where no singularities were present, the CNN7 architecture successfully generated fibre diameters and orientations that closely resembled the original image, with no noticeable unnatural fibre curves or defects. Minor artifacts are present at the periphery of the generated area, resulting in a less-than-optimal smoothness in the border transition. However, in the last example, where the training dataset did not contain any images with a void of the same size as the masked region, the CNN7 model filled the void with fibres, resulting in an image that differed significantly from the ground truth.

Although the neural networks with fewer trainable parameters were able to generate the missing regions of the masked volumes, their performance was somewhat limited. The CNN5 architecture lacked precision in fibre shape generation and introduced some noise, particularly in situations that were under-represented in the dataset. For example, in the fourth example, this model produced fibres with incorrect diameters and orientations. However, in the second example, CNN5 was able to accurately identify two fibre directions. Similarly, the CNN3 model showed similar visual limitations to CNN5, but to a greater extent. In the second and fourth examples, this model was unable to identify orientation patterns, resulting in unnaturally twisted fibres. In addition, CNN3 was found to generate significantly fewer fibres in the region of interest than the

other models and also the image quality of the generated fibres is much lower comparing with CNN5 and CNN7. However, it is worth noting that all NN architectures were able to effectively inpaint the cavity with fibres in the fifth example, albeit without complete accuracy. While specific evaluations of GAN performance on RVEs of varying sizes were not conducted, it is anticipated that generating larger RVEs may lead to a heightened presence of artifacts. This effect is expected to be more pronounced when using smaller neural networks compared to larger ones.

When considering image-related metrics such as MSE and PSNR, it is worth noting that the simplest neural network architecture demonstrated the lowest error values (as shown in Table 3). This can be attributed to the fact that in a simple neural network, the discriminator is unable to provide meaningful feedback during the training process. As a result, the generator tends to focus on reducing the overall error, which may lead to merging and averaging different generation modes, while ignoring the feedback from the discriminator [170,171].

When comparing physical metrics such as anisotropy and orientation, it becomes evident that CNN7 outperforms the CNN3 and CNN5 models. Comparing the whole volume and masked volume as our region of interest (ROI), as indicated in Table 6, CNN7 exhibits an average error relative to the ground truth of 0.4% and 2% for the degree of anisotropy, and 2% and 14% for the orientation tensor. In contrast, for CNN3, the corresponding errors are 1% and 4.15% for the degree of anisotropy and 3% and 20% for the orientation tensor (Table 6). When considering rare generation scenarios such as the fourth and fifth examples, significant differences can be observed in all physical metrics for CNN3, particularly for the fourth example where the degree of anisotropy error is five times higher than that of CNN7, and the orientation tensor difference is 43.8%.

Table 6 – Validation and material-related criteria of full images and only generated region of interest (ROI).

Criteria	Example	CNN3	CNN5	CNN7	CNN3 ROI	CNN5 ROI	CNN7 ROI
MSE	1	0.0163	0.0201	0.0210	0.128	0.157	0.160
	2	0.0144	0.0192	0.0200	0.113	0.151	0.154
	3	0.0195	0.0233	0.0233	0.153	0.181	0.178
	4	0.0190	0.0233	0.0242	0.148	0.181	0.184
	5	0.0208	0.0215	0.0269	0.163	0.168	0.208
	avg	**0.0180**	**0.0215**	**0.0231**	**0.141**	**0.168**	**0.177**
PSNR (higher is better)	1	35.74	33.94	33.56	16.85	15.06	14.67
	2	36.80	34.32	33.98	17.91	15.43	15.09
	3	34.18	32.65	32.64	15.29	13.76	13.75
	4	34.40	32.67	32.34	15.52	13.78	13.45
	5	33.65	33.36	31.39	14.76	14.47	12.50
	avg	**34.95**	**33.39**	**32.78**	**16.07**	**14.50**	**13.90**
Difference of mean degree of anisotropy, %	1	0.53	0.47	0.10	0.92	4.83	1.67
	2	0.53	0.97	0.49	0.63	4.92	2.45
	3	0.11	0.60	0.40	1.48	7.20	1.35
	4	2.85	1.15	0.79	13.57	2.72	2.46
	5	0.19	1.31	0.08	4.74	8.47	7.62
	avg	**1.00**	**0.80**	**0.45**	**4.15**	**4.92**	**1.98**
Orientation tensor difference, %	1	2.01	2.35	1.54	13.5	17.5	9.4
	2	0.41	1.67	0.91	2.8	14.2	10.5
	3	1.81	2.34	2.31	14.8	21.1	16.7
	4	5.80	3.84	2.97	43.8	27.8	16.5
	5	3.82	4.65	2.71	25.9	22.8	15.2
	avg	**2.77**	**2.97**	**2.09**	**20.2**	**20.7**	**13.7**
Degree of orientation, %	1	0.013	0.001	0.001	0.046	0.007	0.003
	2	0.005	0.025	0.015	0.046	0.148	0.206
	3	0.030	0.034	0.011	0.227	0.322	0.210
	4	0.089	0.050	0.022	0.563	0.292	0.161
	5	0.013	0.034	0.002	0.085	0.027	0.071
	avg	**0.034**	**0.027**	**0.012**	**0.221**	**0.192**	**0.145**
Cosine similarity, %	1	0.103	0.086	0.042	3.89	5.27	1.24
	2	0.003	0.011	0.001	0.07	0.19	1.04
	3	0.025	0.038	0.054	1.81	3.67	0.98
	4	0.339	0.120	0.003	26.86	7.55	0.31
	5	0.246	0.260	0.128	9.98	7.99	4.39
	avg	**0.117**	**0.064**	**0.025**	**8.16**	**4.17**	**0.89**

A straightforward analysis of fibre orientation is present in Table 7. It reveals that in the fourth example, CNN3 predicts a value of φ at 21° ± 32°, while CNN7 predicts a value of φ at 127° ± 76°, which is much closer to the original value of φ at 154° ± 56°. However, CNN3 was able to generate volumes with statistically more prevalent physical metrics correctly, as seen in the first example where the physical metrics for CNN3 and CNN7 are similar. On the other hand, CNN5 has an intermediate average error that is closer to CNN3 than CNN7. Also, it worth to note, that the algorithms were able to identify the orientation of fibres correctly in the case 5 with a void and generated volume according to the information around the void.

Table 7 – Mean values and standard deviation of fibre orientations of the generated parts.

Angle, example		CNN3 ROI	CNN5 ROI	CNN7 ROI	Ground truth
φ	1	45 ± 5	45 ± 5	45± 4	44 ± 6
	2	54 ± 46	60 ± 48	63 ± 49	53 ± 41
	3	110 ± 22	113 ± 16	115 ± 26	103 ± 31
	4	21 ± 32	34 ± 56	127 ± 76	154 ± 56
	5	53 ± 7	55 ± 5	54 ± 4	53 ± 7
θ	1	75 ± 5	77 ± 4	74 ± 5	70 ± 5
	2	80 ± 10	83 ± 11	80 ± 10	78 ± 7
	3	75 ± 8	76 ± 10	78 ± 8	73 ± 12
	4	92 ± 9	97 ± 10	88 ± 9	79 ± 10
	5	75 ± 7	74 ± 5	70 ± 5	62 ± 6

The reason CNN7 is more accurate than CNN3 at predicting rare cases is due to its deeper neural network architecture and a larger number of trainable parameters. This means that CNN7 has a greater capacity to store information about recognised features in the analysed data. However, it is important to note that the number of trainable parameters also affects the amount of GPU memory required to fit the entire model, as shown in Table 8.

A comparison of GPU memory consumption showed that although CNN3 has fewer trainable parameters and poorer performance, its memory consumption is almost 17 times lower

than that of CNN7, allowing it to train larger micro-CT images. The performance of CNN5 is intermediate between CNN3 and CNN7, but its size is significantly smaller than CNN7. Despite higher hardware requirements, CNN7 shows the best performance due to a high number of trainable parameters.

Table 8 – GPU memory usage for a one-image batch.

Model	CNN3	CNN5	CNN7
Number of trainable parameters	3 780 738	15 455 106	62 948 738
Size of generator, MB	26	117	255
Size of discriminator, MB	18	61	482
One batch of GAN (8 images), MB	357	1424	5896

5.1.7 Conclusion

In this part of the PhD research, deep learning techniques were applied for the inpainting of CT images of random glass fibre composite. The dataset consisted of generated images based on micro-CT images of $300 \times 300 \times 900$ pixel^3 with a resolution of 4.4 μm. We developed and analysed three different encoder-decoder neural network architectures with varying numbers of convolutional layers (three for CNN3, five for CNN5, and seven for CNN7). The networks produce 3D microstructure representations of materials, a capability beyond the reach of classical 2D inpainting algorithms. Image-related and physical quality metrics were used to evaluate the performance of each network.

The results show that the deepest neural network (CNN7), with over 60 million trainable parameters, outperforms the other models, achieving a low average error of 0.4% for the degree of anisotropy and 2% for the orientation tensor in whole volumes. CNN3 and CNN5 show a higher image-related accuracy during generation, they showed high errors for physical metrics, up to 2 times higher than CNN7. However, CNN3 and CNN5 demonstrated correct fibre behaviour prediction in images similar to the dataset and achieved acceptable errors for physical metrics.

Furthermore, the high performance of CNN7 comes at the cost of high GPU memory usage, up to 17 times higher than CNN3. Therefore, the choice of architecture should depend on the consistency of the material structure, with CNN3 or CNN5 being preferred for inpainting large CT images of more consistently structured materials, and CNN7 being a suitable choice for randomly structured materials.

5.2 Super-resolution: quality enhancement of micro-CT images

5.2.1   Introduction

Super-resolution (SR) is a common task in computer vision that involves generating a high-quality, high-resolution (HR) image from a low-resolution (LR) image. There are several techniques available for SR, including interpolation-based, reconstruction-based, and machine learning-based methods. While interpolation-based methods are fast and simple, they often result in blurred images. Reconstruction-based methods are more accurate but require more computational resources [172]. On the other hand, deep learning-based methods leverage the power of deep neural networks to learn the mapping between low and high-resolution images, delivering high performance and speed. These techniques are already widely used in many fields, but they have not been widely employed in composite materials and are mostly limited to 2D cases. However, super-resolution can mitigate the impact of the resolution-to-sample size trade-off, but it may introduce an image quality-to-reality trade-off as the algorithm may generate new information not present in the original low-resolution data.

Super-resolution has the potential to be an invaluable tool for X-ray computed tomography, which is widely used to experimentally assess defect development during mechanical testing [23]. By enabling in-situ observation of damage development over time, CT allows for the chronology of defects to be studied. While lab-scale CT has been extensively used in the study of composite materials [39,173–177], it remains too slow to capture defects with the resolutions and representative strain rates required to detect structural features at the fibre-by-fibre level. As a result, synchrotron radiation computed tomography (SRCT) has been employed [178,179], but even with its high cost and complexity, it is only possible to observe defect evolution in small specimens (around 1 mm^3) at the desired high sub-µm resolution. For continuous in-situ scanning,

the image quality is significantly lower. Furthermore, increasing the X-ray flux and exposure time to obtain a higher-resolution 3D image of a specimen is not a feasible solution due to the inherent limitations of CT [180]. In addition, automated or semi-automated algorithms only work on high-resolution (HR) images, and it is extremely difficult to annotate fibre breaks in low-resolution and noisy images.

Improving the image quality of CT images of composite materials has become an important task in recent years. As mentioned above, one approach that has shown significant breakthroughs is the use of deep learning techniques, particularly convolutional neural networks (CNN) and generative adversarial neural networks (GAN), to generate high-resolution 2D images [181–183]. For example, the Enhanced Super Resolution GAN (ESRGAN) has demonstrated impressive enhancement results while requiring low computational overhead after training [184]. However, a major limitation of these super-resolution methods is the need for large amounts of ideally paired high- and low-resolution images for training, which can be difficult to obtain in the context of CT imaging. Furthermore, even when non-synthetic data is used, optical distortions can make it impossible to create a perfectly aligned 3D dataset due to small differences in feature locations [117]. To overcome this problem of data parity, the CycleGAN architecture has been proposed, which does not require paired datasets [185].

Super-resolution techniques have mainly been developed for 2D images and are only applicable in the slice direction for 3D images [186]. These methods can introduce inconsistencies in adjacent slices, which limits their effectiveness in analysing continuous features like fibres. Furthermore, they cannot consider information from other slices and generate information between them. A potential solution is to apply super-resolution to initial tomography projections prior to 3D image reconstruction [187], but this approach may not always be feasible due to the lack of

available projections. Recently, 3D super-resolution methods have emerged that utilize 3D filters to allow straightforward 3D image processing [181,188]. However, these techniques require significantly more data for training and hardware resources due to the deeper architecture. This increased complexity can lead to difficulties in training convergence and requires more advanced strategies to train the model properly. Nevertheless, the development of 3D super-resolution techniques promises to improve the analysis of composites by increasing the resolution of 3D images and allowing better tracking of the development of defects and damage over time.

In this section, it is proposed to use a combination of 3D modifications of ESRGAN and CycleGAN for CT image quality improvement, potentially enabling automated image analysis of composite microstructure and defects. The study was carried out for unidirectional carbon fibre/epoxy composite (T700SC) and short fibre composite (1000C). The quality of the super-resolution enhancement is evaluated using the PSNR and SSIM metrics. Verification of the SR implementation for material not included in the training dataset is investigated for fibre break identification in section 6.2. The use of deep learning techniques significantly improves the quality of the images and can help in the analysis of composite materials by reducing the time and manual intervention required for the identification of physical descriptors.

5.2.2   Developed algorithm

In this part of the research, a generative adversarial network was designed, trained, and used as a super-resolution algorithm. As in inpainting, the developed GAN consists of two networks, a generator and a discriminator, but they have different purposes. In this task, the objective of the generator was to increase image resolution: to produce a generated high-resolution image from an original low-resolution image. The purpose of the discriminator is to take the original and the generated high-resolution images as input, distinguish the original from the

generated and provide feedback to the generator. In this adversarial process, the generator attempted to fool the discriminator, while the discriminator attempted to identify when and how it was being fooled. As the training progressed, both neural networks produced increasingly better results.

Significantly modified convolutional neural networks were used for the generator and discriminator to implement the super-resolution algorithm. Specifically, the generator was based on the Enhanced Super-Resolution GAN architecture with residual-in-residual blocks [184]. This architecture was adapted to work with grayscale 3D CT images. Volumetric kernels were employed to upgrade it to the 3D case. The use of residual blocks ensured that information from the initial image was preserved throughout all layers of the network and contributed to the final high-resolution image generation. In addition, a classical convolutional network was used for the discriminator, consisting of four convolutional layers and a fully connected layer, to distinguish between the input image types (generated or true). Figure 23 provides a detailed overview of the generator and discriminator architectures used in this study.

The GAN architecture used in this study has been further improved using the CycleGAN methodology [185]. This approach allows the use of unpaired images for training, eliminating the need for pixel-level alignment between low-resolution and high-resolution data. Instead, CycleGANs enforce an inverse transformation, translating a low-resolution image to resemble a high-resolution image without paired constraints during training. This architecture introduces a low-resolution generator and implements the comparison between the generated (cycled) LR images and the original LR images. The use of such a GAN architecture helps to mitigate inconsistencies resulting from optical distortions, as the network can operate on unpaired data. The final network architecture employed over 8 million trainable parameters, as depicted in Figure 24.

The following loss functions were utilized for training the generator and discriminator: reconstruction, adversarial, and cycle losses.
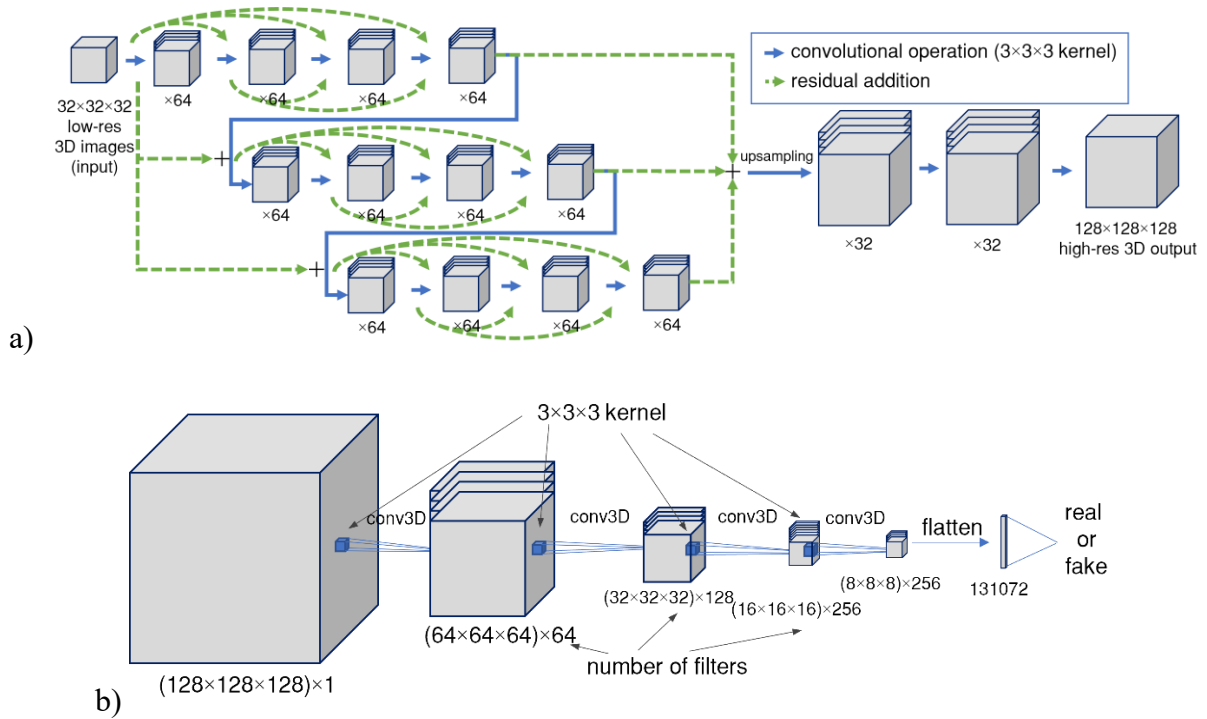
Figure 23 – Detailed graphical representation of neural network architectures: a) generator, and b) discriminator.
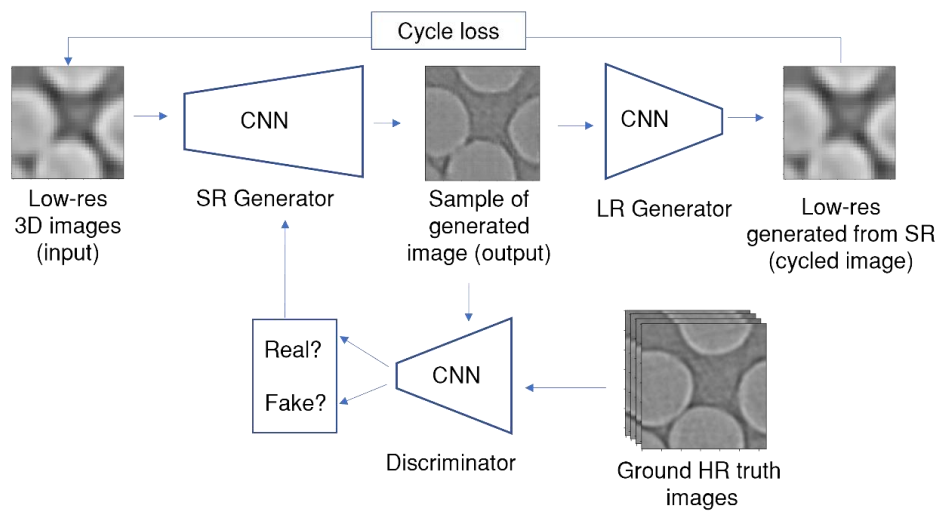
Figure 24 – Cycle Generative Adversarial Network for super-resolution of CT images of composite materials.

5.2.3   Implementation and data processing

The implementation of the deep learning architecture and training of models was carried out using Python 3.8 and the TensorFlow 2.9 framework [92] on a high-performance workstation equipped with a 12-Core Xeon 4214 processor, 16 GB Tesla V100 graphical card, and 64 GB of RAM. We applied a denoising algorithm to the CT image of the short fibre composite and blended it with the original image to reduce the noise level and enhance the image quality. However, we did not modify the image of the UD composite, as it already had a high quality and a low noise level.

Since deep learning and CT processing require significant computational resources, the CT volumes were split into smaller volumes with dimensions of $32\times32\times32$ pixel^3 for low-resolution images and $128\times128\times128$ pixel^3 for high- and super-resolution images. To ensure continuity between the volumes, an overlap of 3 pixels was used for low-resolution and 12 pixels for high-resolution images. Image augmentation, in the form of image jitter, was introduced as a means to artificially increase the amount of data available for training. In this technique, small training images are randomly shifted in all three directions by up to four pixels before each training step. This ensures that the model is not fed with identical batches of images and helps to improve its ability to generalize to new, unseen data. The training dataset comprised 4560 LR and HR small volumes for the dataset of unidirectional carbon fibre composite and 3150 for short glass fibre composite.

The ADAM stochastic gradient descent solver [151] was employed for model optimization with β_1=0.9. As during the training of inpainting algorithm, ADAM stochastic gradient descent was selected for its ability to efficiently handle noisy gradients, making it well-suited for the training dynamics of generative networks. Its adaptive learning rate and momentum mechanisms

help enhance convergence during GAN training. RMSE loss function was implemented for pixel-wise comparison between HR and SR images for training SR generator, and LR and generated LR images for LR generators. Relativistic average loss function (RaGAN) was used for the generator and the discriminator adversarial training process, L_G^{RaGAN} and L_D^{RaGAN} respectively [189]:

$$L_G^{RaGAN} = \mathbb{E}_{x_r \sim \mathbb{P}} \left[f_1 \left(C(x_r) - E_{x_f \sim Q} C(x_f) \right) \right] + \mathbb{E}_{x_f \sim Q} \left[f_2 \left(C(x_f) - E_{x_r \sim \mathbb{P}} C(x_r) \right) \right] \tag{12}$$

$$L_D^{RaGAN} = \mathbb{E}_{x_r \sim \mathbb{P}} \left[g_1 \left(C(x_r) - E_{x_f \sim Q} C(x_f) \right) \right] + \mathbb{E}_{x_f \sim Q} \left[g_2 \left(C(x_f) - E_{x_r \sim \mathbb{P}} C(x_r) \right) \right] \tag{13}$$

where f_1, f_2, g_1, g_2 are scalar-to-scalar functions, x_r is a real image of ground truth dataset $\mathbb{P}$, x_f is a fake image of the distribution of fake data $\mathbb{Q}$. $\mathbb{E}_{x_r \sim P}$ and $\mathbb{E}_{x_f \sim Q}$ denotes expectation over all population images x_r in $\mathbb{P}$ dataset and x_f in $\mathbb{Q}$ dataset respectively. $C(\cdot)$ is discriminator output (also sometimes called critic output).

RaGAN is employed in super-resolution due to its capacity to enhance the generator's ability to produce realistic high-resolution images by improving gradient flow and reducing training instability, ultimately leading to sharper and more visually accurate results. RaGAN loss function is widely recognised as an effective method of image generation and is often compared with Wasserstein GAN [190]. These loss functions evaluate "the probability that the input data is more realistic than a randomly sampled data of the opposing type (fake if the input is real or real if the input is fake)" as stated in [189]. The total loss function was computed as a weighted sum of all losses, with a cycle loss weight of 10 and a GAN loss weight of 1, as in [185]. The training was conducted using mixed precision [191]: all neural network training on GPU were done in half precision, but other calculations as input preparation and output analysis were done in full precision. This helped speed up the training process and reduce GPU memory consumption.

After training, the low-resolution volumes were enhanced using super-resolution techniques, and full-scale SR images were obtained. The overlap ensured that the enhancement was performed seamlessly across the entire volume as shown in Figure 25.
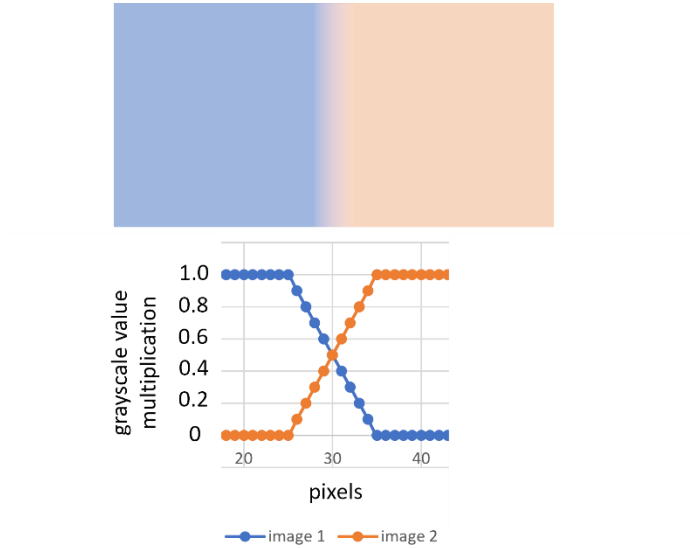
Figure 25 – 2D illustration of 3D stitching of small volumes during SR enchantment process

5.2.4   Validation criteria

Qualitative and quantitative assessments of image enhancement of super-resolution images were performed. In terms of qualitative analysis, the enhanced images were visually inspected to assess the improvements in resolution and clarity. In addition to the visual inspection, quantitative metrics were also calculated to provide a more objective measure of the improvements in image quality. The metrics used included mean squared error (MSE), peak signal-to-noise ratio (PSNR), and structural similarity index measure (SSIM). These metrics are image-related and provide a quantitative assessment of the level of noise reduction and enhancement of structural details in the enhanced images compared to the original low-resolution images [192].

The MSE and PSNR metrics have been used in the development of inpainting algorithms and have been introduced as (7). The Structural Similarity Index (SSIM) is another widely used

76

metric in image processing and computer vision applications that aims to improve traditional metrics such as MSE and PSNR by incorporating perceptual aspects of image quality. SSIM is a full reference metric that requires two images from the same acquisition process or scene as input. It measures the structural similarity between two images by comparing their luminance, contrast, and structure, and can be calculated using the following expression [193]:

$$SSIM(x, y) = \frac{(2\mu_x\mu_y + c_1)(2\sigma_{xy} + c_2)}{(\mu_x^2 + \mu_y^2 + c_1)(\sigma_x^2 + \sigma_y^2 + c_2)} \tag{14}$$

where μ_x and μ_y a pixel-wise mean of image x and y, respectively. Similarly, σ_x^2 and σ_y^2 are the variances of the two images, while σ_{xy} represents their covariance. The variables c_1 and c_2 are used to stabilize the division with a weak denominator, with $c_1 = (k_1 L)^2$ and $c_2 = (k_2 L)^2$, where k_1 and k_2 are constants, typically set to 0.01 and 0.03, respectively, and L is the dynamic range of pixel values, usually equal to $2^{bits\ per\ pixel} - 1$.

The effectiveness of the super-resolution algorithm was further validated by identifying physical descriptors in the enhanced CT images. In particular, Section 6.2 describes in detail how the super-resolution technique can be applied to a CT image that was not a part of the training dataset. Subsequently, automated algorithms were used to identify fibre breaks in the enhanced images, and it was found that the image enhancements did not result in any significant loss of analysis quality. The section demonstrates that the super-resolution algorithm not only improves the visual quality of CT images but also provides accurate and reliable physical descriptors for downstream analysis.

5.2.5　Results and discussions

To assess the quality of the super-resolution technique, we compared the enhanced images with the original high-resolution images and the low-resolution images that were upscaled using

bicubic interpolation. The technique was applied to two common structures of composites: unidirectional long fibre composite and short fibre composite. The super-resolution results for each structure are shown in Figure 26 and Figure 27, respectively.
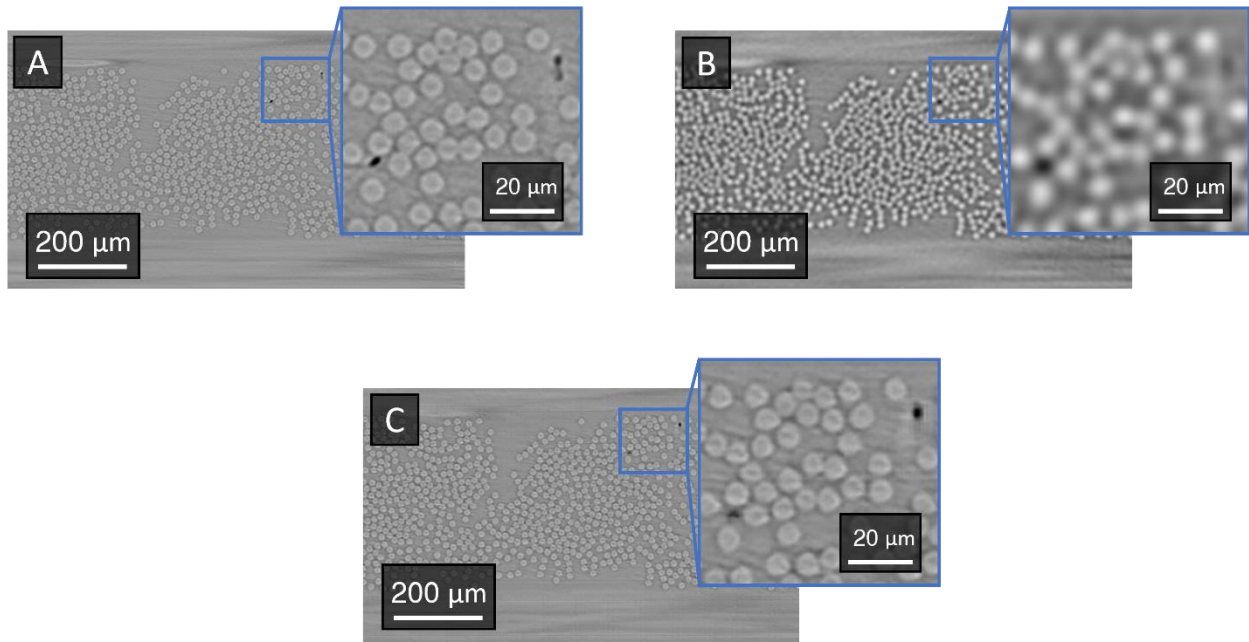
Figure 26 – SR results of image quality enhancements of UD composite materials: a) original HR image, b) interpolated LR image, c) enhanced SR image.

The images show that the super-resolution technique was effective in improving the quality of low-resolution CT images of the UD composites. The SR images are very similar to the HR images, except for some minor differences in edges or image texture. Moreover, the SR technique was able to correct some false voids near closely packed fibre, which appeared in LR images but not in HR images. These artefacts were avoided by the SR technique, unlike the bicubic interpolation method, which produced such image defects. Furthermore, the SR technique was able to restore a small volume on the top right corner of the scaled image example, which was barely visible in the LR images.
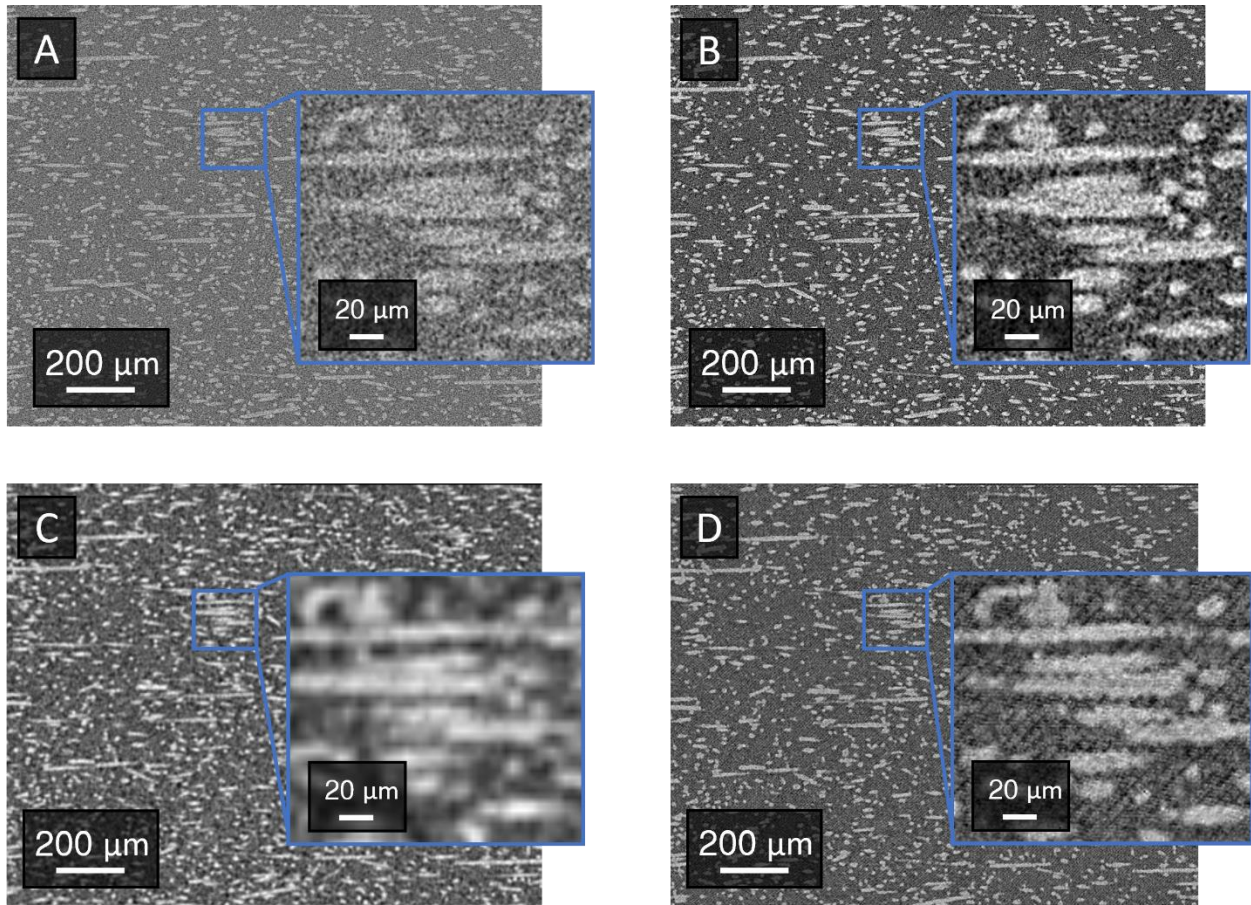
Figure 27 – Example of statistically representative images:
a) original HR noisy CT image, b) denoised HR image, c) original LR image, 4) super-resolution image

The super-resolution technique also produced good results for the short fibres, although there were some slight differences between the input (Figure 27b) and output (Figure 27d) images. Nevertheless, the technique was able to reconstruct the main composite microstructure without significant defects. The presence of textured defects in SR images can be attributed to the use of convolutional layers in neural networks. While it is feasible to mitigate these defects by fine-tuning training hyperparameters, it's essential to note that, for the purposes of this research, these defects have no significant impact on the accuracy of fibre analysis results. The SR images had a different image texture compared to the original images and the boundaries between fibres were clearer.

The enhanced fibre boundaries could facilitate the image processing, as the fibre identification would be easier to perform.

We wanted to examine how the SR model handled the generation of high-quality images of singularities, such as voids. We located such singularities in the original images and compared them with the SR images of UD composites. The enhanced images with singularities are shown in Figure 28.
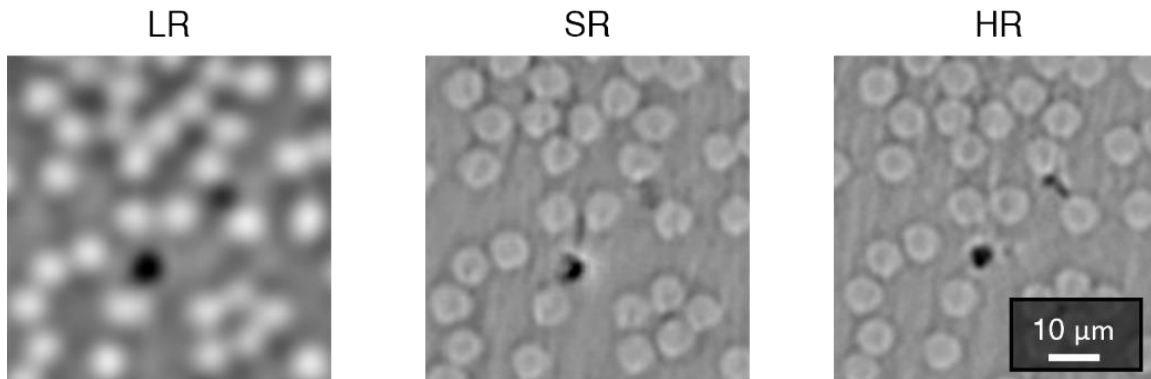
Figure 28 – Example of voids in the UD composites

The generation of singularities from LR images was not as good as the generation of common structures. For instance, the edges of some voids were not as sharp as in the HR images, or some voids that were smaller than the spatial resolution of the LR image were not reconstructed, because they lacked sufficient information in the LR image, or they were on the border of stitched volumes and not regenerated correctly.

We performed a quantitative analysis of the SR algorithm regeneration and presented the results in Table 9. HR images are used as the reference for the UD composite and the denoised HR image for the short fibre composite. Overall, the values in Table 9 shows the difference between the original HR images and other processed images.

Table 9 – Quantitative comparison of true HR image with noisy, LR and SR.

Image		MSE (lower is better)	PNSR (higher is better)	SSIM (lower is better)	Fibre diameter, μm
UD	Original	0	-	0	5.9 ± 0.5
	LR (interpolated)	403	50.1	0.12	5.8 ± 1.3
	SR	98	62.4	0.23	5.9 ± 0.8
SGFC	HR noisy	889	43.3	0.91	-
	LR (interpolated)	1883	36.7	0.11	-
	SR	1416	39.3	0.15	-

The metrics indicate a significant quality improvement after applying the SR technique to the LR images of the UD composite material, as they have a more consistent material structure. We observe a small MSE error and a high PSNR metrics for SR images compared to other images, which imply a high visual similarity between HR and SR images. The SSIM is relatively low (SSIM equal to 1 indicates perfect similarity, and 0 is no similarity), which reflects the difference in image texture. The short fibre composite case is harder to compare quantitatively due to its random structure. Even the original noisy image has worse results in MSE and PSNR, but a good SSIM metric. However, the SR image metrics are much better than the interpolated images in terms of MSE, PSNR and SSIM, but not perfect.

Fibre segmentation and diameter analysis, discussed in detail in Chapter 5.3, uses deep learning segmentation and ImageJ software. The results reveal that super-resolution significantly improves the accuracy of diameter calculations, aligning closely with the actual measurements of 6 μm, and SR demonstrates superior standard deviation results compared to low-resolution image analysis.

5.2.6   Conclusion

This PhD project focuses on the development of an advanced deep learning-based algorithm to improve the quality of images obtained from synchrotron and lab-scale CT scans. A super-resolution algorithm has been designed and applied to significantly improve the quality of low-resolution images of UD and short fibre composites. The algorithm relies on deep learning techniques, such as the Enhanced Super-Resolution GAN and CycleGAN, to regenerate high-resolution images with greater accuracy and detail. High-resolution and low-resolution scans of stationary carbon fibre composites and short fibre composites were used to train the neural networks.

The resulting super-resolution images show a significant visual improvement in the precision of fibre and void boundaries, with only minor deep learning-based artefacts. Image generation metrics indicate good image similarity between SR and original HR images, confirming the effectiveness of the proposed approach.

This algorithm allows researchers to use faster, low-resolution in-situ CT scans on continuously loaded specimens with only minor accuracy compromise of physical parameter identification. In addition, super-resolution algorithms have the ability to replace multiple post-processing techniques such as denoising and contrast enhancement, streamlining the image enhancement process and providing more accurate and visually enhanced results. The potential of super-resolution extends to improving segmentation accuracy by providing finer image detail, facilitating sharper object boundary delineation, and ultimately improving the overall quality of segmentation results. The development of this deep learning-based algorithm promises to advance the field of CT imaging of composite materials, providing researchers with the opportunity to obtain increasingly detailed and accurate images.

5.3 Segmentation: analysis of machine and deep learning tools for object identification

5.3.1   Introduction

While obtaining CT images of the highest possible quality can be considered a priority task, another, equally important task is to analyse the images accurately. CT images are data rich, so researchers tend to extract as much useful information as possible from the images. One of the main tasks in the analysis is to perform segmentation: to identify the objects of interest, in our case fibres, matrix and voids. Accurate segmentation of fibres, matrix and other physical descriptors in composites is of paramount importance, as it allows accurate characterisation of the microstructure of the material, which is critical for improving its mechanical properties and determining its strength within the composite.

The simplest segmentation is threshold segmentation, which separates an image into two parts: the background and the foreground. However, when the microstructure has low contrast, a complex shape, or different image textures for different sections or different times for in-situ testing, classical algorithms such as thresholding and others may not be sufficient for accurate segmentation. To overcome these limitations, the field is moving towards machine and deep learning techniques, which promise much better segmentation quality for fewer computational resources.

This section is devoted to the analysis of existing segmentation algorithms. There are several proprietary and open-source software packages that provide machine and deep learning segmentation [194]. The main difficulty in using such packages is that most of them are dedicated to biological or medical applications and have been trained to segment different structures and cannot be easily applied to composite materials. Several packages offer a training option to use a new dataset of label images to train the model, but there can also be difficulties in setting up

modern deep learning frameworks for this software. For example, CSBDeep [195] was implemented using the TensorFlow framework written in Python and distributed in ImageJ plugin format as a Java program, which increases incompatibility issues on some machines. Weka segmentation [106] and RootPainter [107] software offers a convenient way to create labelled data and train models within one package, making them an easy choice to perform segmentation on new data.

5.3.2   Selected algorithms

To evaluate the segmentation algorithms for easy, fast, and accurate segmentation of physical descriptors from CT images used in this research, we selected a machine learning-based algorithm, a deep learning algorithm and a popular non-ML algorithm. All selected algorithms were compared with thresholding. This is the simplest method of image segmentation. Thresholding divides an image into just two classes of pixels, 'foreground' and 'background'. The process involves setting a threshold value that separates the two classes of pixels. Pixels with values above the threshold are classified as foreground pixels, while those below the threshold are classified as background pixels.

Machine learning segmentation is based on narrow learning algorithms such as random forest [196]. One of the practical tools that implements ML segmentation is "Trainable Weka segmentation", which is provided as a plugin to the popular image processing tool ImageJ (Fiji [112]). The plugin used in this study uses a set of machine learning algorithms and a carefully curated feature list to generate pixel-level segmentations. It uses the Weka software and can be trained using user input, ultimately producing a labelled output based on the training of the chosen classifier.

For this study, a FastRandomForest [197] was chosen as the main ML algorithm for Weka segmentation as it delivers good performance while consuming minimal computational resources. The segmentation is carried out by analysing up to 20 image features that can be chosen manually by the user. The available image features for Weka segmentation are presented in Figure 29.
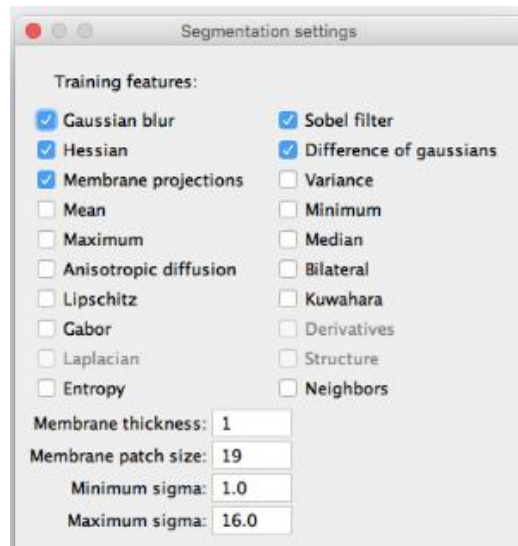
Figure 29 – The list of features in Trainable Weka Segmentation with default options selected.

The image features are computed for each pixel by considering both the pixel itself and its neighbours within a given window. The plugin generates a stack of images, with each image corresponding to a particular feature. For example, if Gaussian blur is selected as the feature, the plugin trains the classifier using the original image and several blurred versions of it, each with different σ parameters for the Gaussian. The ML algorithm then classifies each pixel based on the calculated image features. To achieve the most accurate segmentation, the parameters of the ML algorithm and the computed features can be fine-tuned. Details on how to optimise these parameters are given in section 5.3.4.

The second selected algorithm, U-Net – a widely popular deep learning model, was first introduced by Ronneberger et al. [198] and has since been extensively used in many fields. One

such implementation of this network is RootPainter, which was initially designed to detect roots in biological images but can be adapted for other purposes owing to its user-friendly graphical interface. The software is open-source and built on the PyTorch framework, which can be easily installed on suitable GPUs. The U-Net model used in RootPainter comprises the same number of layers and dimensions as the original U-Net with minimal modifications. Furthermore, RootPainter features corrective annotation, which enables the input of labelled data during training to enhance the accuracy of the model's segmentation results.

RootPainter has a limited number of tuneable parameters, such as the lack of options to adjust the prediction threshold or output prediction maps (which can be critical to accurately segmenting composites and adjusting the segmented volume fraction). However, as it is open source, researchers have the flexibility to modify the code to suit their specific requirements. For example, during this research the generation of probability maps were implemented in RootPainter, Probability maps represent the likelihood of an object being present in an image at this exact place, their usefulness is described in Chapter 6. For this implementation, the 0.5 prediction threshold after the prediction calculation was removed and the generation of NumPy arrays was added for easy analysis using Python. This change allows for a more refined analysis of the prediction maps and greater control over the segmentation process.

In addition to the FastRandomForest and U-Net models, we included a widely used non-ML algorithm [199], called InSegt, in our comparative analysis to evaluate different segmentation approaches. InSegt also involves a training phase but does not rely on machine learning algorithms. Instead, the algorithm uses a content-based propagation technique that utilises user markers to propagate segmentation labels to other parts of the image. A notable advantage of InSegt is its easy-to-use implementation, with no strict hardware requirements or software dependencies,

unlike deep learning methods. The algorithm has also been extended to analyse CT images and identify fibre centres in composite materials while calculating fibre trajectories [22].

5.3.3   Metrics

We evaluated the segmentation performance quantitatively using two metrics: Pixel Accuracy (PA) and Intersection over Union (IoU).

PA is a widely used metric in semantic segmentation that measures the accuracy of pixel-level classification. It is computed by dividing the number of correctly classified pixels by the total number of pixels in the image. This metric provides a percentage value that represents the overall accuracy of the segmentation model's predictions:

$$PA = \frac{\sum_{j=1}^{k} n_{jj}}{\sum_{j=1}^{k} t_j} \tag{15}$$

where he parameter n_{jj} in Pixel Accuracy (PA) represents the count of pixels that are correctly classified as class j. Put differently, it denotes the total number of true positives associated with class j. Meanwhile, the parameter t_j refers to the overall count of pixels that are labelled as class j in the image. By using these definitions, we can precisely calculate PA and measure the accuracy of pixel-level classification in an image. PA is a fundamental metric as it directly assesses pixel-level classification accuracy, providing insights into the accuracy of pixel classification in an image.

Intersection over Union (IoU) is a commonly used metric for evaluating the accuracy of semantic segmentation. It measures the degree of overlap between the predicted segmentation and the ground truth by calculating the intersection of the two areas divided by their union. The resulting IoU value ranges from 0 to 1, with a higher value indicating better segmentation performance. The IoU can be computed using the following equation:

$$IoU = \frac{TP}{TP + FP + FN} \tag{16}$$

where TP refers to true positives, which are the number of pixels correctly classified as belonging to the target class. Meanwhile, FP (false positives) represents the number of pixels incorrectly classified as belonging to the target class, and FN (false negatives) represents the number of pixels that should have been classified as belonging to the target class but were not. IoU is widely accepted for its ability to assess the spatial agreement between segmentation results and true object boundaries.

For image processing tasks, especially those involving the analysis of large datasets such as CT scans, the execution time of a segmentation algorithm is an important metric to consider. It refers to the time required for the algorithm or model to process one or more images and produce the corresponding labelled output. Given the potentially long processing times even on powerful workstations, optimising the execution time is crucial to ensure the practical applicability and scalability of the segmentation approach.

The preference for PA and IoU is due to their meaningful representation of pixel classification and spatial overlap, which are fundamental to segmentation tasks. These metrics are widely accepted in the research community for their clarity and interpretability. However, the specific requirements of a task and dataset should also be considered, and alternative metrics such as Dice coefficient, F1 score, and memory-related metrics may be relevant depending on the context.

5.3.4 Comparison

To optimise the parameters of the Trainable Weka Segmentation plugin, we evaluated the segmentation quality in relation to the processing time. The default setting was kept of sigma size for each possible image feature, which we found to be the most optimal. We then selected the most

efficient features and included them in the FastRandomForest model to segment the selected image. Table 10 summarises the selected features. To selection of these feature was based on time of execution and the additional information is added to the analysis. As for the RootPainter and InSegt software, we used the default settings as they were found to be the most optimal.

The comparison of the methods was carried out using two high HR and LR semi-manually annotated images of UD and short fibre composites, which were not included in the training dataset. The comparison was based on visual inspection and quantitative evaluation using specified metrics. The images used for the comparison, along with their corresponding manually annotated counterparts, are presented in Figure 30.

Table 10 – Analysis of image features in Weka segmentation, with * marked the selected features.

Feature	Time, s	Results	Feature	Time, s	Result
Gaussian blur*	1.84		Sober filter*	2.5	
Hessian*	2.8		Difference of gaussians*	2.5	
Membrane projection	7.8		Variance	2.3	
Mean*	1.5		Minimum	1.9	
Maximum	2.3		Median	2.3	
Anisotropic diffusion	30.9		Bilateral	5.6	
Lipschitz	3.2		Kuwahara	20.4	
Gabor	18.2		Derivatives*	2.8	
Laplacian*	2.2		Structure*	2.5	
Entropy	18.3		Neighbours*	3.2	
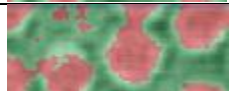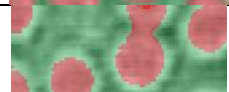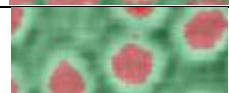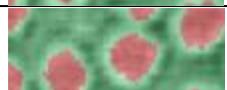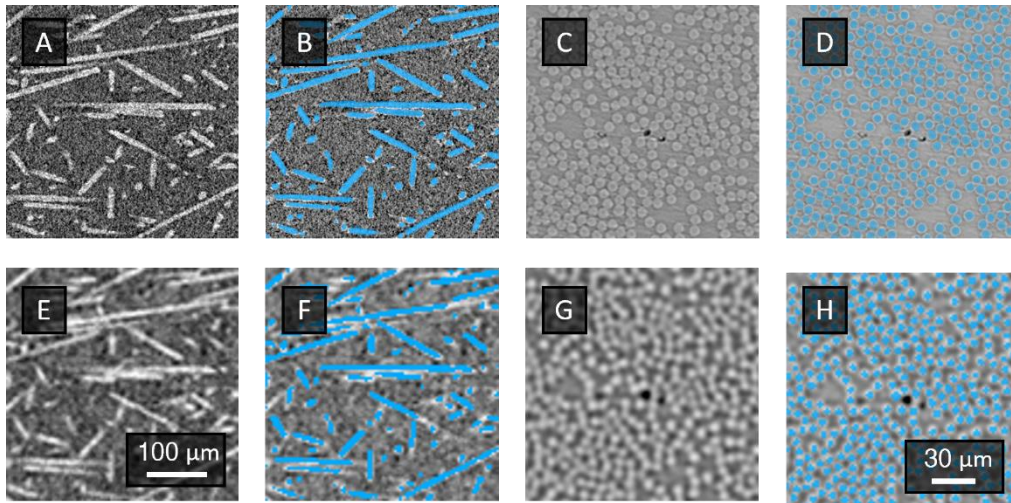
Figure 30 – The original images selected for segmentation analysis, along with their corresponding semi-manually segmented images: a) HR image of SGFC, b) segmented HR image of SGFC, c) HR image of UD composite, d) segmented HR image of UD composite, e) HR image of SGFC, f) segmented HR image of SGFC, g) HR image of UD composite, h) segmented HR image of UD composite

The algorithms were trained on labelled data consisting of examples of identified fibres and matrixes. The training was conducted separately for each type of image: 1) HR image of UD composite, 2) LR image of UD composite, 3) HR image of short fibre composite, 4) LR image of UD composite. The labelled data was supplied to the models until no further improvements were observed and time for labelling was calculated. The results are presented in Figure 31.

As shown in Figure 31, all three algorithms were able to identify fibres in HR images of UD composites, which is not a difficult task due to their high contrast and clear edges. Deep learning segmentation produced almost perfect results, accurately identifying the round shapes of the fibres. Weka segmentation also produced good segmentation results, although it struggled to maintain the exact shape of the fibres, as it is a pixel-based segmentation method that does not take into account the shape of the identified objects. The InSegt algorithm tended to reduce the occupied area as it was designed to identify fibre centres rather than their full shape. For LR images of UD composites, the deep learning segmentation gave the best visual results, although it had occasional

errors of fused objects and inconsistent shapes. ML segmentation of LR images of UD composites gave only moderate results with many fused objects. InSegt performed well but struggled with dense fibres. However, the performance of InSegt was on par with ML segmentation. Threshold segmentation yielded inaccurate results that could not be used for further image processing.

The HR images of the short fibre composite were segmented well by the deep learning-based algorithm, accurately identifying the shape of the fibres and keeping all objects separate. ML segmentation also produced good results, with occasional fused objects. However, the InSegt algorithm had difficulty maintaining segmentation quality and was unable to separate objects due to its design for patterned data segmentation, struggling with random microstructures. For low-resolution (LR) images, even the DL algorithm was unable to maintain good segmentation quality. The quantitative metrics are shown in Table 1.

Table 11 – The quantitative analysis of segmentation algorithms and time of execution.

	Algorithm	PA	UoI	Fibre diameter, μm	Time, min		
					labelling	training	volume processing
HR UD	RootPainter	0.990	0.957	5.9 ± 0.5	15	40	5
	Weka	0.875	0.768	6.1 ± 1.7	10	1	20
	InSegt	0.759	0.603	5.4 ± 0.8	10	0.2	1
	Threshold	0.729	0.487	6.7 ± 4.8	-	-	1
HD SGFC	RootPainter	0.963	0.871	-	30	30	5
	Weka	0.905	0.715	-	20	1	20
	InSegt	0.864	0.560	-	15	0.2	1
	Threshold	0.843	0.553	-	-	-	1
LR UD	RootPainter	0.800	0.534	5.8 ± 1.3	10	10	1
	Weka	0.779	0.485	5.9 ± 2.1	8	0.5	4
	InSegt	0.763	0.451	5.5 ± 2.0	5	0.2	0.25
	Threshold	0.764	0.438	6.8 ± 3.7	-	-	0.25
LD SGFC	RootPainter	0.780	0.441	-	30	15	1
	Weka	0.835	0.515	-	10	0.5	4
	InSegt	0.814	0.433	-	10	0.2	0.25
	Threshold	0.760	0.370	-	-	-	0.25
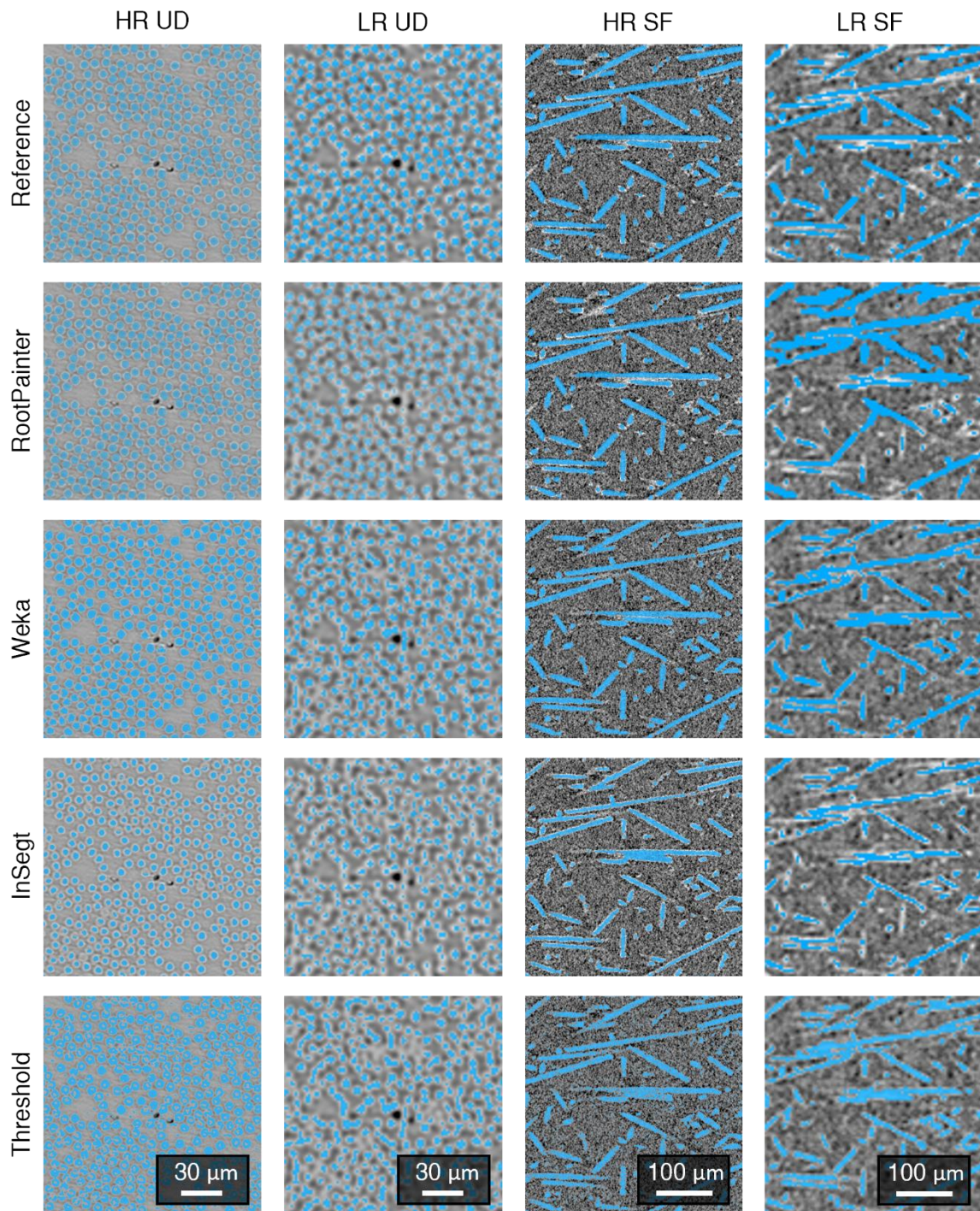
Figure 31 – Results of segmentation of validation image as reference using 3 selected algorithms: the first column is HR images of UD composites, second – LR images of UD composite, third – HR images of short fibre composites and the last column is LR images of short fibre composite.

The evaluation metrics support our visual inspection of the segmentation results, with RootPainter showing the highest accuracy of the tools evaluated, despite requiring GPU hardware. It is worth noting that the InSegt algorithm is significantly faster than ML algorithms, as it is based on simpler computations. Weka Segmentation, on the other hand, was the slowest tool due to the need to generate a new feature image to analyse at each iteration. Due to its long execution time, Weka Segmentation is not recommended for analysing large image datasets such as CT scans of composite materials. Based on the results, it can be suggested that deep learning-based segmentation of images enhanced by SR may achieves comparable segmentation quality to that of HR images. This topic will be discussed in detail in Chapter 6.

ImageJ analysis of fibre diameter in UD composites as a physical descriptor revealed the superior accuracy and consistency of deep learning, with the lowest standard deviation among methods. Weka, employing machine learning, also performed well but had a slightly higher standard deviation. InSegt tended to underestimate diameter by preventing objects from touching, while thresholding showed the least favourable results due to an inability to segment within fibres, artificially inflating their diameter.

All of these methods require retraining for each new dataset. This is essential because it allows the model to adapt to the different features, characteristics, and variations specific to each dataset. Training is the means by which the model learns to extract relevant patterns and structures, ensuring accurate and context-specific segmentation results for each dataset.

5.3.5   Conclusion

This section presents a comparative analysis of deep learning, machine learning and non-ML techniques to improve segmentation quality. To evaluate the segmentation algorithms they were compared visually, in addition, pixel accuracy and intersection over union metrics were used

to quantify the percentage of correctly classified pixels and the percentage of overlap between the target mask and the prediction output. The study focused on HR and LR images of composite materials and compared three image segmentation tools. While all tools performed well on HR images, ML-based and InSegt algorithms struggled with LR images. Conventional segmentation algorithms are beneficial in straightforward cases where image objects are easily distinguishable. RootPainter proved to be the most accurate tool with a fast execution time, although it requires GPU hardware. In contrast, Weka segmentation was slow and impractical for large datasets. However, the limitations of deep learning segmentation, compared to other methods, include a higher demand for labelled data, computationally intensive training, susceptibility to overfitting in small datasets, and the "black box" nature of deep neural networks, which can make the interpretation of results challenging.

5.4 Conclusion

The PhD research focuses on the development and implementation of deep learning algorithms specifically adapted to improve the quality of computed tomography images of composite materials.

The first part of the chapter focuses on the application of deep learning techniques to the inpainting of CT images of random glass fibre composites. The aim is to develop and evaluate three encoder-decoder neural network architectures based on both image-related and physical quality metrics. The results showed that the deepest neural network, CNN7, with over 60 million trainable parameters, outperformed the other models in inpainting large CT images of randomly structured materials. However, CNN3 and CNN5 correctly predicted fibre behaviour in images similar to the dataset and achieved acceptable errors for physical metrics. The choice of architecture should depend on the consistency of the material structure. For inpainting large CT

images of more consistently structured materials, CNN3 or CNN5 would be preferred, while CNN7 is a suitable choice for smaller volumes of more complexly structured materials. Overall, the developed algorithm can serve as a basis for other generative deep learning algorithms for various tasks, such as periodic structure generation, which will be demonstrated in the next chapter.

As part of a PhD project, a second algorithm was developed to improve the quality of images obtained from synchrotron and lab-scale CT scans. This algorithm focuses on super-resolution, using deep learning techniques such as Enhanced Super-Resolution GAN and CycleGAN to significantly improve the quality of low-resolution images. The resulting super-resolution images show a significant visual improvement in the precision of fibre and void boundaries, with only minor deep learning artefacts. The benefit of this algorithm is that it allows researchers to use faster, low-resolution in-situ CT scans on continuously loaded specimens without compromising the quality of physical parameter identification. One of the most important applications of this algorithm is the more accurate automated identification of physical descriptors of composite materials, such as fibre breaks, which is discussed in the next chapter.

The third section of this chapter presents a comparative analysis of deep learning, machine learning and non-ML techniques to improve the segmentation quality of high-resolution and low-resolution images of composite materials. Three image segmentation tools were compared based on the visual comparison, pixel accuracy and intersection over union metrics. The results showed that the deep learning technique implemented by RootPainter software was the most accurate tool with a fast execution time, although it requires GPU hardware. Machine learning based segmentation using Weka software was accurate but slow and impractical for large datasets. InSegt algorithms worked well to segment patterned images such as CT scans of UD composites. However, ML-based and InSegt algorithms struggled with low-resolution images, while all tools

performed well on high-resolution images. Overall, the study found that deep learning was the best tool for the segmentation of composite CT images. It offered the highest accuracy and efficiency compared to other approaches.

The study helps to overcome the limitations of CT imaging techniques and traditional image processing tools by using deep learning techniques. These techniques are capable of improving the usability of CT images of composite materials, which are critical for the design and analysis of these materials. The algorithms developed in this PhD research provide a comprehensive framework that enables researchers to obtain detailed and accurate CT images of composite materials and can be applied to various engineering applications.

Chapter 6. Applications developed methods to composite materials.

The field of composite materials relies heavily on the use of CT images for various purposes, such as defect detection and analysis, and the creation of finite element models for mechanical property calculations. Obtaining high-quality CT images is crucial for accurate analysis. In this chapter, we will explore a practical implementation of the deep learning algorithms developed and analysed in the previous chapters.

The first section focuses on the calculation of the mechanical properties of short fibre composites, where we use a modified inpainting algorithm to generate periodic structures. This section provides a detailed explanation of how the algorithm works and its effectiveness in improving the accuracy of mechanical property calculations.

In the second section, we discuss the use of super-resolution methods to identify fibre breaks from low-resolution scans of unidirectional composites. This approach will enable fast and automated fibre break identification algorithms, making the analysis of such damage much more efficient.

6.1 Finite-element micro-CT-based modelling with periodic boundary conditions

6.1.1 Introduction

Finite Element Analysis (FEA) is a widely used numerical technique for simulating the behaviour of composite materials under different loading conditions. FEA is well established and widely used for the multiscale characterisation of composites with any microstructure, making it a valuable tool for understanding the nature of materials. A common objective of FEA in composite simulations is to obtain homogenised properties that can be used in concurrent or further analysis methods. The microstructure is represented by a representative volume element. The RVE can

represent a large mechanical system and is often used to capture the heterogeneity of the material. Different methods for obtaining the geometry of the RVE have been discussed in Section 2.1.6.

CT can provide detailed information about the geometry and density distribution of materials, which are essential inputs for finite element modelling. By incorporating CT data into finite element models, researchers can capture the realistic microstructure and defects of materials, resulting in improved accuracy and reliability of the generated RVEs. CT can also be used to validate the results of finite element modelling by comparing simulated and experimental deformation and damage patterns. CT and finite element modelling are complementary tools that can enhance the understanding and optimisation of composite materials.

Periodic boundary conditions (PBCs) are a popular choice among researchers for simulating the behaviour of composite materials. PBCs are a technique for imposing continuity and compatibility of strains and stresses on the boundaries of a representative volume element (RVE) of a composite material [200]. This approach can reduce the size of the finite element model and ensures that the RVE is representative of an infinite, complex medium. PBCs can account for the effects of microstructural features such as fibre orientation, geometry, and interface properties on the overall behaviour of the composite [45].

However, PBCs also have some limitations and challenges for composite models. For example, PBCs require the RVE to have a periodic microstructure, which may not be realistic for some composites with random or irregular fibre distributions [201]. The periodicity of the microstructure may be violated if damage or large deformations appear. In addition, PBCs can be difficult to implement in finite element software and may require special algorithms or user-defined subroutines.

In this section, deep learning algorithms are proposed to alleviate some of the challenges associated with periodic boundary conditions and their implementation in finite element simulations of short fibre composites based on CT images. First, the mathematical formulation of periodic boundary conditions and their finite element implementation in the Abaqus software is discussed. A rigorous RVE size determination is also provided to ensure that the RVE is large enough to describe the mechanical properties of the material. To address the challenges of PBC implementation, we provide a methodology for integrating a modified inpainting neural network, super-resolution, and DL segmentation into the RVE creation workflow. Finally, we present the results of test simulations to demonstrate the effectiveness of our proposed pipeline for CT-based simulation of short fibre composites with periodic boundary conditions using deep learning methods. Our approach shows promising results in accurately capturing the behaviour of short-fibre composites under various loading conditions.

6.1.2   Periodic boundary conditions: formulation and implementation in FEA

The conventional mathematical models used to simulate the mechanical behaviour of fibre composite materials are typically based on a number of underlying assumptions that depend on the specific properties being investigated. In this research, the approach is illustrated on an example of isotropic fibres, avoiding introduction of complex algorithms for identification directionality of objects, segmented out from CT images. Also, we have made the following assumption: the effects of fibre/matrix debonding, interfacial slippage and microcracking within the matrix are not taken into account: the fibres and matrix remain bonded at their interface during deformation.

To obtain more accurate predictions of the mechanical properties of short fibre composites, researchers seek to represent an RVE as a volume with a pseudo-periodic structure and use periodic boundary conditions [45,67,201,202]. However, the heterogeneous nature of short fibre

composites means that the short fibres themselves cannot have a true periodic structure and non-physical stress and strain fluctuations can occur at the boundaries of the RVE. To address this issue, a methodology for creating an RVE with a periodic structure has been developed and will be discussed in detail later in this chapter.

The following short formulation of periodic boundary conditions is based on the lectures of Prof. Lomov [203]. To introduce this formulation, we consider a heterogeneous periodic medium subjected to external loads of characteristic length L. Within this medium, we can identify a periodic cell (RVE, in our case) with l_i which denotes the length of the RVE in the i-direction between opposite surfaces. If the periodic volume is affected by mass forces f, stresses σ are introduced in the medium. The equilibrium equations for this volume can be written as follows:

$$\sigma_{ij,j} = -f_i \tag{17}$$

To extend these equations, we can utilise Hooke's law in the form of a stiffness matrix, which takes into account the size and coordinates of the RVE [67]:

$$\left(C_{ijkl}\left(\frac{\mathbf{x}}{\alpha}\right) u_{k,l} \right)_{,j} = -f_i(\mathbf{x}) \tag{18}$$

In the above equation, $\mathbf{C} = \mathbf{C}(\xi) = \mathbf{C}\left(\frac{\mathbf{x}}{\alpha}\right)$ is a stiffness function that depends on periodic value $\mathbf{x}$ with period α, and C_{ijkl} is the stiffness matrix. $\xi_i = \frac{x_i}{\alpha} = \frac{X_i}{l}$ is a "fast" variable that is related to the cell coordinate system, where x_i is the ratio of X_i-numbered coordinates in the global coordinate system to the characteristic size of the medium L.

To solve equation (18) we take into account the variability of the right and left sides of the equation and use the asymptotic method of averaging. However, due to the length and complexity of the solution, it is not presented in this thesis. Interested readers may refer to [67] for the complete solution.

Using the asymptotic averaging method, we can obtain the zero approximation of the solution to equation (18), which enables us to determine the stiffness matrix of the homogenised medium:

$$\langle C_{ijkl} \rangle = \frac{1}{V} \int\limits_V C_{ijpq}(\xi) U_{pkl|q}(\xi) d\xi = \frac{1}{V} \int\limits_V \sigma_{ij}^{(kl)}(\xi) d\xi \tag{19}$$

$$\sigma_{ij}^{(kl)}(\xi) = C_{ijpq}(\xi) U_{pkl|q}(\xi)$$

The pseudo-displacement U_{ipq} and the pseudo-stress $\sigma_{ij}^{(kl)}$ are obtained as solutions to the elasticity boundary value problems within the periodicity cell:

$$\left(C_{ijkl}(\xi) U_{kpq|l}(\xi) \right)_{|j} = 0 \tag{20}$$

with the following general kinematic formulation of periodic boundary conditions:

$$U_{ipq}^{(2)}(\xi) - U_{ipq}^{(1)}(\xi) = \frac{1}{2} \left(\Delta \xi_q \delta_{ip} + \Delta \xi_p \delta_{iq} \right) \tag{21}$$

where free indices p, q identify the possible boundary problem.

Equation (21) signifies the importance of maintaining the continuity of displacements and stresses at the boundaries between adjacent unit cells to prevent interpenetration or abrupt changes. It is imperative to ensure that the displacement and stress fields remain smooth and continuous throughout the composite material.

Figure 32 can be used to illustrate the implementation of PBC in a three-dimensional FE model of a cuboidal RVE. To express the general kinematic PBC formulation in FEA, a relative formulation involving nodal displacement constraints can be used, as demonstrated in previous studies [204]. This relative displacement is then used to apply appropriate nodal displacement constraints to the nodes of one face to enforce periodicity with the corresponding nodes on the opposite face.

$$U_j^{(2)} - U_j^{(1)} = \varepsilon_{ij}^0 l_i \tag{22}$$

the term ε_{ij}^0 represents the macro-strain tensor of the RVE.

The application of periodic boundary conditions (PBC) in FE packages such as Abaqus, as specified in equation (22), can result in over-constrained models when PBCs are applied to entire surfaces. This occurs because the behaviour of edges and vertices is described multiple times, as shown in Figure 32. The system would not be mathematically over-constrained, as several equations in the set are fully equivalent. However, this problem still prevents the FE solver from running and simulating the mechanical behaviour of the material.

To avoid this problem during simulation in FE packages, it is necessary to explicitly define constraints for interior points of faces, edges and vertices when applying BCs. Each constraint specifies the displacement between two symmetric points (with respect to the XY, XZ, and YZ mid-planes) as previously described in the PBC formulation.

Figure 32 shows the distribution of periodic boundary conditions, where the red lines and dots represent the fixed nodes on edges and vertices, respectively. The green arrow and edges indicate the application of edge periodic boundary conditions, while the blue arrow and dots indicate vertex periodic boundary conditions.

Dummy nodes are reference points in finite element modelling that are not attached to the model and allow different boundary conditions to be easily applied. Different boundary conditions can be applied to the dummy node for different load cases. If there is no displacement of the dummy node, the solver treats it as if it were under free stress conditions, allowing the Poisson effect to be considered in different directions.
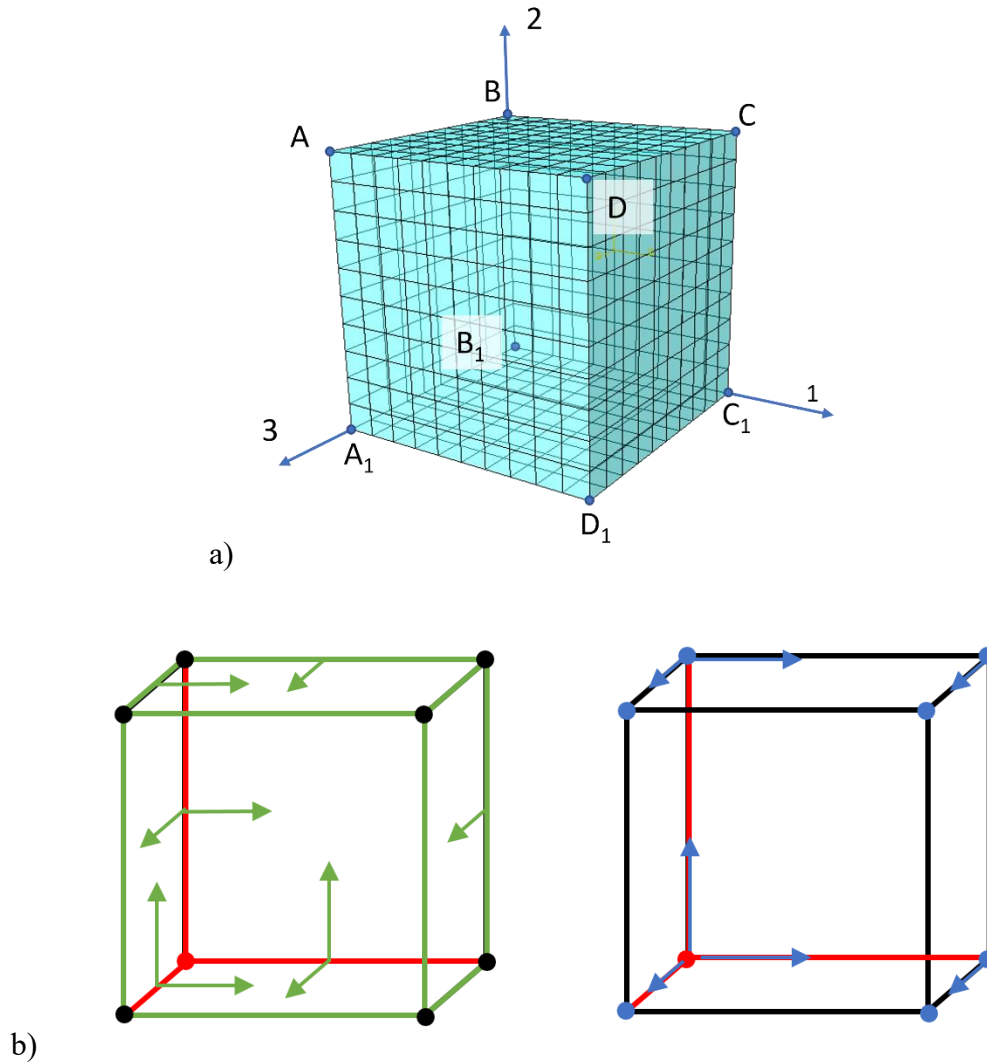
Figure 32 – Kinematic relative formulation of periodic boundary conditions: a) representation of notation on RVE cube, b) edge and vertices treatment.

Given the constant initial dimensions l_i of the RVE the displacement of a dummy node $\widehat{U}_j^i$ can be used to represent the right term of the equation (22) $(\varepsilon_{ij}^0 l_i)$ in the form of reference points. To implement the PBC constraints, a dummy node with three displacement components j is used for each direction i connecting nodes of opposite surfaces. This allows an easy implementation of PBC constraints in the Abaqus software (or any other FE solver) where the macro-strain tensor is defined as the displacement components of these reference points [204,205].

Table 12 shows the equations for applying PBCs to the RVE, grouped for clarity into internal nodes, edges (excluding vertices), and vertices as it was done in [204]. The notation follows vertex nomenclature from Figure 32. Three equations are required for internal surface nodes, nine for edge nodes, and seven for vertices. Table 12 displays a set of equations arranged in a node-to-node coupling format, which relies on a conformal mesh where every node on one surface has a corresponding node on the opposite surface.

Table 12 – Kinematic relative formulation of periodic boundary conditions.

Surface nodes	Edge nodes	Vertices nodes
$U_j^{ABCD} - U_j^{A_1 B_1 C_1 D_1} = \widehat{U}_j^y$	$U_j^{BA} - U_j^{B_1 A_1} = \widehat{U}_j^y$	$U_j^{B} - U_j^{B_1} = \widehat{U}_j^y$
$U_j^{CC_1 D_1 D} - U_j^{AA_1 B_1 B} = U_j^x$	$U_j^{AD} - U_j^{A_1 D_1} = \widehat{U}_j^y$	$U_j^{A} - U_j^{A_1} = \widehat{U}_j^y$
$U_j^{A_1 D_1 DA} - U_j^{B_1 C_1 CB} = \widehat{U}_j^z$	$U_j^{DC} - U_j^{D_1 C_1} = \widehat{U}_j^y$	$U_j^{D} - U_j^{D_1} = \widehat{U}_j^y$
	$U_j^{CB} - U_j^{C_1 B_1} = \widehat{U}_j^y$	$U_j^{C} - U_j^{C_1} = \widehat{U}_j^y$
	$U_j^{CC_1} - U_j^{BB_1} = \widehat{U}_j^x$	$U_j^{C_1} - U_j^{B_1} = \widehat{U}_j^x$
	$U_j^{DD_1} - U_j^{AA_1} = \widehat{U}_j^x$	$U_j^{A_1} - U_j^{D_1} = \widehat{U}_j^x$
	$U_j^{D_1 C_1} - U_j^{A_1 B_1} = \widehat{U}_j^x$	$U_j^{A_1} - U_j^{B_1} = \widehat{U}_j^z$
	$U_j^{A_1 D_1} - U_j^{B_1 C_1} = \widehat{U}_j^z$	
	$U_j^{AA_1} - U_j^{BB_1} = \widehat{U}_j^z$	

where U_j^k – assigned displacement of the k-th reference point (dummy node) in the j-th direction, U_j^{ABCD} – displacement of a node on ABCD surface in the j-th direction, $\widehat{U}_j^k$ – corresponding to k-th reference point displacement of nodes in the j-th direction.

Numerical solutions for stresses and displacements can be obtained through finite element analysis by solving the boundary value problems (BVPs) of elasticity theory. In this case, there

are six different variants of boundary conditions represented by equation (21) corresponding to six

BVPs. Figure 48 illustrates this concept.
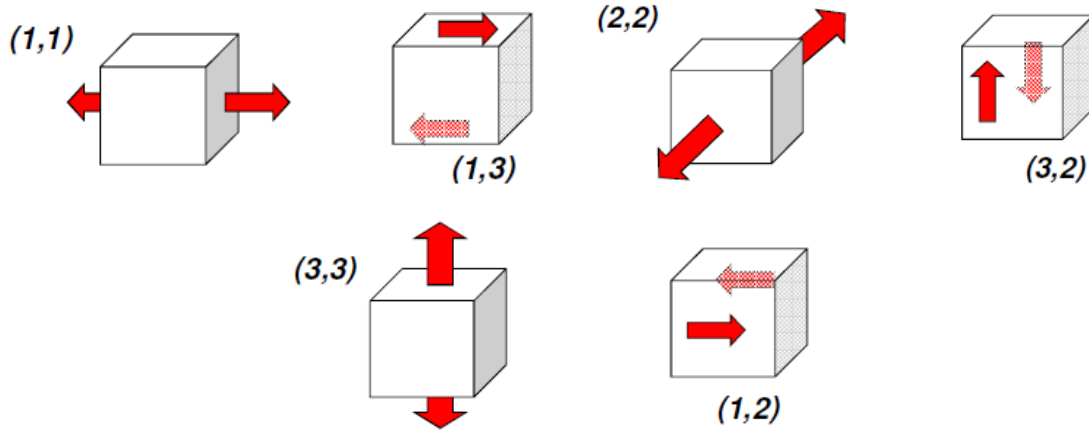
Figure 33 – Six boundary value problems that are applied to the RVE for calculating the stiffness matrix. The figure is adapted from the lectures of prof. Lomov [86].

To calculate the effective stiffness of a 3D composite with a periodic structure, it is

necessary to solve six boundary value problems of elasticity theory using periodic boundary

conditions (22). These problems correspond to six types of displacements, which are associated

with the six non-zero components of the macro-strain tensor. Table 13 provides the displacement

components of the dummy nodes for each of these six cases and the corresponding stiffness matrix

component. By solving these boundary value problems and combining the results, the

homogenised stiffness can be calculated.

Table 13 – Displacement components of the dummy nodes for six BVP.

Tensor component	Boundary condition
C_{1111}	$U_1^x = 0.2L; U_1^{y,z} = U_{2,3}^{x,y,z} = \text{unset}$
C_{2222}	$U_2^y = 0.2L; U_2^{x,z} = U_{1,3}^{x,y,z} = \text{unset}$
C_{3333}	$U_3^z = 0.2L; u_3^{x,y} = U_{1,2}^{x,y,z} = \text{unset}$
C_{1122}	$U_1^y = U_2^x = 0.1L; U_1^{x,z} = U_2^{y,z} = U_3^{x,y,z} = \text{unset}$
C_{2233}	$U_3^x = U_1^z = 0.1L, U_3^{y,z} = U_1^{x,y} = U_2^{x,y,z} = \text{unset}$
C_{1133}	$U_3^y = U_2^z = 0.1L, U_3^{x,z} = U_2^{x,y} = U_1^{x,y,z} = \text{unset}$

if $U_j^x =$ unset then $\widehat{U}_j^x = 0$ in the corresponding constrains in Table 12.

The stress fields obtained from the FE results of each of the six boundary value problems can be used to calculate all components of the stiffness matrix using the following expression:

$$\bar{C}_{ijkl} = \frac{1}{V} \sum_{elements} \sigma_{ij}^{(kl)} V_e \tag{23}$$

where V is the volume of RVE, V_e the volume of an individual element and $\sigma_{ij}^{(kl)}$ are pseudo-stress obtained as solutions to the elasticity boundary value problems.

To transform the stiffness matrix into engineering constants, nine non-linear equations with nine unknown values have to be solved. These equations express the relationship between the stiffness matrix and the engineering constants are written as follows:

$$C_{1111} = E_{11} \cdot (1 - E_{33}/E_{23} \cdot v_{23}^2) \cdot D$$

$$C_{1122} = (E_{22} \cdot v_{12} + E_{33} \cdot v_{13} \cdot v_{23})$$

$$C_{1133} = E_{33} \cdot (v_{12} \cdot v_{23} + v_{13})$$

$$C_{2222} = E_{22} \cdot (1 - E_{33}/E_{11} \cdot v_{13}^2)$$

$$C_{2233} = E_{33}/E_{11} \cdot (E_{11} \cdot v_{23} + E_{22} \cdot v_{12} \cdot v_{13})$$

$$C_{3333} = E_{33} \cdot (1 - E_{22}/E_{11} \cdot v_{12}^2) \tag{24}$$

$$C_{4444} = G_{23}$$

$$C_{5555} = G_{13}$$

$$C_{6666} = G_{12}$$

$$D = 1/\left(1 - 2 \cdot \frac{E_{33}}{E_{11}} \cdot v_{12} \cdot v_{13} \cdot v_{23} - v_{13}^2 \cdot \frac{E_{33}}{E_{11}} - v_{23}^2 \cdot \frac{E_{33}}{E_{22}} - v_{12}^2 \cdot \frac{E_{22}}{E_{11}}\right)$$

A Python library SimPy, which provides symbolic computing capabilities, was used to calculate the engineering constants from the stiffness matrix obtained from the finite element simulations.

There are several third-party implementations for PBC in Abaqus, with EasyPBC [206] being one of the most popular plugins. However, the plugin uses non-rigorous calculations of effective properties from dummy nodes, as opposed to the stiffness calculation described above, to determine the effective properties. In addition, the plugin does not provide the option of implementing additional constraints on the model. For example, it completely ignores embedded elements, which are used in this research.

Therefore, to meet all the FEA demands of this work, the PBC implementation was carried out using a Python code developed during this research. This code automatically identifies the opposing nodes and generates all the necessary constraints representing the PBCs. In addition, the code calculates the stiffness matrix and determines the effective elastic properties using the system of equations outlined above.

6.1.3   Representative volume element size determination

Accurate prediction of the effective properties of a material is critically dependent on the size of the representative volume element [47,207–209]. A balance between computational efficiency and capturing all important features is essential when selecting the optimal RVE size. Several factors such as material type, property of interest, and loading condition need to be considered when making this choice. This is particularly important for homogenisation and localisation methods. An RVE that is too small can be influenced by boundary conditions, leading to biased predictions of macroscopic behaviour. Conversely, an RVE that is too large may introduce computational inefficiencies and fail to accurately capture local variations. Therefore, choosing an appropriate RVE size is critical to achieving accurate results while avoiding unnecessary computational costs.

Different approaches exist to determine the optimal size of the RVE for mechanical simulations. Experimental or image processing methods combine material response measurements with microstructure image analysis to determine the RVE size using stress or strain indicators. Analytical approaches use models or formulas with assumptions such as random distribution, isotropy, or linearity to estimate the RVE size. However, these methods can be time-consuming or less accurate when dealing with complex structures. For this research, statistical-numerical methods are used [47]. These involve conducting numerical simulations with different RVE sizes and using statistical analysis to identify the optimal RVE size based on convergence, accuracy, or efficiency criteria.

Statistical-numerical methods involve generating random samples of the material microstructure at different sizes, applying boundary, and loading conditions, performing numerical simulations, and calculating effective properties. These methods aim to find the optimal RVE size at which the effective properties converge. This approach applies to a wide range of material types and properties, including elastic, plastic, and fracture behaviour. One such method was used in this research to find the most appropriate RVE size.

To determine the appropriate size of the RVE for our numerical experiments, we followed the guidance provided by Singh [47]. 1000C material was selected for periodicity generation and subsequent effective property prediction based on its inherently random microstructure. The RVE with the optimal is targeted to have a standard deviation less than 5% of the mean value calculated over all RVEs of that size. Specifically, we created 30 different voxel models: six RVE in five different, non-overlapping locations. The sizes of the RVEs are represented by the edge lengths: 96, 192, 288, 384, 480 and 576 μm. These values were based on the average fibre length. The sizes

of these RVEs were chosen based on the material properties (the average fibre length is 250 μm) and the expected computational resources required for the numerical simulations.

Voxel models were generated using VoxTex software, which is based on structure tensor analysis [39]. The voxel parameters, including the mesh density (i.e., the distance between voxels) and the radius of the window size, were selected to be more than 3 voxels per fibre diameter, corresponding to 4 μm for both parameters. The choice of these parameters was also based on the complexity of the material and the expected computational demands.

The voxels were segmented using a thresholding procedure based on grey scale: segmentation allowed different material properties to be assigned to different regions within the model. To ensure that the properties of each material in the RVEs were accurately captured, the threshold was determined by analysing the fibre volume fraction of the entire CT scan. The volume fraction was calculated from the fibre mass fraction used during the manufacturing of composite materials. This approach ensured that the segmentation was performed appropriately and that the material properties within the RVEs were accurately assigned. The created voxel models are shown in Figure 34.

In this instance, the models lack periodic structure, but the implementation of PBC serves to approximate the RVE size as closely as possible to the final simulation. The effective properties of the material were calculated using the periodic boundary conditions and the Python code mentioned earlier. Simulations were performed for each of the 30 models.
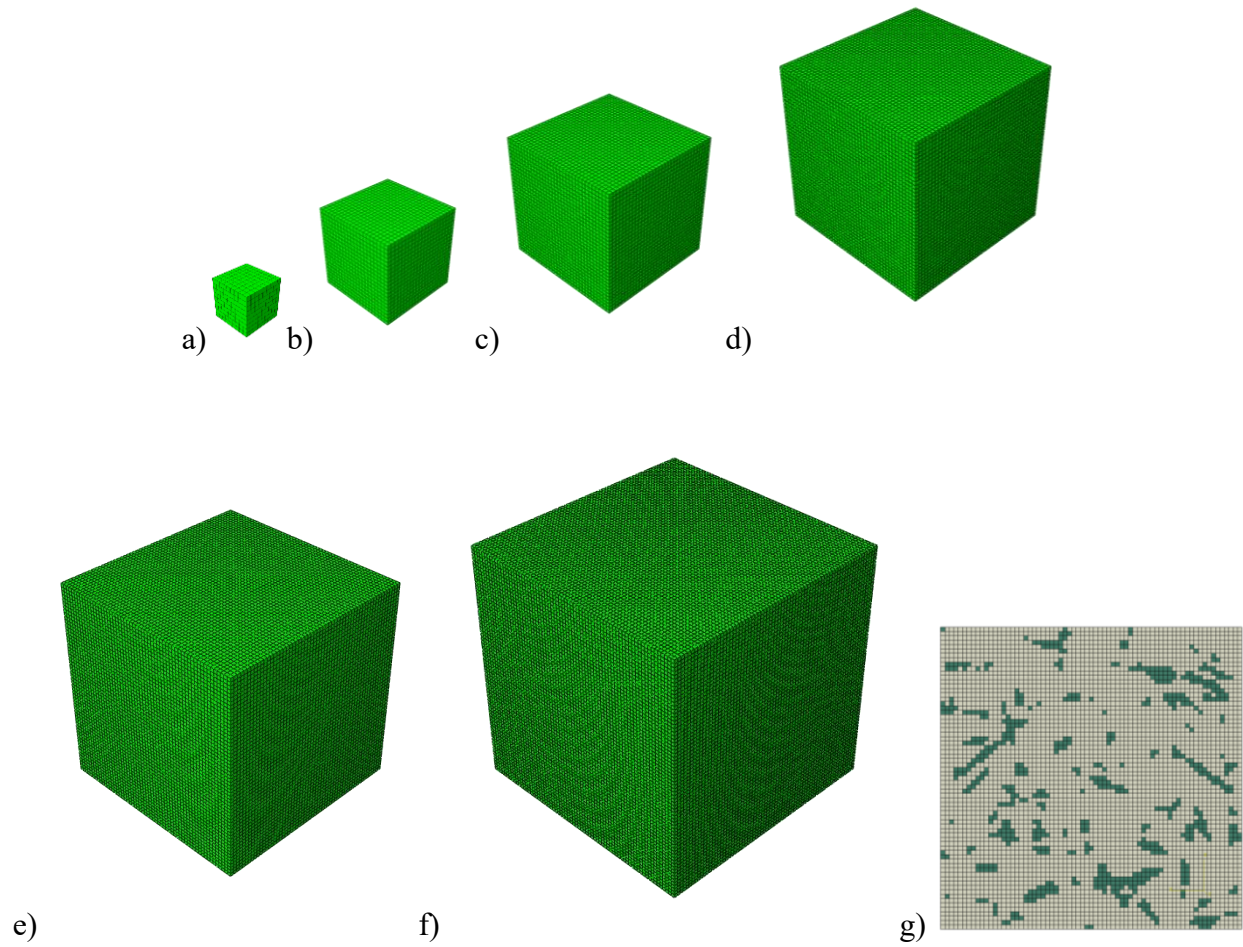
Figure 34 – Voxel models for FEA of short fibre composite to determine the RVE size represented at the same scale: a) 96, b) 192, c) 288, d) 384, e) 480 and f) 576 µm: g) thresholded slice of 576 µm RVE.

The effective properties were calculated based on the stress-strain relationships obtained from the finite element simulations of each RVE model. Table 14 presents the results of the simulations, including the tensile and shear properties for each model with their corresponding RVE size. It should be noted that all effective properties were calculated for each model, and the same trend was observed across all properties.

Table 14 – Effective tensile properties of 1000C according to 5 simulations per model size.

Model size, μm	Number of voxels	E_{11}, GPa	ν_{12}	E_{22}, GPa	G_{23}, GPa
96	729	6.5 ± 3.0	0.41 ± 0.046	4.5 ± 0.6	1.59 ± 0.4
192	9261	5.1 ± 0.6	0.41 ± 0.018	4.0 ± 0.3	1.42 ± 0.2
288	35937	5.3 ± 0.3	0.40 ± 0.004	4.2 ± 0.1	1.43 ± 0.1
384	91125	5.3 ± 0.2	0.40 ± 0.003	4.2 ± 0.1	1.42 ± 0.1
480	185193	5.4 ± 0.1	0.40 ± 0.003	4.2 ± 0.07	1.41 ± 0.1
576	328509	5.4 ± 0.1	0.40 ± 0.003	4.2 ± 0.03	1.42 ± 0.03

Analysis of the results shows that the calculated mechanical properties converge at an RVE size of 288 μm, but the standard deviation of tensile elastic modulus is a little more 5%. However, at RVE sizes of 384 μm and above, the results are highly accurate at all locations with low standard deviation below 5%. Figure 35 shows the calculated mechanical properties and their corresponding deviations, represented by the standard deviation. Figure 35 and Table 14 clearly shows the observed convergence of the calculated properties as the RVE size increases.
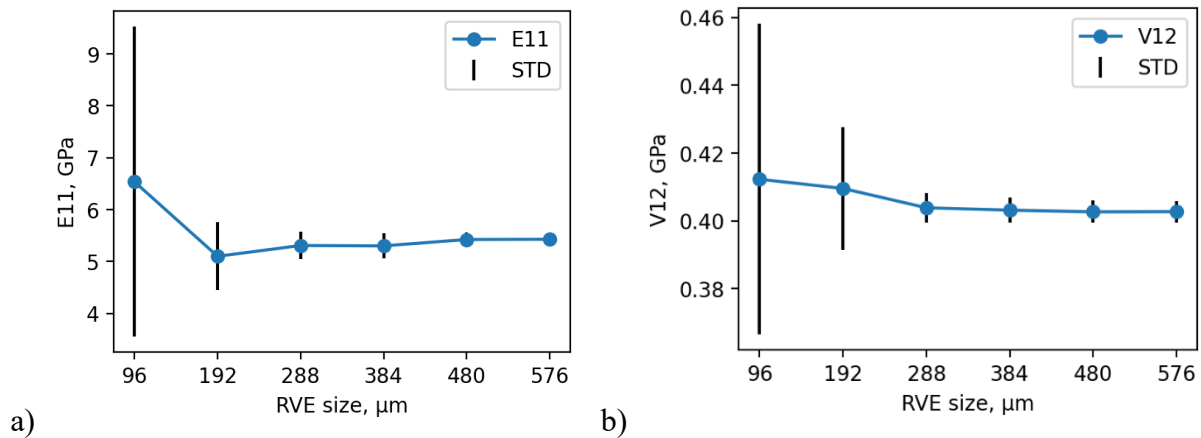
Figure 35 – Convergence of calculated mechanical properties: a) tensile modulus in X-direction, b) Poisson's ratio

The simulation results show that the effective properties of the material exhibit a degree of stability with respect to changes in RVE size. These results support previous discussions in the

literature suggesting that models with larger RVE sizes tend to produce more stable and accurate results, while smaller RVE sizes may result in less accurate and less stable predictions of effective properties. This is because smaller RVE sizes may not adequately capture all the relevant microstructural features of the material, leading to inaccuracies in the predicted effective properties.

In this study, an RVE size of 384 microns was chosen as it provides a good balance between computational efficiency and accuracy in capturing the microstructural features of the material. This size can be used for further finite element modelling from higher quality images with a finer mesh and generated periodic structure. However, it should be noted that the optimum RVE size may vary depending on the specific material and the objectives of the research. It is therefore recommended that an analysis is carried out to validate the chosen RVE size for each study.

6.1.4 Representative volume element creation

This work presents a workflow for creating representative volume elements using CT images and deep learning techniques to generate periodic structures. Additionally, the thesis introduces an approach for obtaining probability maps by image segmentation and finite element modelling, utilising both voxel and tetrahedral techniques. The entire workflow is illustrated in Figure 36.
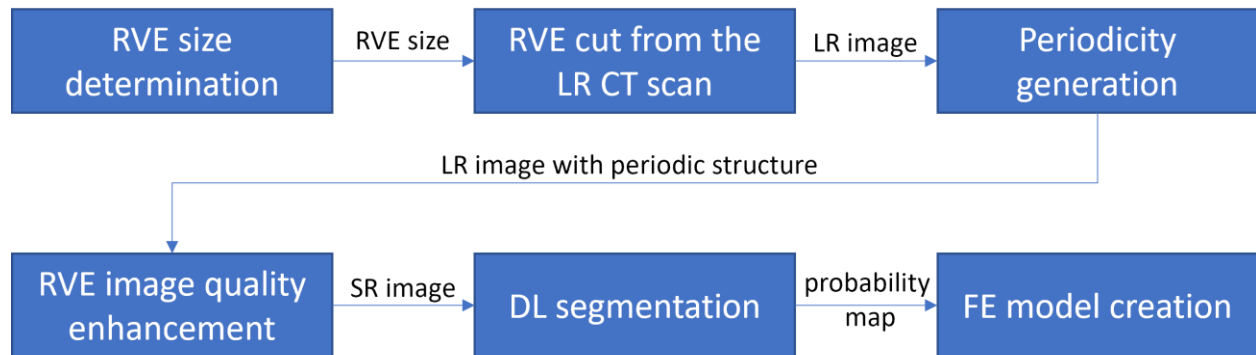
Figure 36 – Workflow for RVE creation with periodic structure from CT images

Once the appropriate size for the RVE is determined, the CT images of that physical size are processed using a periodic inpainting GAN. However, due to the high GPU memory demands of the inpainting GAN, the periodic structure generation is limited to images with lower resolution to reach the determined RVE size. Because of this, periodic generation is performed on an image with the same optimal RVE size but in low resolution. The resolution of the resulting low-resolution image with periodic structure is then increased with a super-resolution algorithm for more accurate processing. Subsequently, the SR image with periodic structure is segmented with deep learning segmentation, producing probability maps. These probability maps are then utilised to create finite element (FE) models using two widely used techniques: voxel and tetrahedral meshing. The proposed workflow enables the efficient and accurate generation of periodic microstructures with the same physical features as the original material.

6.1.4.1 Modified inpainting generative adversarial networks

This subsection explains the changes made to the inpainting GAN to generate periodic RVEs. This modified version of the model was named periodic inpainting GAN. To create this modified version, the existing inpainting GAN with 7 convolutional layers in the decoder was used as a starting point. Several modifications were made, including the development and implementation of:

- periodic convolutional layers;

- periodicity loss to ensure that the generated RVEs are periodic;

- resemblance critic and a resemblance loss to improve the quality of the generated RVE in larger periodic medium.

The architecture of the periodic inpainting GAN is presented in Figure 37.
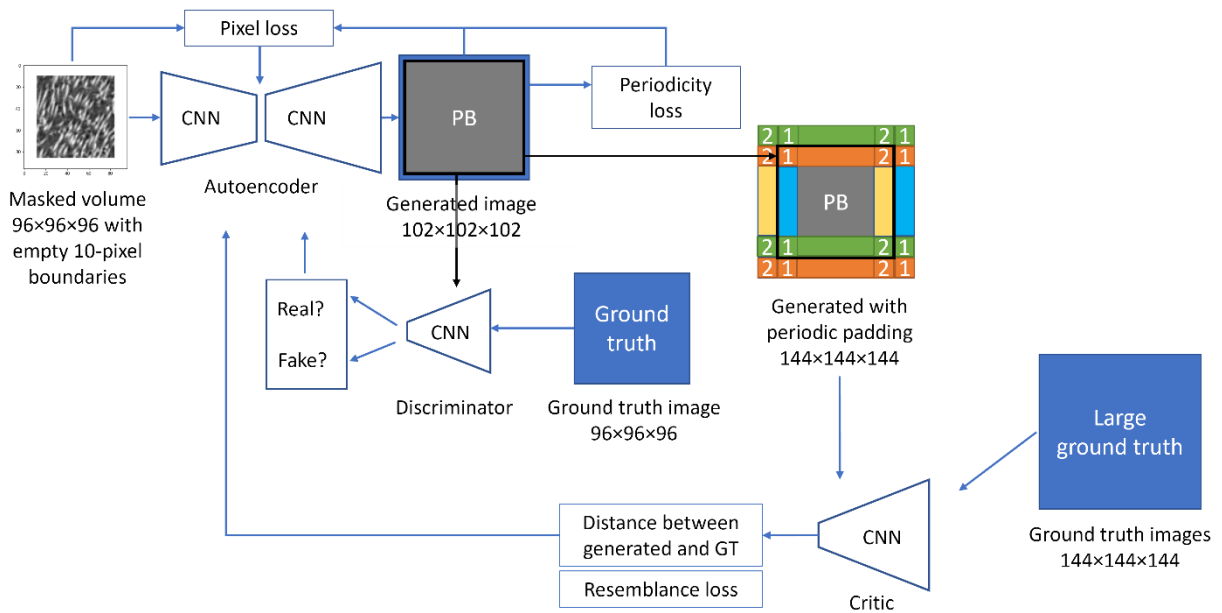
Figure 37 – The modified architecture of periodic inpainting GAN

A periodic convolutional layer is similar to a standard convolutional layer, but it takes input data from the previous layer and applies additional periodic padding. This padding involves copying data from one edge of the image and concatenating it to the opposite part of the image. This is illustrated in Figure 38 for the 2D case. In this work, we apply the same procedure to 3D CT images. The thickness of the padding is equal to half of the current kernel size and rounded down to the nearest integer: for example, for kernel size of 3×3×3 the thickness of the padding would be one, for 5×5×5 it would be 3. In this work, the periodic convolution uses the "same" boundary treatment.

In deep learning terminology, there are two ways to process boundaries in convolution: using "same" and "valid" boundary treatments. If the "same" treatment is used with periodic padding, the output size of the convolutional operation will be larger than the original size by twice the periodic thickness. On the other hand, if the "valid" treatment is used with periodic padding, the output size will be the same as the input size. It is important because by using different

boundary treatments during convolution, we can only control the size of the output, but also implement an additional loss on the boundary, which will be discussed below. The "same" boundary treatment is used for periodic convolution in this work.
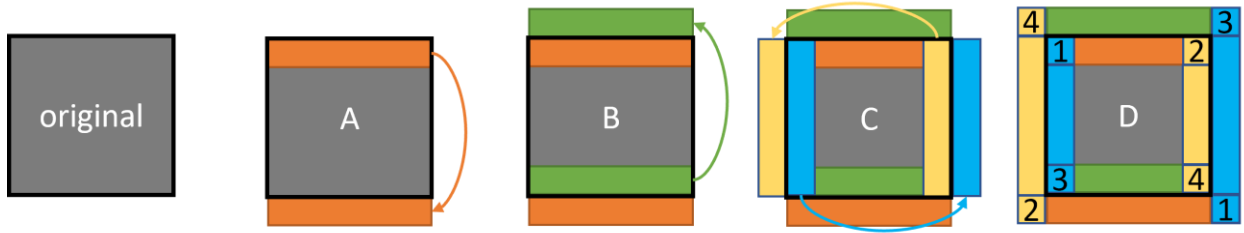
Figure 38 – Illustration of periodic padding in 2D with the black square indicating the initial boundaries of input. A, B, and C show edge concatenation and D shows vertices concatenation.

The purposes of the generator (autoencoder) and the discriminator were not altered. In the modified generator architecture, each deconvolutional layer is followed by a periodic convolutional layer to produce a periodic structure in the output. The complete architecture of the modified generator is shown in Table 15. For the discriminator, it remains the same as in the original inpainting GAN in Section 5.1.3, but in the modified case it takes data from the centre of the generator output, which corresponds to the desired size of the RVE.

A new CNN has been added to the architecture, which is similar to the discriminator but does not discriminate between fake and true volumes, but "criticises" the overall structure resemblance between the two volumes. The input to this network is obtained by taking the data from the centre of the generator output that corresponds to the desired RVE size and applying large periodic padding (with a thickness of 24 pixels) to mimic the final structure with periodicity. Unlike the discriminator, the resemblance critic does not use a sigmoid activation function to limit the values to 0 or 1, which correspond to fake and true data, respectively. Instead, it uses the relative average GAN loss (as shown in equation (12)). By using this approach, the CNN outputs the distance between the real and generated data, which the new CNN is set to maximise, while

the generator is set to minimise this distance. These types of networks, which cannot accurately distinguish real and fake data but only calculate the distance between them, are called critics [190].

Table 15 – Architecture of the modified generator.

№	Layer	Input	Stride	Activation	Output
1.	Conv3D	96×96×96×1	2×2×2	LeakyReLU+BN	48×48×48×64
2.	Conv3D	48×48×48×64	2×2×2	LeakyReLU+BN	24×24×24×128
3.	Dil.conv3D	24×24×24×128	1×1×1	LeakyReLU+BN	24×24×24×128
4.	Conv3D	24×24×24×128	2×2×2	LeakyReLU+BN	12×12×12×256
5.	Dil.conv3D	12×12×12×256	1×1×1	LeakyReLU+BN	12×12×12×256
6.	Conv3D	12×12×12×256	2×2×2	LeakyReLU+BN	6×6×6×512
7.	Conv3D	6×6×6×512	1×1×1	LeakyReLU+BN	6×6×6×512
8.	Conv3D	6×6×6×512	1×1×1	LeakyReLU+BN	6×6×6×512
9.	Deconv3D	6×6×6×512	1×1×1	ReLU+BN	6×6×6×512
10.	Deconv3D	6×6×6×512	1×1×1	ReLU+BN	6×6×6×512
11.	Deconv3D	6×6×6×512	2×2×2	ReLU+BN	12×12×12×256
12.	Dil.deconv3D	12×12×12×256	1×1×1	ReLU+BN	12×12×12×256
13.	Valid.periodic	12×12×12×256	1×1×1	ReLU+BN	12×12×12×256
14.	Deconv3D	12×12×12×256	2×2×2	ReLU+BN	24×24×24×128
15.	Dil.deconv3D	24×24×24×128	1×1×1	ReLU+BN	24×24×24×128
16.	Valid.periodic	24×24×24×128	1×1×1	ReLU+BN	24×24×24×128
17.	Deconv3D	24×24×24×128	2×2×2	ReLU+BN	48×48×48×64
18.	Same.periodic	48×48×48×64	1×1×1	ReLU+BN	50×50×50×64
19.	Deconv3D	50×50×50×64	2×2×2	ReLU+BN	100×100×100×64
20.	Same.periodic	100×100×100×64	1×1×1	tanh	102×102×102×1

The periodicity loss is an important addition that efficiently uses the extra data generated due to the implementation of periodic padding with the same treatment of boundaries. This loss is computed as the mean absolute error between the generated data outside the desired RVE size and

the corresponding data from the opposite edge but within the RVE size. To help visualise this, consider Figure 38 where the RVE is enclosed by the black rectangle and the data outside the rectangle is generated during the periodic padding. In this case, the loss is calculated as the difference between the identically coloured parts inside and outside the rectangle. It is important to note that all calculations are done in 3D to account for the CT image data. The periodicity loss provides a means to hardcode a check for the periodicity of the generated volumes, and it is combined with the pixel loss. The generator is then trained to minimise this combined loss, resulting in a more accurate and periodic representation of the RVE.

Furthermore, the pixel loss on the boundaries is calculated using a spatially discounted reconstruction loss that takes into account the gradient. This pixel loss is calculated in a similar way to a previously proposed method [140] and is based on assigning weights to each pixel in the mask based on its distance l from the closest known pixel. This distance-based weighting is calculated as γ^l, where γ is a constant value of 0.9 that is consistent throughout the process.

The training and image generation procedure for the modified generator is the same as for the original inpainting GAN. The size of the input volume is 96×96×96 pixels with empty 10-pixel boundaries, meaning that the useful CT data is 76×76×76 pixels. At each iteration, a new input volume is generated with corresponding ground truth images that are not periodic. The training process involves minimising the weighed loss of the generator, the discriminator, and the critic, which includes the pixel loss, periodicity loss, and two relative average GAN losses.

The periodic inpainting GAN was tested on CT scans of two different short-fibre composites. The physical properties, such as fiber volume fraction and orientation distribution, closely match those in the original image, as demonstrated in Chapter 4. Figure 39 shows the generated periodic structures, where the purple rectangle indicates the generated RVE, and the

green rectangle indicates the initial CT image size given to the periodic inpainting GAN. The image outside the purple rectangle is shown to better illustrate the periodicity. This data is not new, and it has been copied in periodicity manner from the generated RVE.
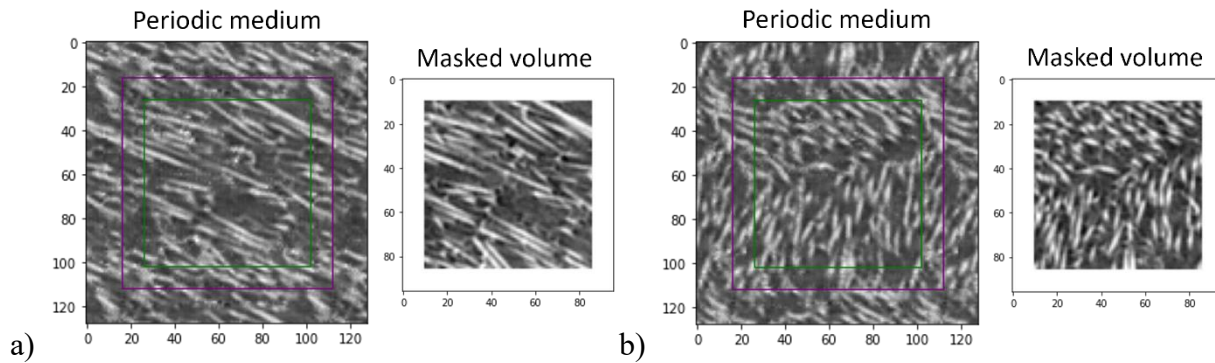
Figure 39 – Middle slices of generated volumes: a) an example of long fibre generation to ensure structure periodicity, b) an example of generation of two different orientations that merge at the boundary

The generated periodic structures shown in Figure 39 demonstrate that the algorithm was able to successfully generate microstructures with over 90% periodicity (pixel correlation of opposite faces), a substantial improvement compared to the original images which had approximately 50% periodicity. For instance, in Figure 39a, the fibre from the top right corner correctly continued into the masked region and had identical continuations on the right and left boundaries, demonstrating the periodicity. The second image from the same material shows how the model was able to recognise the change in fibre orientation and reconstruct the RVE in a way that smoothly transitions between boundaries. The periodic RVE generation of the short fibre composite with the lower fibre volume fraction also exhibits a periodic structure.

6.1.4.2 Super-resolution of the generated images.

Super-resolution is used to enhance the quality of generated images so that they have the same resolution as the original high-resolution images. In this case, super-resolution is being used because inpainting was performed on low-resolution images due to the high requirements of deep

learning on GPU memory. This step is optional and is being included here to provide a complete overview of the possible pipeline for creating high-quality RVEs.

The super-resolution model trained during the research, described in Chapter 5, was not effective at working with generated structures. This is because it was trained to increase the resolution of the original lo LR using data from HR images, not generated images. The model's ability to capture image features that are not observable to the human eye can explain this behaviour, and it results in a significant difference between the generated images and the original ones.

To address this problem, we retrained the super-resolution (SR) model with the same architecture using fully regenerated images obtained through inpainting. This was done by cutting the full CT image into small volumes of size 76×76×76 pixels, with an 8-pixel overlap, similar to the approach used for super-resolution image reconstruction. Next, we cut the LR images into 294 images and regenerated each one using the inpainting algorithm. Finally, we stitched all these images together to create a new fully regenerated CT volume. The entire process took less than 15 minutes of computation time. Figure 40 displays both the original and fully regenerated images. As can be seen in the images, the style of fibre representation in the regenerated images is quite different, and there are grey scale variations that can be related to kernel size.

The original HR volume and fully regenerated LR volume that contained the generation features through inpainting were used as input for the super-resolution training. The training process followed the same procedure outlined in Section 5.2, and no additional adjustments or parameter changes were made. The training took approximately 24 hours.
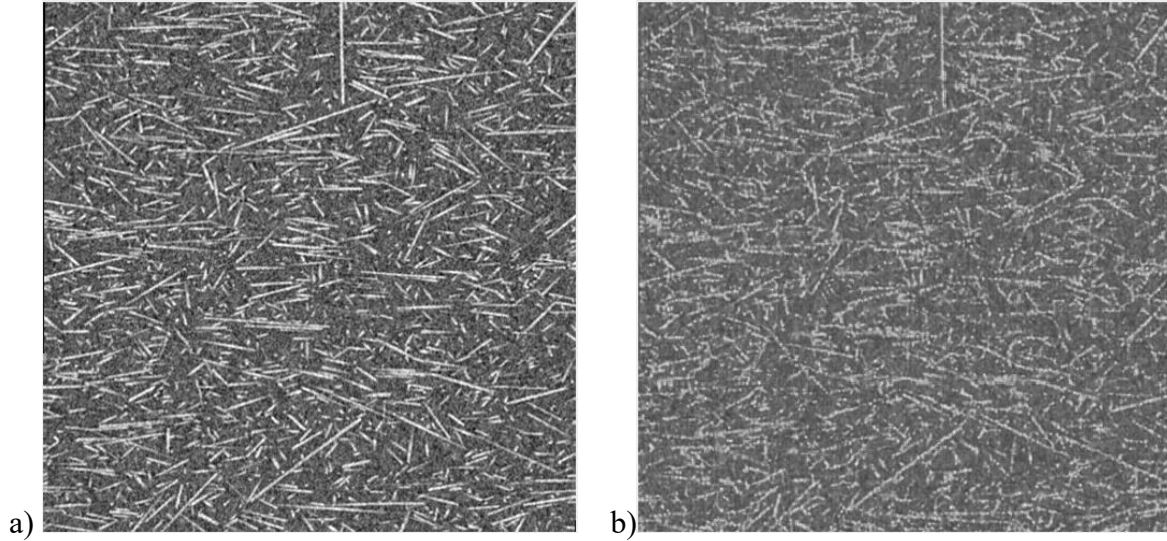
Figure 40 – Middle slices of full CT volumes of a) original LR image; b) inpainting regenerated image

The super-resolution algorithm, trained on generated images, is now capable of enhancing the quality of the generated RVEs. Figure 41 displays slices of the high-quality RVEs that were created, which do contain some artefacts due to the complex transition from the LR-generated image to the HR images. However, these artefacts did not pose a problem, as deep learning segmentation can identify them and identify objects accordingly at this resolution.
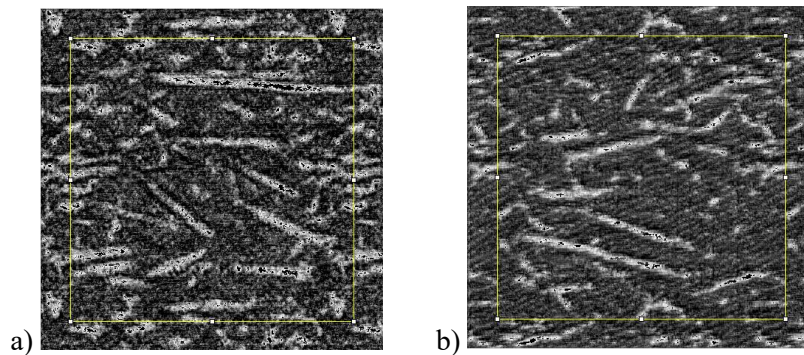
Figure 41 – SR enhanced periodic medium with the RVE in the yellow rectangle: a) middle slice, the information of the centre was known, b) bottom slice, which was fully generated without preliminary information of the region.

6.1.4.3 Segmentation of the generated images.

To identify fibres, we used RootPainter software which utilises a deep-learning segmentation algorithm. We followed the process described in Section 5.3, which involved the first manual annotation of fibres, followed by model training and corrective annotation during the training process. The procedure was performed for both HR original RVE and periodic RVE.

The microstructure of short fibre composites is complex, and identifying the correct boundaries of the fibres from CT images is not always straightforward. This can result in operator errors during the annotation process, leading to deep learning algorithms learning contradicting features. To address this issue, we performed image segmentation twice in both the XY and XZ planes and then averaged the results to imitate a quasi-three-dimensional segmentation. This approach indirectly calculated the segmentation results using information from neighbouring slices. We used probability maps, obtained from the raw output of the deep learning segmentation, to indicate the likelihood of each pixel belonging to the fibre class. In these maps, black pixels correspond to the matrix, while white pixels correspond to fibres.

We applied this approach to segment the RVE volume slice by slice, with each direction of segmentation taking less than 30 minutes for annotation and training, and less than 5 minutes for segmentation. To obtain the final probability volume, we smoothed the probabilities in 3D using results from both the XY and XZ directions and then averaged them. This method helped to reduce operator errors and improve the accuracy of fibre identification. The results of the segmentation in the YZ direction are presented in Figure 42.
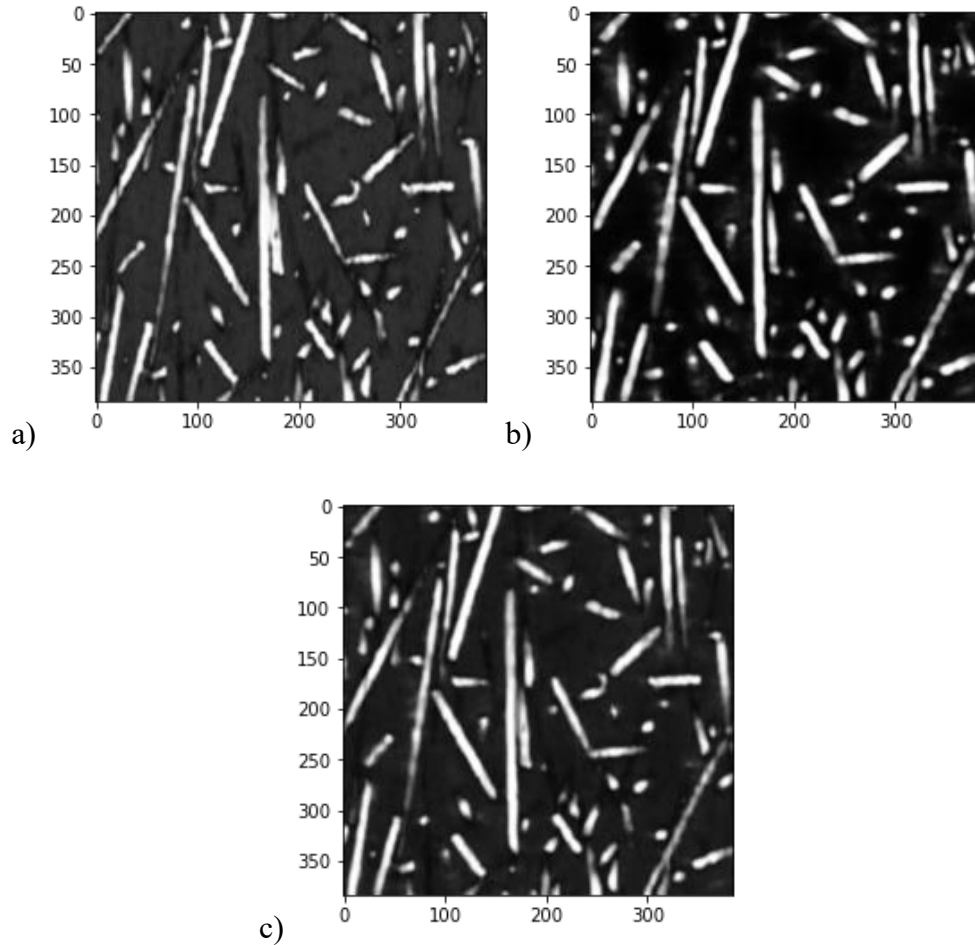
Figure 42 – Probability maps of a YZ image of original RVE obtained with annotation: a) in the XY direction; b) in the XZ direction; c) by averaging in XY and XZ directions

The vertical defects observed in the XY segmentation, which are attributed to operator errors that arise from using 2D segmentation methods. The final image, obtained by averaging and smoothing the probability maps, may not have edges that are as sharp as segmentation in one direction, but it mitigates artefacts resulting from operator annotation. These images can be utilised as a substitute for CT images in any software for further analysis. This approach can improve the accuracy of segmentation in other software where only classical algorithms such as thresholding are provided.

6.1.4.4 FE models of RVE

To analyse the behaviour of the material, two models were created based on a 3D image of the generated RVE: a voxel model and a tetrahedral model.

The voxel model was created using VoxTex software based on the probability volume obtained after deep-learning object identification. To ensure the accuracy of the model, the parameters for the voxel model were chosen to have at least four voxels per fibre diameter. This was achieved by setting the distance between voxels to 4 pixels and the radius of the integration window to 4, which captured only half of the neighbouring voxel integration window. The voxels were segmented by density thresholding, with a threshold value selected to match the experimentally obtained fibre volume fraction. The materials were assigned to the glass and matrix based on the material properties listed in Table 1, and the orientations of the materials were not specified since both the fibre and matrix are isotropic materials. The resulting image of the voxel FE model is shown in Figure 43.

Figure 43 – Voxel model created with VoxTex software with green as fibre and white as matrix

The model accurately captures the important microstructural features of the material. However, due to the voxel nature of the model, fused objects can be observed. To separate the fibres from each other and obtain a more accurate representation of the microstructure, the mesh would need to be much finer. This would require a smaller voxel size and result in significantly larger models, making them impractical to calculate.

In addition to the voxel model, a tetrahedral-mesh model (hereafter referred to as tetrahedral model) of the fibres was created using Avizo software. The main advantage of using a tetrahedral mesh is the ability to create models of complex microstructures that more accurately capture the shape and features of even the most complicated geometries. To create the tetrahedral model in Avizo software, probability volumes were segmented to match the experimentally obtained fibre volume fraction. The geometry was then smoothed in 3D to eliminate sharp edges, which is necessary to avoid poorly shaped elements that cannot be accurately meshed.

The tetrahedral mesh was generated using standard Avizo software with medium quality to have a balance between accurately capturing small features and minimising computation time and mesh complexity. Despite using mesh optimisation, initially, the mesh contained around 1% of "badly" shaped elements known as slivers, which have almost flat features. To repair these bad-quality elements, built-in optimisation tools in Avizo were used. The optimisation process targeted elements with a ratio of the radii of the inscribed sphere and the circumscribed sphere less than 0.02. The mesh modifiers used included "automatic" and "repair bad tetras". As a result, the number of bad tetrahedral elements decreased from 5841 to only 16. The final tetrahedral model of the fibres is shown in Figure 44.

Figure 44 – FE model of fibres created using Avizo software

To create a complete FE model, the previously created fibre geometry was imported into Abaqus software and embedded within the matrix geometry with a mesh size of 8 µm (approximately 2 elements per fibre diameter). Embedded element constraints were employed in this process, which kinematically constrained the fibre elements with host elements of the matrix. According to the Abaqus documentation [210], the translational degrees of freedom of the nodes of the embedded elements are constrained by the interpolated values of the corresponding degrees of freedom of the host elements. The adoption of this method simplifies the implementation of PBC as it ensures a uniform mesh at the boundaries. However, this approach leads to an overestimation of the stiffness of the embedded locations since this volume contributes to the stiffness twice, as both matrix and glass [211]. To ensure accurate calculation of the stiffness matrix, the Young's modulus of the glass fibre was reduced by the Young's modulus of the matrix, resulting in 68.5 GPa.

Overall, from a single location of the CT scan, four high-quality RVE finite element models were created. These models included original and periodic versions using both voxel and tetrahedral implementations.

6.1.5 Results and discussions of simulation with PBC

The simulations of the periodic and original RVEs were performed using Abaqus software and a Python code developed according to the procedure described in Section 6.1.2 about periodic boundary conditions. PBCs were applied to both RVEs to ensure an accurate representation of the larger material. The simulations were run for six loading cases, as shown in Figure 33. The time required for calculations was approximately 20 hours for the voxel models and 8 hours for the tetrahedral models. The simulation results are presented in Figure 45. In this research, the elastic modulus in prevalent orientation was calculated (E_{11}). Since the material exhibits almost transversely isotropic behaviour, elastic properties in other directions are represented as perpendicular to the prevalent orientation ($E_{22} \approx E_{33}$).

The stiffness tensor was calculated based on the six loading cases described earlier, and the effective elastic properties were then recalculated from the stiffness tensor using equation (24). The resulting values are presented in Table 16.

Table 16 – Predicted effective elastic properties of short fibre composite 1000C with different RVEs with the error in brackets if compared with the experimental value.

Model	Number of elements	E_{11}, GPa (error, %)	ν_{12} (error, %)	E_{22}, GPa	G_{23}, GPa (error, %)
Original voxel	804357	5.59 (7.1)	0.38 (5)	4.23	1.44 (5.2)
Periodic voxel	804357	5.43 (9.8)	0.38 (5)	4.35	1.42 (6.6)
Original tetra	641615	5.75 (4.5)	0.38 (5)	4.14	1.39 (8.6)
Periodic tetra	542596	5.64 (6.3)	0.38 (5)	4.24	1.37 (9.5)
Experiment	-	6.02	0.40	-	1.52
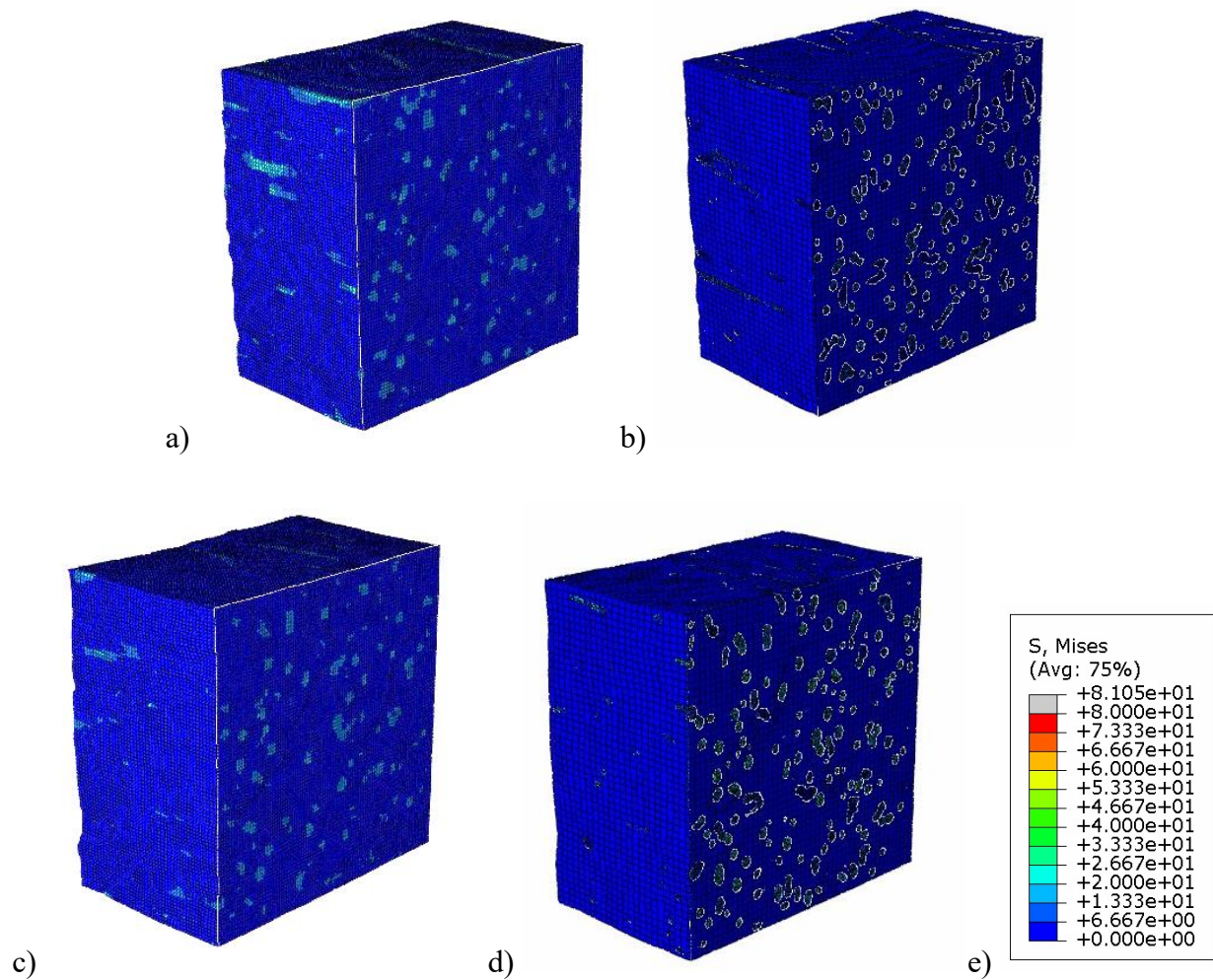
Figure 45 – Distribution of von Mises stresses for tensile loading along the x-direction with a transparent cut in the middle of the RVE: a) original voxel; b) original tetrahedral; c) periodic voxel; d) periodic tetrahedral; e) legend in GPa.

When comparing the predicted effective elastic properties with the experimentally determined properties of the tensile specimen from which the CT specimen was cut, a reasonable agreement is observed. The error was within 10% of the individual specimen's elastic modulus and within 15% for the mean value of specimens from different plates, so the fibre orientation is not

known in the experiment. However, it is important to note that the developed models tended to underpredict the material stiffness. This could be because the material's microstructure is random, and the fibre fraction distribution may differ for each tensile specimen. To obtain more accurate predictions, additional CT scans should be conducted on different plates to account for the inherent variability of the material's microstructure. However, for this study, only one CT scan was analysed. Despite the limitations of the analysis, the results provide valuable insights into numerical simulation with PBCs of deep learning-generated structures.

The results suggest that the periodic RVE model exhibits a larger discrepancy from the experimental value compared to the original RVE model. This observation may be attributed to the relatively large size of the RVE used in the study, which could have minimized the effect of stress/strain fluctuations at the edges. It is plausible that the differences between the two models would favour the periodic RVE model if a smaller RVE size was employed. Furthermore, it is possible that the input parameters used for the fibre-matrix system were not precise, and an increase in matrix stiffness, for instance, could lead to higher model predictions than the predicted tensile stiffness. As an example, the matrix properties may have been undervalued. Under such circumstances, the simulation results could potentially be higher for both the original and periodic models, with both possibly exceeding the experimental values. Therefore, in this case, the periodic simulation would yield results that are closer to the experimental data.

The most important results of the analysis can be seen when examining the local stress fields, particularly on the boundaries of opposite faces, as shown in Figure 46. Inconsistencies are observed between opposite faces of the model. Specifically, a significant difference is noticed between faces a) and b), which is not characteristic of a model with implemented PBC where a

smoother transition is expected. In contrast, images c) and d) show much smaller differences, resulting in a more uniform transition from one face to another.
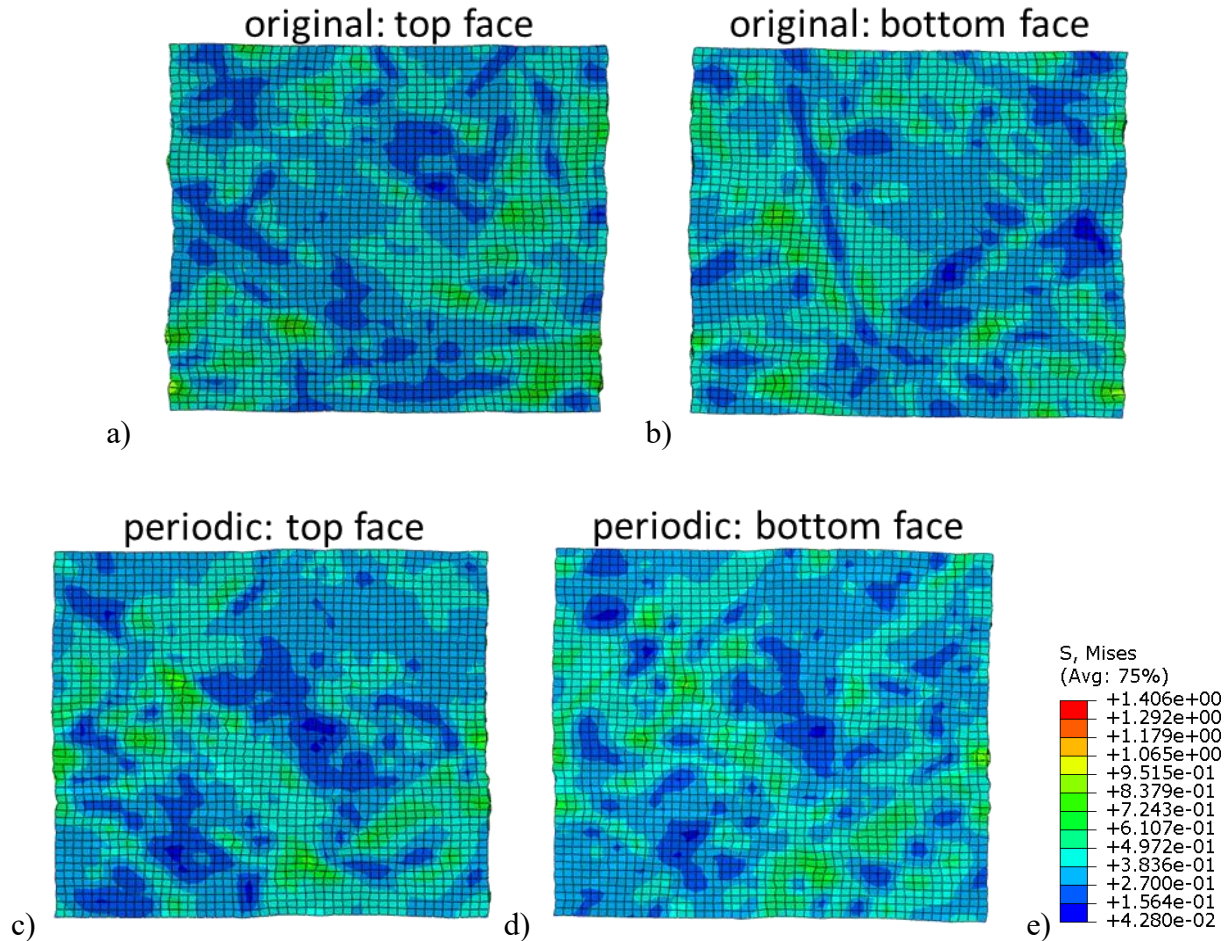
Figure 46 – Significant stress differences in the matrix on the opposite XZ faces of (a,b) tetrahedral original RVE and a minor difference on (c,d) periodic RVE. The legend (e) in GPA is the same for each figure.

The stress distributions on the periodic RVE are nearly identical, indicating that there are no property jumps on the boundaries when the periodic structure is imitated. In contrast, the stress distribution on the original RVE is completely different, there are non-physical stress and strain fluctuations between the boundaries. They can cause discontinuities in the stress and strain fields and affect the overall behaviour of the material for more comprehensive simulations. These results suggest that additional treatment of the original RVE is necessary to achieve a more accurate

simulation. Also, the higher error in effective properties of the voxel model can be linked to these stress fluctuations. The lower predicted effective properties in the voxel model can be attributed to the presence of more elements, which can result in stress concentrations not propagating as far as in the smoother model.

In addition to examining the local stress fields, the matrix material was inspected to predict its yield behaviour using the von Mises yield criterion. Von Mises stresses were calculated at an elongation of 3%, taking into account the specimen's tensile failure strain of 3.5%. The von Mises stress values of all elements of the matrix were then imported and statistically analysed, resulting in the histogram represented in Figure 47. The Poketon M330 material has a tensile yield strength of 60 MPa. This means that yielding begins when the von Mises stress value of a finite element reaches this value, the elastic energy of distortion reaches a critical value and plasticity begins after this point. The red line on the histogram indicates when the elements surpass the critical value.
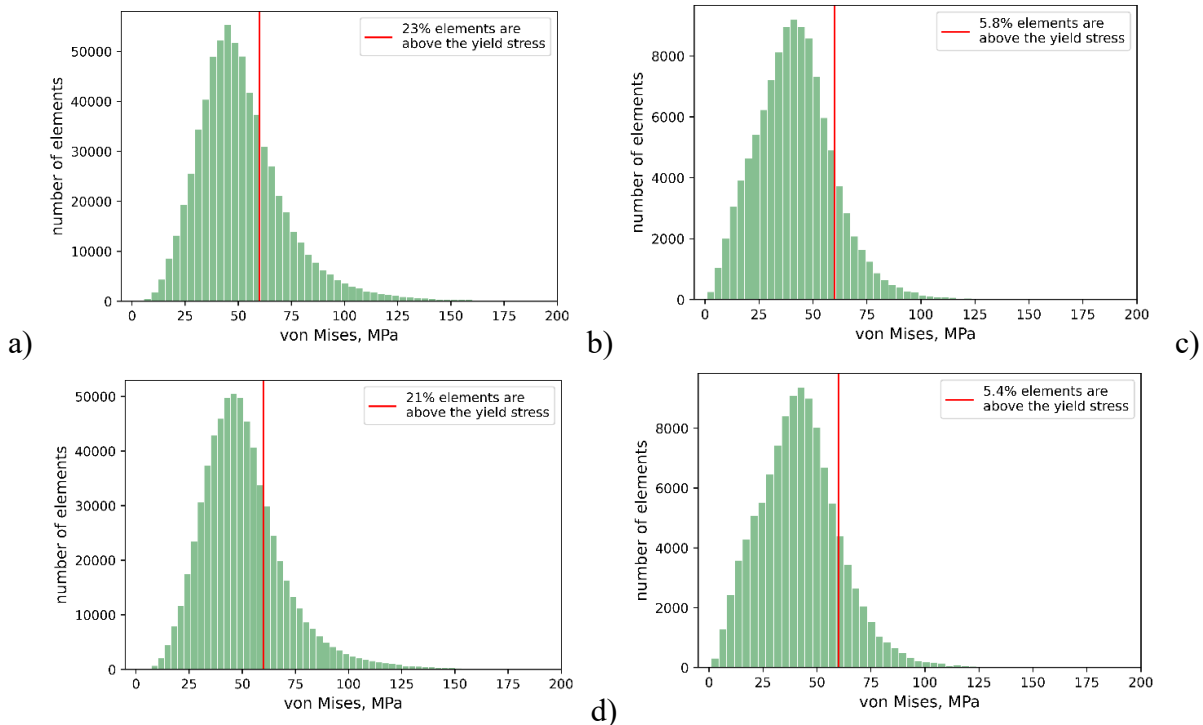
Figure 47 – Histograms of the number of matrix elements only and their calculated von Mises stress values for 3% elongation: a) original voxel; b) original tetrahedral; c) periodic voxel; d) periodic tetrahedral. The red line indicated the matrix yield stress.

There is no significant difference between original and periodic RVEs if the number of affected elements is considered. However, the analysis indicates that the voxel model produces a much higher number of matrix elements above the critical value due to the artificial concentration on material-to-material boundaries. On the other hand, the tetrahedral model is more suitable for damage analysis, as it does not produce any artificial stress concentration. This outcome can be attributed to the structural characteristics of the voxel models, which feature a ladder-like structure with sharp edges and lack the smooth curves found in tetrahedral models. The sharp edges in voxel models can lead to stress concentrations in more elements. Nonetheless, generating a tetrahedral mesh is considerably more challenging due to the possibility of producing low-quality elements. Additionally, the voxel models always converge, despite their long calculation time, while the tetrahedral models are less likely to converge easily, and additional effort should be made to ensure stable calculations.

6.1.6 Conclusion

The modified inpainting GAN was developed for generating fully periodic representative volume elements. To achieve this, the network was modified to include periodic layers, periodicity loss, and a resemblance critic. The proposed network was able to generate periodic RVEs, and the image quality was further improved using a super-resolution algorithm to match the resolution of the original RVEs. To segment the fibres in both the original and periodic RVEs, deep learning algorithms in the RootPainter software were used, resulting in the generation of probability volumes. These probability volumes were then used to create voxel and tetrahedral models using VoxTex and Avizo software, respectively.

The simulations were carried out using a python code with periodic boundary conditions for both the original and periodic representative volume elements (RVEs). The results of the simulations showed that both RVEs had similar solutions that were in average agreement with the measured tensile properties. However, the periodic RVE showed significantly better boundary treatment without any property jumps between opposite faces, while the original RVE had a significant jump and boundary stress fluctuations, indicating non-physical simulation results, which should be treated separately. In addition, the von Mises stress values of the matrix elements were compared with the yield stress of the matrix material for 3% elongation. The analysis revealed that the tetrahedral models produced fewer elements with von Mises stresses above the critical value of 5-6%, compared to more than 20% for the voxel models, indicating more physical behaviour. This suggests that tetrahedral models are more accurate for local field representation, but they are also more challenging to handle.

6.2 Automation of synchrotron-based fibre break identification

The second implementation of the developed algorithms is devoted to the use of super-resolution to enable automated fibre break identification from low-resolution synchrotron CT scans of unidirectional composites. The section is based on the submitted paper by Karamov et al. [212].

6.2.1   Introduction

The methodology is verified on unidirectional composites which are commonly used in industry due to their high mechanical properties-to-weight ratio. One common form of damage in UD composites is fibre breakage, which causes longitudinal tensile failure. Accurately predicting this phenomenon is difficult and requires comprehensive mathematical models and reliable verification methods. Previous studies have introduced different prediction models [213–217], but

recent benchmarking exercises have shown that these models are not accurate in predicting fibre break development [42,43,111]. In-situ experimental methods are crucial for improving the accuracy of longitudinal tensile strength predictions [43].

Identifying fibre breaks in low-resolution images requires manual effort and multiple attempts to locate all breaks, which can be time-consuming. In-situ scans produce numerous volumes, and with fibre break densities reaching up to 1000 mm^3, it may take several working days to identify all the breaks in one volume manually [43]. X-ray CT's resolution limitation is one of the bottlenecks impeding the development of models for properties that rely on composite material damage and microstructure information, including longitudinal tensile failure.

In this part of the research, it is proposed to use the developed combination of 3D modifications of ESRGAN and CycleGAN to improve the quality of synchrotron CT images of UD composites for automated fibre break analysis. The study was conducted on two types of carbon fibre/epoxy unidirectional composites with known fibre break distribution, T700SC with both LR and HR images and 34-700 [218] with LR images only. The first material was used for training, the second for validation. The quality of super-resolution enhancement was evaluated using two metrics: the number of individual fibre breaks (1-plets) and the number of clusters (2-plets, 3-plets). Implementing deep learning techniques significantly improves identification quality and reduces the need for manual intervention and time requirements.

6.2.2 Super-resolution enhancement

The super-resolution architecture is described in Section 5.2. There were no additional interventions to the work of the already trained model, and it was taken from that study as is. However, the 34-700 LR scan was image processed to match the original T700SC LR scans in

terms of average grayscale values, contrast, and sharpness. The CT images of the composite are provided in Figure 15.

To handle the hardware-intensive tasks of deep learning and CT processing, we divided the CT volumes into smaller volumes: $32 \times 32 \times 32$ pixel^3 for low-resolution images and $128 \times 128 \times 128$ pixel^3 for high- and super-resolution images. For low-resolution images, we used a volume overlap of 3 pixels, and for high-resolution images, we used an overlap of 12 pixels. The total training dataset comprised 4560 LR and HR small volumes of T700SC. In contrast, the image of the 34-700 material was divided into 61489 small volumes of the same size. The final resolution of the SR image of the 34-700 material was $4336 \times 1912 \times 6864$ pixel^3, and the 16-bit version had a size of more than 100 GB.

6.2.3 Automated algorithms of fibre identification

To obtain reference data for fibre break locations, several manual inspections of images were performed for fibre break analysis in detail on the last volume before failure in the previous works [6,35]. For the specimen with 17 volumes to be analysed manually, it took about 5 working days to identify all the fibre breaks once everything is set up. This is due to the high fibre break density, which can reach 1000 breaks/mm^3 and the low resolution of the images posing difficulties in unambiguously identifying all the breaks.

In this study, all dark regions, including possible fibre breaks and cracks, are referred to as voids. To identify fibres and voids in the images, RootPainter software was employed, which utilises deep learning techniques and implements a U-Net network for image segmentation. The algorithm was trained interactively on partially annotated images, and the batch size was set to 4 with 3x3 kernels. To locate the centre points of fibres, only the central portions of the fibres without edges were used for training. Additionally, part of the InSegt Fibre code [22] was implemented for

fibre segmentation and trajectory tracking. For 3D analysis of voids, the MATLAB "regionprops3" function was used, and the voids were filtered to remove noise (voids less than 1000 pixels in volume) and very large objects (more than 10^5 pixels in volume), which were analysed manually.

Two techniques were employed to differentiate between fibre breaks and voids. The first method identifies fibre sections above and below a void along the smallest diameter of an ellipsoid fitted to the void. Voids located between these fibre sections are then classified as fibre breaks. The second method utilises a high-resolution CT image of the initial state of the specimen, which is registered with the loaded state images using a MATLAB image registration algorithm. Voids that intersect the initial fibre trajectories are selected as fibre breaks. The second approach is adopted from the algorithm that was used in [43] for higher-quality CT scans of stepwise loaded specimens. To avoid false identification resulting from image artefacts, the intersection of the voids and fibre sections is based on the distance from the void centre to the fibre centre.

The analysis of fibre break clustering was based on geometric criteria that relied on stress redistribution caused by the break, similar to [43]. Specifically, two fibre breaks were considered as part of the same cluster if their centre points were located within a cylindrical volume of 13 μm radius (equivalent to 2 fibre diameters) and an axial length of 97.5 μm (equivalent to 15 fibre diameters).

To analyse the accuracy of fibre break identification, statistical classification [219] was used in this study. The identification was classified as true positive if it correctly indicated the presence of a fibre break, false negative if it incorrectly indicated the absence of a fibre break, and false positive if it incorrectly indicated the presence of a fibre break. The accuracy of the automated algorithm was determined based on its proximity to the number of fibre breaks identified manually. The accuracy was calculated using the following equation:

$$Accuracy = \frac{true\ positive}{true\ positive + false\ negative + false\ positive} \qquad (25)$$

To ensure accurate results, the semi-automatic identification process incorporates manually identified fibre breaks from large, fused objects and verifies false positives. The miss rate, expressed as a percentage, represents the proportion of fibre breaks that were not detected by the automated algorithms.

$$Miss\ rate = 1 - \frac{true\ positive}{true\ positive + false\ negative} \qquad (26)$$

6.2.4 Results and discussion

The study used SRCT images of a specimen loaded continuously in real-time (in-situ) as a validation set. In comparison to statically acquired images, in-situ images possess a lower resolution and exhibit higher noise levels with less precise object edges due to movement during image acquisition. Notably, voids in the in-situ images do not appear as spheres or ellipsoids, but rather as vortex artefacts with the void serving as their centre, as shown in Figure 48. This presents additional challenges for image processing.

To enhance the quality of the in-situ synchrotron images, super-resolution algorithms were employed, and the resulting images are shown in Figure 49. The resolution was improved from 1.1 μm/pixel to approximately 0.3 μm/pixel, with the size of the LR images increasing from 1089x478x1716 pixel³ to SR images of 4336×1912×6864 pixel³.

The improvement in image quality is evident: the fibre cross-sections become more visible, the fibre edges become well-defined for both visual and computational analysis, and the fibres no longer blend into each other. Although some stitching artefacts are present in the centre of the image in Figure 49a, they are not significant enough to affect the image analysis. These enhanced

images are more suitable for automatic processing. However, since there are no ideal pixel values for SR images, it is not possible to use image-related metrics such as peak signal-to-noise ratio for quantitative assessment as was done in Section 5.2.
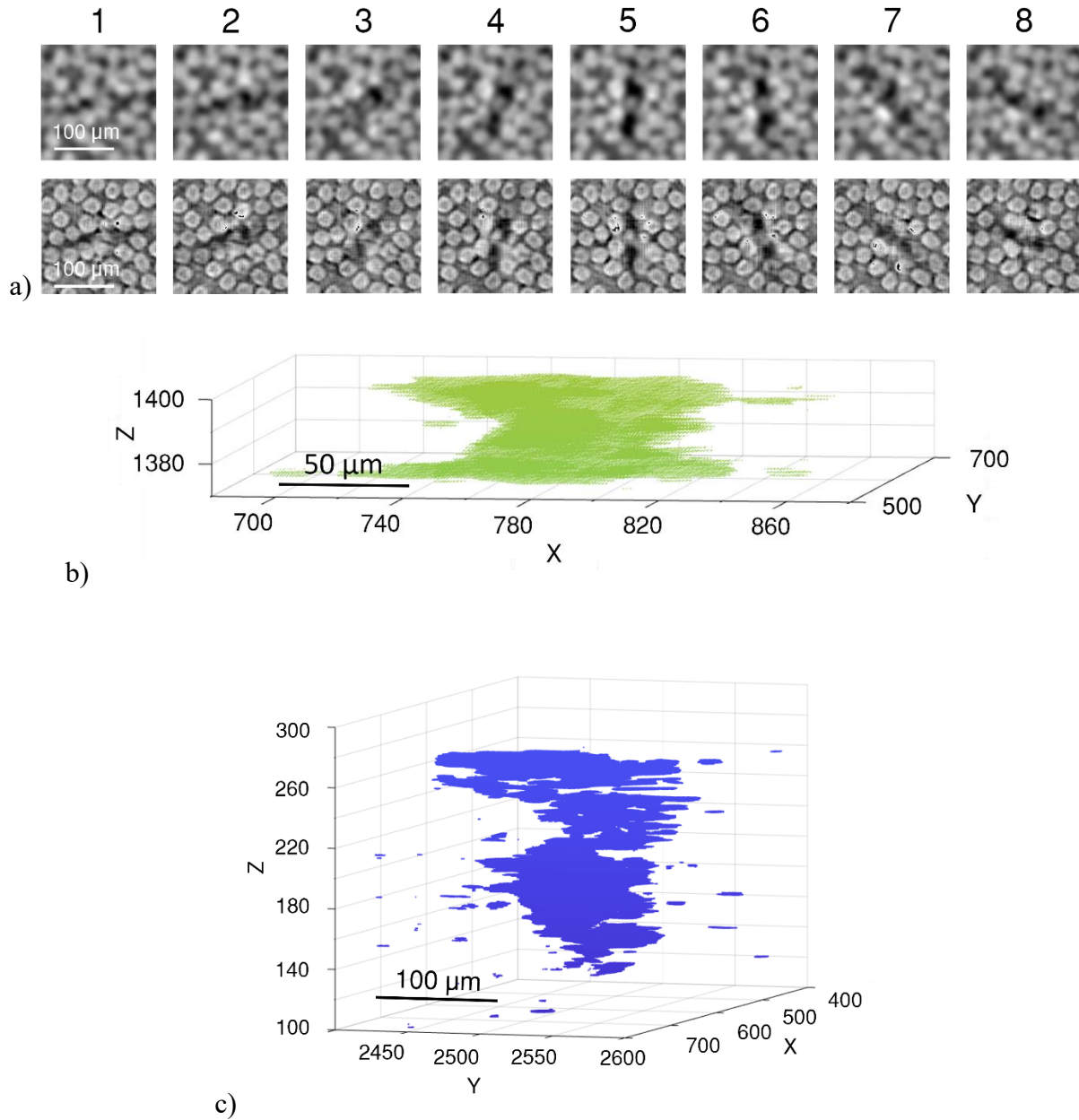
Figure 48 – Low-resolution in-situ scans have vortex artefacts around the large voids: a) slice-by-slice representation of the artefact; b) 3D visualisation of segmented void; c) visualisation of a large, fused object with surrounding noise.

top view

| original | super-resolution | segmentation |

20 μm · 20 μm · 20 μm

a)

top view

| original | super-resolution | segmentation |

20 μm · 20 μm · 20 μm

b)

small volume with
10% of fibres shown

fibre break

20 μm
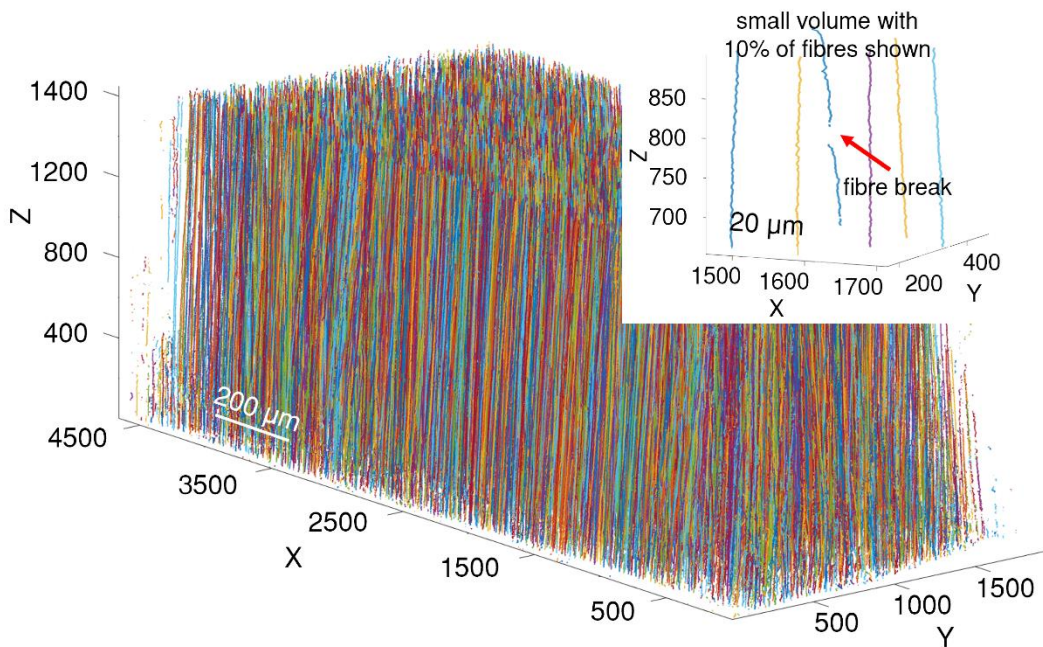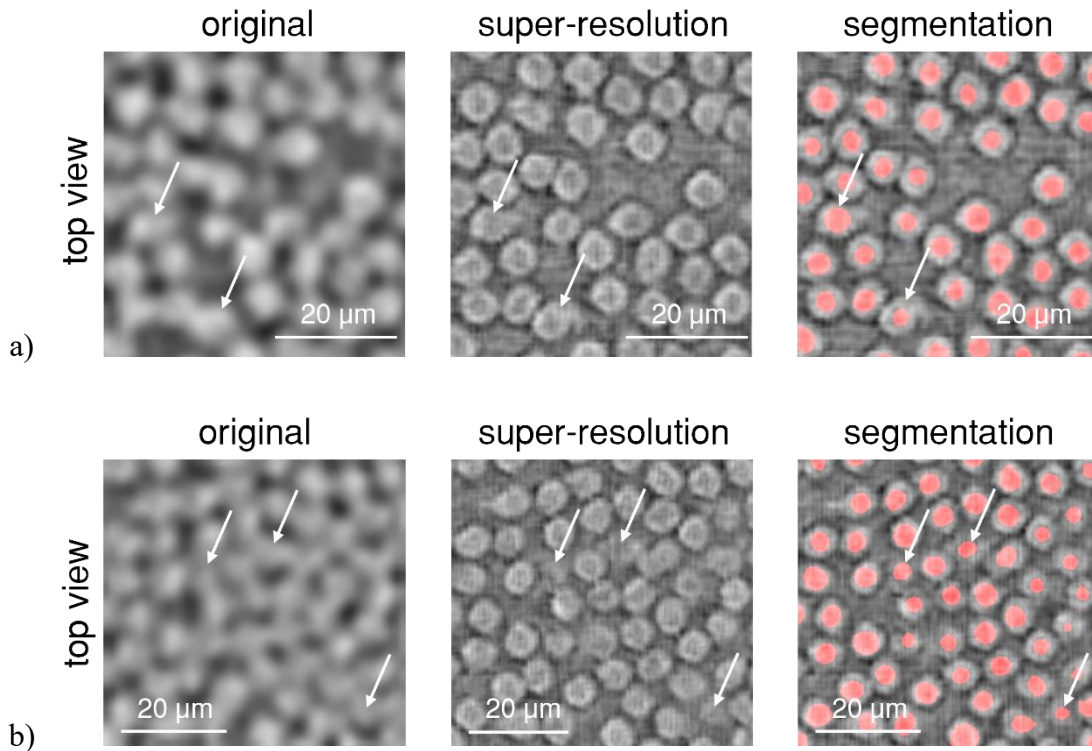
c)

Figure 49 – Super-resolution enhancement of fibres and their segmentation in:
a) common locations; b) challenging locations; c) visualisation of fibre trajectories (a random colour is
assigned to each fibre); in the inset, only 10% of the fibres are shown to demonstrate a fibre break.

Despite the substantial enhancement in image quality achieved through super-resolution, some deviations caused by deep learning are present. First, some fibres appear non-circular. Second, in rare cases, the edges of fibres can blend into the surrounding matrix, as indicated by the white arrow in Figure 49a. Third, in the most challenging cases where all the fibres in the original image are merged, a few reconstructed fibres may be difficult to detect by the human eye, as shown in Figure 49b. Likewise, linear artifacts are noticeable, similar to what's observed in short fibre composite CT image super-resolution. Importantly, these artifacts have minimal impact on the results. However, when using deep learning (U-Net) segmentation, all the fibres are accurately segmented, even in difficult cases where the fibres are represented by small grayscale gradients.

Consistency in the quality enhancement of the reconstruction is observed in all directions throughout the volume, without significant variations in the position of fibre edges or greyscale inconsistencies. This result is attributed to the application of a 3D filter in the super-resolution model and the seamless stitching of small batches to create the whole volume.

Accurate identification of fibre breaks is crucial for reliable analysis of fibre trajectories, and this can be achieved through fibre segmentation using the U-Net neural network and InSegt Fibre code. Figure 49c depicts the result of fibre tracking, where individual fibres are depicted as lines with randomly assigned colours. Reliable fibre segmentation and tracking are imperative for the correct identification of fibre breaks throughout the volume.

More than 90% of the fibres are successfully tracked without interruption or loss of tracking along the entire volume, demonstrating the potential of super-resolution and deep learning segmentation to facilitate automatic fibre tracking in low-resolution CT images of fibre-reinforced composite materials.

In low-resolution CT images (Figure 48) of fibre-reinforced composite materials, voids can be represented in different ways due to the continuous fast scanning, resulting in a few distinct artefacts such as void vortices visible only in 3D, larger size of fibre breaks compared to fibre cross-section, and voids superimposed by fibres, beam hardening, and grey scale inhomogeneities. These artefacts are not present in the training data, making the accurate segmentation of voids and identification of their centres challenging. Moreover, the super-resolution algorithm not only enhances the clarity of fibres and voids but also improves the visibility of these artefacts in the original image. Figure 50a illustrates the described phenomenon. The super-resolution-enhanced void is more clearly visible, however, without the small dark artefacts between the fibres that appear due to their tight packing. Similar small artefacts were also observed in the training data and were explained in Section 5.2. The U-Net segmentation can accurately identify the boundaries of the void, enabling the precise localisation of its centre and identification of fibre breaks. It should be noted that the accuracy of the super-resolution enhancement of voids varies depending on the artefacts present in the original LR image. Nonetheless, the results demonstrate the potential of using super-resolution algorithms and deep learning segmentation for accurate void segmentation and fibre break identification in low-resolution CT images.
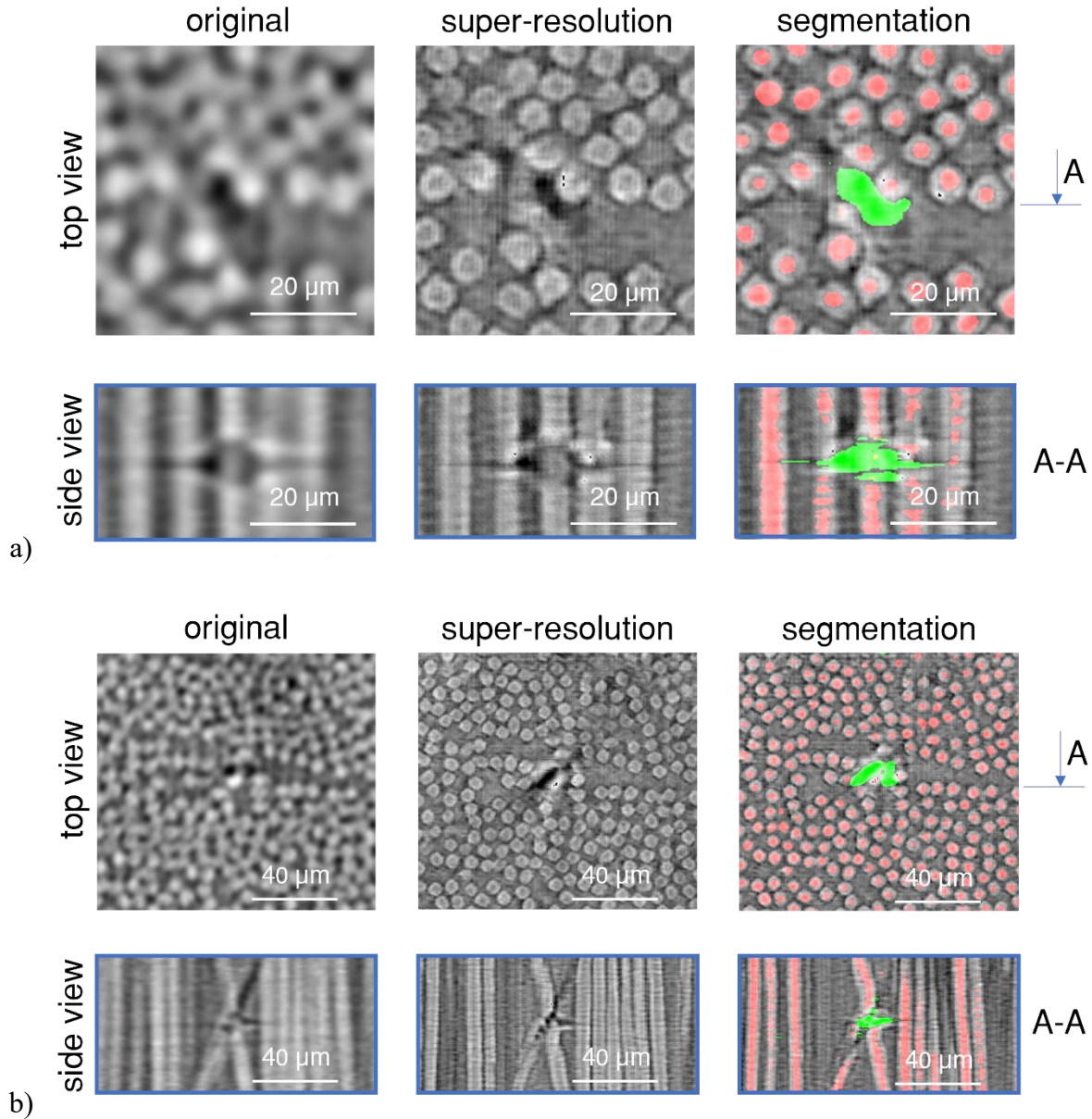
Figure 50 – Segmentation of possible voids and fibre break identification in SR images:
a) example of common quality enhancement of voids; b) challenging case of fibre break identification
where the algorithm was not able to identify it automatically.

The quality enhancement of fibre breaks can be challenging in some cases, as demonstrated in Figure 50b. In this example, a pronounced vortex artefact increased the size of the void in the super-resolution image, making it difficult to accurately segment the fibre break. However, despite the artefacts, shape, and size differences, the centre of the segmented fibre break is correctly

located thanks to the symmetry of the 3D vortex artefact. Figure 50b shows the segmentation of this dark region, which successfully identifies the centre of the fibre break.

The 3D visualisation of the segmented voids is presented in Figure 48b, which clearly shows the vortex artefacts. However, it was not feasible to train the segmentation algorithm to exclusively identify voids without these artefacts.

To identify potential fibre breaks, the segmented voids are analysed to locate objects that have a similar size and shape to known fibre breaks. An average volume for fibre breaks is established through manual analysis and determined to be between 1000 and 50000 pixels in volume, with a diameter of circumscribed ellipsoids longer than 20 pixels. Voids that do not meet these parameters are filtered, leaving only those that could potentially be fibre breaks. Void clusters with a volume much larger than the average fibre break are treated separately, as they may represent a cluster of fibre breaks.

The identification of fibre breaks is carried out in accordance with the procedures outlined in Section 6.2.3, wherein only the central point of the fibre break is recorded (as shown in Figure 49). The accuracy of fibre break detection through the first method relies heavily on the search window and the number of slices used in the analysis, especially when there is no initial stage image available. Although the accuracy can be enhanced by optimising the search parameters through trial and error, flawless identification of all fibre breaks cannot be guaranteed. Nonetheless, using the statistical analysis of void and fibre size to determine the search parameters may lead to lower accuracy in fibre break identification, as demonstrated in Table 17.

In cases where a pre-loading scan is available, the second method can be employed for identifying fibre breaks. This method yields superior results and entails optimising only one parameter, namely the minimum distance between a void centre and the fibre trajectory for

identifying the analysed void as a fibre break. Table 17 illustrates the outcomes of the fibre break identification process utilising both methods.

Table 17 – Statistics of the automated fibre break identification with both methods.

	98% load Method 1 (stat.)	98% load Method 1 (opt.)	98% load Method 2	94% load Method 1 (opt.)	94% load Method 2	75% load Method 1 (opt.)	75% load Method 2
Manual	299	299	299	248	248	78	78
True positive	258	266	272	225	230	74	75
False positive	70	51	33	43	25	14	6
False negative	41	33	27	23	18	4	3
Large objects	79	79	79	39	39	1	1
Fibre breaks from manual	18	18	18	12	12	1	1
Automatic accuracy	0.70	0.76	0.82	0.77	0.84	0.80	0.89
Semi-automatic accuracy	0.79	0.86	0.92	0.85	0.93	0.82	0.92
Miss rate (%)	8.2	5.3	3.2	4.7	2.5	3.9	2.6

When dealing with volumes containing a large number of fibre breaks, the accuracy of fibre break identification tends to decrease. This is primarily due to the algorithm's inability to identify individual fibre breaks in tightly packed fused objects, as depicted in Figure 48.

At this stage of image processing, separating clusters of tightly packed fused objects into individual voids poses a significant challenge. As such, the manual intervention of an operator may be necessary to handle such clusters during image processing. The operator would review the low-resolution, super-resolution, and segmented images, akin to those depicted in Figure 50, and determine the presence of fibre breaks in the images. The operator would then eliminate all false

positive errors from the results, leaving only false negatives unidentified. By employing this approach, along with super-resolution analysis, most fibre breaks in low-resolution images of continuously loaded specimens can be identified in a reasonable amount of time.

The clustering of fibre breaks was carried out using the geometric criteria outlined in Section 6.2.3. For clusters, the results obtained through the second method were used since the initial image was available. Table 18 presents the outcomes of the fibre break cluster identification process, revealing small differences in cluster identification, as depicted in Figure 51c. Such variations arise due to the inconsistency in the ability of the automated algorithm and the operator to locate the centre of the fibre break with the same coordinates. On average, the distance between manually and automatically calculated coordinates is approximately 4.7 µm (in 3D) and can be as much as 10 µm for larger fibre breaks or fused objects. These deviations are similar to the radial distance of 13 µm in the geometric criteria and can influence the clustering of fibre breaks.

Table 18 – Number of fibre break clusters identified with the manual and automated inspection.

		1-plet	2-plet	3-plet	4-plet	5-plet	7-plet
98%	manual	175	43	7	0	2	1
load	auto	170	41	7	0	2	1
94%	manual	145	34	6	0	2	1
load	auto	147	29	6	0	2	1
75%	manual	45	10	1	0	2	0
load	auto	42	9	2	0	2	0

The image processing of enhanced images requires a significant amount of time. After training the super-resolution network, it took roughly four hours of wall-clock time for the SR application to augment the resolution of the entire volume, six hours to segment an SR image into fibres and voids, and an additional hour for image processing tasks such as tracking fibre trajectories, calculating void sizes, and identifying fibre breaks. Furthermore, about an hour of manual work was needed to carefully examine large objects and eliminate false positives in the

image prior to failure, involving the checking of 79 large objects and 328 potential fibre breaks. However, this process is much faster than the 3-5 working days typically required for manual analysis, particularly considering that it only took an hour of hands-on time.
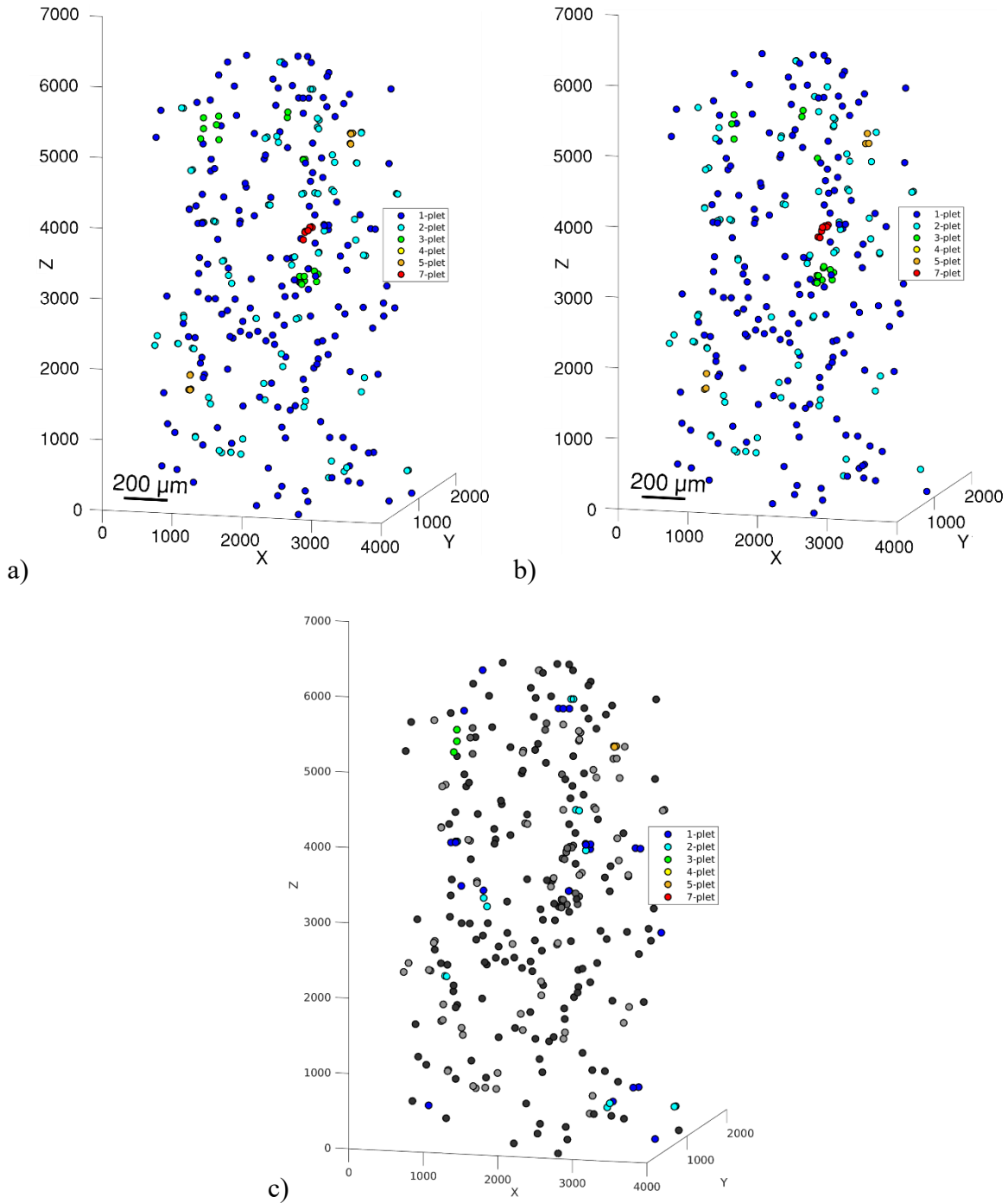
Figure 51 – Location of all fibre breaks and their clusters for a) manual inspection and b) semi-automated inspection. c) small differences are highlighted by colour.

145

Super-resolution is not only useful for identifying fibre breaks in unidirectional composites, but it can also be employed to identify other manufacturing defects in composite materials, such as delamination, matrix cracking, voids, or porosity. The developed algorithm can assist researchers working on models for strength assessment based on fibre breaks. It is possible to attempt to train the algorithm on one material and transfer its super-resolution capabilities to other similar materials, as demonstrated by training on T700SC and validating on 34-700WD. Nevertheless, there are limitations to using machine learning algorithms on data that differ significantly from the training dataset. In such cases, these algorithms will not be able to work effectively. If a new type of feature is introduced in the images, machine learning algorithms will produce unexpected results. For instance, in this study, the neural network was incapable of properly removing vortex artefacts and improving the quality of all voids. The extent to which images can differ from one another and still be used with machine learning algorithms remains an area of further research. Additionally, future research could be focused on exploring more adaptable neural networks that are trained on different materials at varying resolutions.

6.2.5 Conclusion

A deep learning-based super-resolution algorithm that has been developed during this research was utilised to enhance the image quality of synchrotron CT scans with low resolution. The algorithm integrates Enhanced Super-Resolution GAN and CycleGAN and was trained on high-resolution and low-resolution scans of a stationary carbon fibre composite. The algorithm was further tested on a significantly larger low-resolution image of a continuously loaded specimen.

The use of the super-resolution algorithm has led to the generation of images with more accurate fibre and void boundaries, with minimal DL-based artefacts present. To achieve accurate

146

identification of fibres and voids, a U-Net tool called RootPainter was employed for deep-learning-based segmentation. The high quality of the segmentation allows for a detailed analysis of fibre trajectories and void locations.

The super-resolution processing has enabled the automated identification of fibre breaks through the analysis of void locations and fibre trajectories. Two algorithms have been developed: one using only the information from the loaded image and the other one using the fibre trajectories from the unloaded image. The fully automated process achieved average accuracies of 76% and 82%, while the semi-automated process achieved accuracies of 86% and 92%, with a miss rate of less than 5.3%. Clustering of the fibre breaks produced similar results with minor deviations due to inconsistent fibre break centre locations. With super-resolution, it is possible to use faster, low-resolution in-situ CT scans on continuously loaded specimens without significant compromises on the quality of physical parameter identification. This methodology can provide faster, albeit less accurate, fibre break identification for strength assessment models.

6.3 Chapter conclusion

This chapter provides two verification applications of the developed algorithms. The first is devoted to the generation of periodic RVEs of short fibre composite, and the second to the enabling automated identification of fibre breaks in carbon unidirectional composites.

A new technique called modified inpainting GAN was developed to create periodic RVEs. This was achieved by modifying a neural network to include periodic layers and a resemblance critic, which resulted in high-quality periodic RVEs which were enhanced using super-resolution. Deep learning algorithms were used to segment the fibres in both the original and periodic RVEs, resulting in the creation of probability volumes. These probability volumes were then used to

create voxel and tetrahedral models using different software. Simulations were carried out on both RVEs with periodic boundary conditions, and the results showed that the periodic RVE had significantly better boundary treatment without any property jumps from one to opposite faces compared to the original RVE. Furthermore, the tetrahedral models were found to be more accurate for local field representation, but they were also more challenging to handle.

The super-resolution algorithm was trained on images of one composite material and tested on a low-resolution image of another continuously loaded specimen. High-quality images were generated with accurate fibre and void boundaries. Deep learning-based segmentation was employed for the accurate identification of fibres and voids, allowing for detailed analysis of fibre trajectories and void locations. The super-resolution processing enabled the automated identification of fibre breaks using two algorithms: one using only the loaded image and the other using the fibre trajectories from an unloaded image. Both achieved high accuracies with a low miss rate. With this method, faster, low-resolution in-situ CT scans can be used for continuous loading without significant loss of accuracy. This approach can provide faster fibre break identification for strength assessment models.

Chapter 7. Conclusion and future perspective.

7.1 Main achievements and impact

The focus of this thesis was to overcome the challenges associated with the investigation of composite materials using X-ray CT image processing techniques. These challenges included image artefacts, the trade-off between spatial resolution and specimen size, and the application of periodic boundary conditions to CT-based finite element models. To address these challenges, the study used deep learning techniques to accurately process the CT images of the materials. The research objectives of the study were to develop generative and super-resolution algorithms and to analyse existing segmentation software. Using these techniques, the study demonstrated the potential of deep learning methods to process X-ray tomography images of composite materials to generate periodic RVEs for micromechanical analysis and to enable automated identification of material defects from the LR image. These methods can be applied to a wide range of fields and materials.

This work has led to the development of a CT processing pipeline that leverages deep learning methods, with the aim of improving the analysis of composite materials. This pipeline is based on several key achievements:

1) The deep learning generative algorithm was developed for image volume inpainting in CT scans. The algorithm can effectively regenerate missing parts of the input data and can be used to remove image artefacts and material defects. Furthermore, this approach can be used to alter the representation of the material microstructure. The verification results show that the proposed methodology allows accurate generation of missing regions based on known information about the material's microstructure. Three different neural network architectures were tested, and the deepest neural network outperformed the others, although it requires a lot of GPU memory.

149

2) The developed super-resolution algorithm for CT scanning has shown the potential to significantly improve the image quality of composite materials. By addressing the limitations of current CT imaging techniques, this algorithm allows the acquisition of larger regions of interest with higher resolution and quality without sacrificing scan time. The improved image quality can enable more accurate analysis and modelling of the microstructure of composite materials.

3) The analysis of existing segmentation algorithms for CT image processing has been carried out as an important tool in the study of composite materials. Accurate identification and analysis of different constituents of the material microstructure, such as fibres, matrix and voids, is crucial for data-driven prediction of mechanical properties. By selecting the most appropriate segmentation algorithm for specific research objectives and CT imaging data, the accuracy of analysis and prediction of mechanical properties can be significantly improved.

The effectiveness of these methods in improving the analysis of composite materials has been demonstrated by their application to the following two cases:

1) The methodology of using the DL methods has been developed for generating periodic data-driven RVEs for finite element analysis of composite materials, as one of the most challenging objectives of this work. By using a modified inpainting algorithm, a larger periodic volume can be generated from the initial CT image while preserving the physical description of the material microstructure. This approach allows the implementation of periodic boundary conditions in finite element analysis to CT-based models, leading to more accurate calculation of effective properties and faster computational convergence. The proposed approach provides a powerful tool for periodic RVE generation and subsequent prediction of mechanical properties of composite materials.

2) This research has also achieved the goal of enabling automated algorithms to identify fibre breaks in time-resolved synchrotron-based CT scans. It has been demonstrated that by using the super-resolution and deep learning segmentation algorithms, researchers can now quickly and accurately identify fibre breaks in large volumes of CT image data. This enables faster analysis and more efficient identification of potential material defects or other physical descriptors of a material.

The developed methods, including inpainting generative and super-resolution algorithms, combined with existing deep learning segmentation algorithms, are expected to lead to more accurate CT data analysis and modelling of composite materials, which can be beneficial in a wide range of applications, including the design and manufacture of composite structures with improved properties and performance. This research has the potential to advance the field of materials science and engineering by advancing the understanding and application of deep learning generated structures in materials science and finite element simulations. The research may open new routes for the development of more reliable and robust composite materials through a better understanding of their microstructure and mechanical properties.

At this stage, the research results may not be directly applicable to engineering practices due to the complexities of data collection and deep learning model training. However, the developed algorithm has the potential to be integrated into existing FEM or CT software. Engineers could then use this software to obtain initial predictions of effective mechanical properties based on limited material samples, reducing the need for extensive and often costly full-scale mechanical testing at first stages of composite material development.

7.2 Limitations and future developments

There are several limitations of the developed methods that should be considered. The main limitation is that deep learning techniques are usually learned on one type of data and are not easily transferable to other types of data. It is also essential to consider specific limitations of the effectiveness of each objective, which may include the following points.

The inpainting algorithm may face challenges in accurately regenerating missing parts of the input volume if the amount of missing data is significant, or the input volume is limited. To address this issue, deeper neural networks can be developed and trained using a larger dataset of CT scans of materials. This has the potential to mitigate the limitation and improve the effectiveness of the methodology.

The super-resolution algorithm may not be effective in enhancing the quality of CT images with significant noise or artefacts, which can lead to inaccurate data analysis, as demonstrated with the super-resolution of regenerated images. Also, the automated algorithm for identifying fibre breaks in time-resolved synchrotron-based CT scans may not be effective in detecting small features that are smaller than the initial spatial resolution of a CT, in which case there is no information in the CT data about that feature. To address this issue in the future, there is potential to create a more universal super-resolution model that can be trained on CT images from a single CT system. The universal super-resolution model should be continuously trained on different CT datasets, enabling it to consistently improve the quality of CT images across different materials and scenarios. This would require a significant increase in the number of trainable parameters and training on a more diverse set of materials, which would require the use of specialised high-performance clusters. This will provide a more robust and generalised super-resolution model that

can be applied to this specific CT system to improve the image quality of a wider range of materials.

Super-resolution techniques can improve industrial X-ray computed tomography, but they also carry the risk of false-positive defect identification due to assumptions about image structure and noise enhancement. To avoid this risk, it is important to validate and calibrate super-resolution techniques, establish clear defect criteria, and combine with other imaging techniques to confirm defects and eliminate false positives. In addition, the super-resolution algorithm has the potential to address several challenging tasks, for example, the identification of other compact small objects, such as microvoids.

Existing segmentation algorithms are useful for identifying different constituents of composite materials, they may not be suitable for the type of materials with many more than 3 classes of features in an image, or for identifying descriptors that are not easily identified by the human eye and, therefore, properly annotated. One way to overcome this limitation, presented in this work, is to apply super-resolution to improve image quality for easier annotation.

The generation of periodic RVE may produce nonphysical results for the RVE of some materials where the periodicity cannot be achieved due to the complex, rigid geometry that cannot be altered. Further research can investigate how the periodic inpainting algorithm developed in this study can potentially find useful applications in other areas, such as the analysis of weak periodicity in the unit cells of textile composites. In addition to its specific use cases in calculations, the periodic inpainting technique has the potential to be utilized for assessing the tolerance levels for PBC violation. Although weak PBC may not significantly affect homogenization, it can result in an erroneous stress-strain field formation the boundary layer.

Bibliography

[1]   Swolfs Y, Morton H, Scott AE, Gorbatikh L, Reed PAS, Sinclair I, et al. Synchrotron radiation computed tomography for experimental validation of a tensile strength model for unidirectional fibre-reinforced composites. Compos Part A Appl Sci Manuf 2015;77:106–13. https://doi.org/10.1016/j.compositesa.2015.06.018.

[2]   Bargmann S, Klusemann B, Markmann J, Schnabel JE, Schneider K, Soyarslan C, et al. Generation of 3D representative volume elements for heterogeneous materials: A review. Prog Mater Sci 2018;96:322–84. https://doi.org/10.1016/j.pmatsci.2018.02.003.

[3]   Naouar N, Vasiukov D, Park CH, Lomov S V., Boisse P. Meso-FE modelling of textile composites and X-ray tomography. J Mater Sci 2020;55:16969–89. https://doi.org/10.1007/s10853-020-05225-x.

[4]   Gu GX, Chen CT, Buehler MJ. De novo composite design based on machine learning algorithm. Extreme Mech Lett 2018;18:19–28. https://doi.org/10.1016/j.eml.2017.10.001.

[5]   Charalambakis N. Homogenization techniques and micromechanics. A survey and perspectives. Appl Mech Rev 2010;63:1–10. https://doi.org/10.1115/1.4001911.

[6]   Gibson RF. A review of recent research on mechanics of multifunctional composite materials and structures. Compos Struct 2010;92:2793–810. https://doi.org/10.1016/j.compstruct.2010.05.003.

[7]   Yuan Z, Fish J. Toward realization of computational homogenization in practice. Int J Numer Methods Eng 2008;73:361–80. https://doi.org/10.1002/nme.2074.

[8]   Liu X, Tian S, Tao F, Yu W. A review of artificial neural networks in the constitutive modeling of composite materials. Compos B Eng 2021;224. https://doi.org/10.1016/j.compositesb.2021.109152.

[9]   Bishara D, Xie Y, Liu WK, Li S. A State-of-the-Art Review on Machine Learning-Based Multiscale Modeling, Simulation, Homogenization and Design of Materials. Archives of Computational Methods in Engineering 2023;30:191–222. https://doi.org/10.1007/s11831-022-09795-8.

[10]   Bostanabad R, Zhang Y, Li X, Kearney T, Brinson LC, Apley DW, et al. Computational microstructure characterization and reconstruction: Review of the state-of-the-art techniques. Prog Mater Sci 2018;95:1–41. https://doi.org/10.1016/j.pmatsci.2018.01.005.

[11]   Kachanov M, Sevostianov I. Micromechanics of Materials, with Applications. vol. 249. Cham: Springer International Publishing; 2018. https://doi.org/10.1007/978-3-319-76204-3.

[12]   Eshelby JD. The determination of the elastic field of an ellipsoidal inclusion, and related problems. Proc R Soc Lond A Math Phys Sci 1957;241:376–96. https://doi.org/10.1098/rspa.1957.0133.

[13]   T M, K T. Average stress in matrix and average elastic energy of materials with misfitting inclusions. Acta Metallurgica 1973;21:571–574. https://doi.org/10.1016/0001-6160(73)90064-3.

[14]   Jain A. Micro and mesomechanics of fibre reinforced composites using mean field homogenization formulations: A review. Mater Today Commun 2019;21:100552. https://doi.org/10.1016/j.mtcomm.2019.100552.

[15]   Abaimov SG, Akhatov IS, Lomov S V. Detailed comparison of analytical and finite element–based homogenization approaches for fibre-reinforced composites. Multi-Scale Continuum Mechanics Modelling of Fibre-Reinforced Polymer Composites, Elsevier; 2021, p. 141–77. https://doi.org/10.1016/B978-0-12-818984-9.00006-8.

[16]   Singh H. EFFECT OF SIZE, SHAPE AND ORIENTATION OF INCLUSIONS ON HOMOGENIZED PARAMETERS OF HETEROGENEOUS MATERIALS. 2019.

[17]   Thionnet A, Chou HY, Bunsell A. Fibre break processes in unidirectional composites. Compos Part A Appl Sci Manuf 2014;65:148–60. https://doi.org/10.1016/j.compositesa.2014.06.009.

[18]   Salnikov V, Choï D, Karamian-Surville P. On efficient and reliable stochastic generation of RVEs for analysis of composites within the framework of homogenization. Comput Mech 2015;55:127–44. https://doi.org/10.1007/s00466-014-1086-1.

[19] Zeman J, Šejnoha M. From random microstructures to representative volume elements. Model Simul Mat Sci Eng, vol. 15, 2007. https://doi.org/10.1088/0965-0393/15/4/S01.

[20] Stier B, Simon JW, Reese S. Comparing experimental results to a numerical meso-scale approach for woven fiber reinforced plastics. Compos Struct 2015;122:553–60. https://doi.org/10.1016/j.compstruct.2014.12.015.

[21] Madra A, Breitkopf P, Rassineux A, Trochu F. Image-based model reconstruction and meshing of woven reinforcements in composites. Int J Numer Methods Eng 2017;112:1235–52. https://doi.org/10.1002/nme.5555.

[22] Emerson MJ, Jespersen KM, Dahl AB, Conradsen K, Mikkelsen LP. Individual fibre segmentation from 3D X-ray computed tomography for characterising the fibre orientation in unidirectional composite materials. Compos Part A Appl Sci Manuf 2017;97:83–92. https://doi.org/10.1016/j.compositesa.2016.12.028.

[23] Garcea SC, Wang Y, Withers PJ. X-ray computed tomography of polymer composites. Compos Sci Technol 2018;156:305–19. https://doi.org/10.1016/j.compscitech.2017.10.023.

[24] Gao Y, Hu W, Xin S, Sun L. A review of applications of CT imaging on fiber reinforced composites. J Compos Mater 2022;56:133–64. https://doi.org/10.1177/00219983211050705.

[25] Chen J, Yu Z, Jin H. Nondestructive testing and evaluation techniques of defects in fiber-reinforced polymer composites: A review. Front Mater 2022;9. https://doi.org/10.3389/fmats.2022.986645.

[26] Stock SR. X-ray microtomography of materials. International Materials Reviews 1999;44:141–64. https://doi.org/10.1179/095066099101528261.

[27] Stock SR. Recent advances in X-ray microtomography applied to materials. International Materials Reviews 2008;53:129–81. https://doi.org/10.1179/174328008X277803.

[28] Garcea SC, Sinclair I, Spearing SM. Fibre failure assessment in carbon fibre reinforced polymers under fatigue loading by synchrotron X-ray computed tomography. Compos Sci Technol 2016;133:157–64. https://doi.org/10.1016/j.compscitech.2016.07.030.

[29] Yu B, Bradley RS, Soutis C, Withers PJ. A comparison of different approaches for imaging cracks in composites by X-ray microtomography. Philosophical Transactions of the Royal Society A: Mathematical, Physical and Engineering Sciences, vol. 374, Royal Society of London; 2016. https://doi.org/10.1098/rsta.2016.0037.

[30] Wisnom MR. Size effects in the testing of fibre-composite materials. Compos Sci Technol 1999;59:1937–57. https://doi.org/10.1016/S0266-3538(99)00053-6.

[31] Yu B, Blanc R, Soutis C, Withers PJ. Evolution of damage during the fatigue of 3D woven glass-fibre reinforced composites subjected to tension-tension loading observed by time-lapse X-ray tomography. Compos Part A Appl Sci Manuf 2016;82:279–90. https://doi.org/10.1016/j.compositesa.2015.09.001.

[32] Eekhoff JD, Lake SP. Three-dimensional computation of fibre orientation, diameter and branching in segmented image stacks of fibrous networks. J R Soc Interface 2020;17. https://doi.org/10.1098/rsif.2020.0371.

[33] Çinar K, Ersoy N. Effect of fibre wrinkling to the spring-in behaviour of L-shaped composite materials. Compos Part A Appl Sci Manuf 2015;69:105–14. https://doi.org/10.1016/j.compositesa.2014.10.025.

[34] Zhou XY, Qian SY, Wang NW, Xiong W, Wu WQ. A review on stochastic multiscale analysis for FRP composite structures. Compos Struct 2022;284. https://doi.org/10.1016/j.compstruct.2021.115132.

[35] Agrawal S, Singh KK, Sarkar PK. Impact damage on fibre-reinforced polymer matrix composite - A review. J Compos Mater 2014;48:317–32. https://doi.org/10.1177/0021998312472217.

[36] Rus J, Gustschin A, Mooshofer H, Grager JC, Bente K, Gaal M, et al. Qualitative comparison of non-destructive methods for inspection of carbon fiber-reinforced polymer laminates. J Compos Mater 2020;54:4325–37. https://doi.org/10.1177/0021998320931162.

[37] Badran A, Marshall D, Legault Z, Makovetsky R, Provencher B, Piché N, et al. Automated segmentation of computed tomography images of fiber-reinforced composites by deep learning. J Mater Sci 2020;55:16273–89. https://doi.org/10.1007/s10853-020-05148-7.

[38] Badran A, Parkinson D, Ushizima D, Marshall D, Maillet E. Validation of Deep Learning Segmentation of CT Images of Fiber-Reinforced Composites. Journal of Composites Science 2022;6. https://doi.org/10.3390/jcs6020060.

[39] Straumit I, Lomov S V., Wevers M. Quantification of the internal structure and automatic generation of voxel models of textile composites from X-ray computed tomography data. Compos Part A Appl Sci Manuf 2015;69:150–8. https://doi.org/10.1016/j.compositesa.2014.11.016.

[40] Wielhorski Y, Mendoza A, Rubino M, Roux S. Numerical modeling of 3D woven composite reinforcements: A review. Compos Part A Appl Sci Manuf 2022;154. https://doi.org/10.1016/j.compositesa.2021.106729.

[41] Ansar M, Xinwei W, Chouwei Z. Modeling strategies of 3D woven composites: A review. Compos Struct 2011;93:1947–63. https://doi.org/10.1016/j.compstruct.2011.03.010.

[42] Breite C, Melnikov A, Turon A, de Morais AB, Otero F, Mesquita F, et al. Blind benchmarking of seven longitudinal tensile failure models for two virtual unidirectional composites. Compos Sci Technol 2021;202. https://doi.org/10.1016/j.compscitech.2020.108555.

[43] Breite C, Melnikov A, Turon A, de Morais AB, Le Bourlot C, Maire E, et al. Detailed experimental validation and benchmarking of six models for longitudinal tensile failure of unidirectional composites. Compos Struct 2022;279. https://doi.org/10.1016/j.compstruct.2021.114828.

[44] Thionnet A, Bunsell AR. Fibre break failure processes in unidirectional composites: Evaluation of critical damage states. Philosophical Transactions of the Royal Society A: Mathematical, Physical and Engineering Sciences, vol. 374, Royal Society of London; 2016. https://doi.org/10.1098/rsta.2015.0270.

[45] Xia Z, Zhang Y, Ellyin F. A unified periodical boundary conditions for representative volume elements of composites and applications. Int J Solids Struct 2003;40:1907–21. https://doi.org/10.1016/S0020-7683(03)00024-6.

[46] Mirkhalaf SM, Andrade Pires FM, Simoes R. Determination of the size of the Representative Volume Element (RVE) for the simulation of heterogeneous polymers at finite strains. Finite Elements in Analysis and Design 2016;119:30–44. https://doi.org/10.1016/j.finel.2016.05.004.

[47] Kanit T, Forest S, Galliet I, Mounoury V, Jeulin D. Determination of the size of the representative volume element for random composites: Statistical and numerical approach. Int J Solids Struct 2003;40:3647–79. https://doi.org/10.1016/S0020-7683(03)00143-4.

[48] Sharma R, Mahajan P, Mittal RK. Elastic modulus of 3D carbon/carbon composite using image-based finite element simulations and experiments. Compos Struct 2013;98:69–78. https://doi.org/10.1016/j.compstruct.2012.11.019.

[49] Sharma R, Mahajan P, Mittal RK. Fiber bundle push-out test and image-based finite element simulation for 3D carbon/carbon composites. Carbon N Y 2012;50:2717–25. https://doi.org/10.1016/j.carbon.2012.02.030.

[50] Fang G, Liang J. A review of numerical modeling of three-dimensional braided textile composites. J Compos Mater 2011;45:2415–36. https://doi.org/10.1177/0021998311401093.

[51] Park JM, Park SJ. Modeling and simulation of fiber orientation in injection molding of polymer composites. Math Probl Eng 2011;2011. https://doi.org/10.1155/2011/105637.

[52] Lomov SV, Gusakov AV, Huysmans G, Prodromou A, Verpoest I. Textile geometry preprocessor for meso-mechanical models of woven composites. Compos Sci Technol 2000;60:2083–95. https://doi.org/10.1016/S0266-3538(00)00121-4.

[53] Lomov SV, Huysmans G, Luo Y, Parnas RS, Prodromou A, Verpoest I, et al. Textile composites: modelling strategies. Compos Part A Appl Sci Manuf 2001;32:1379–94. https://doi.org/10.1016/S1359-835X(01)00038-0.

[54] Gaiselmann G, Froning D, Tötzke C, Quick C, Manke I, Lehnert W, et al. Stochastic 3D modeling of non-woven materials with wet-proofing agent. Int J Hydrogen Energy 2013;38:8448–60. https://doi.org/10.1016/j.ijhydene.2013.04.144.

[55] Kari S, Berger H, Rodriguez-Ramos R, Gabbert U. Computational evaluation of effective material properties of composites reinforced by randomly distributed spherical particles. Compos Struct 2007;77:223–31. https://doi.org/10.1016/j.compstruct.2005.07.003.

[56] Schneider K, Klusemann B, Bargmann S. Automatic three-dimensional geometry and mesh generation of periodic representative volume elements for matrix-inclusion composites. Advances in Engineering Software 2016;99:177–88. https://doi.org/10.1016/j.advengsoft.2016.06.001.

[57] Badel P, Vidal-Sallé E, Maire E, Boisse P. Simulation and tomography analysis of textile composite reinforcement deformation at the mesoscopic scale. Compos Sci Technol 2008;68:2433–40. https://doi.org/10.1016/j.compscitech.2008.04.038.

[58] Daelemans L, Faes J, Allaoui S, Hivet G, Dierick M, Van Hoorebeke L, et al. Finite element simulation of the woven geometry and mechanical behaviour of a 3D woven dry fabric under tensile and shear loading using the digital element method. Compos Sci Technol 2016;137:177–87. https://doi.org/10.1016/j.compscitech.2016.11.003.

[59] Wintiba B, Vasiukov D, Panier S, Lomov S V., Ehab Moustafa Kamel K, Massart TJ. Automated reconstruction and conformal discretization of 3D woven composite CT scans with local fiber volume fraction control. Compos Struct 2020;248:112438. https://doi.org/10.1016/j.compstruct.2020.112438.

[60] Liu Y, Straumit I, Vasiukov D, Lomov S V., Panier S. Prediction of linear and non-linear behavior of 3D woven composite using mesoscopic voxel models reconstructed from X-ray micro-tomography. Compos Struct 2017;179:568–79. https://doi.org/10.1016/j.compstruct.2017.07.066.

[61] Kim DW, Lim JH, Kim SW, Kim YH. Micro-computed tomography-aided modeling for misaligned and noncircular fibers of unidirectional composites and validation under a transverse tensile loading. Compos Sci Technol 2021;212. https://doi.org/10.1016/j.compscitech.2021.108879.

[62] Naili C, Doghri I, Kanit T, Sukiman MS, Aissa-Berraies A, Imad A. Short fiber reinforced composites: Unbiased full-field evaluation of various homogenization methods in elasticity. Compos Sci Technol 2020;187. https://doi.org/10.1016/j.compscitech.2019.107942.

[63] Mehta A, Schneider M. A sequential addition and migration method for generating microstructures of short fibers with prescribed length distribution. Comput Mech 2022;70:829–51. https://doi.org/10.1007/s00466-022-02201-x.

[64] Hessman PA, Riedel T, Welschinger F, Hornberger K, Böhlke T. Microstructural analysis of short glass fiber reinforced thermoplastics based on x-ray micro-computed tomography. Compos Sci Technol 2019;183. https://doi.org/10.1016/j.compscitech.2019.107752.

[65] Zhong Y, Liu P, Pei Q, Sorkin V, Louis Commillus A, Su Z, et al. Elastic properties of injection molded short glass fiber reinforced thermoplastic composites. Compos Struct 2020;254. https://doi.org/10.1016/j.compstruct.2020.112850.

[66] Hill R. Elastic properties of reinforced solids: Some theoretical principles. J Mech Phys Solids 1963;11:357–72. https://doi.org/10.1016/0022-5096(63)90036-X.

[67] Bakhvalov N, Panasenko G. Homogenisation: Averaging Processes in Periodic Media. vol. 36. Springer Netherlands; 1989. https://doi.org/10.1007/978-94-009-2247-1.

[68] Song W, Krishnaswamy V, Pucha R V. Computational homogenization in RVE models with material periodic conditions for CNT polymer composites. Compos Struct 2016;137:9–17. https://doi.org/10.1016/j.compstruct.2015.11.013.

[69] Jendrysik N, Schneider K, Bargmann S. Automatic generation and discretization of fully periodic representative volume elements of plain woven composites. J Compos Mater 2018;52:4061–73. https://doi.org/10.1177/0021998318774403.

[70] Campillo M, Sedaghati R, Drew RAL, Alfonso I, Pérez L. Development of an RVE using a DEM–FEM scheme under modified approximate periodic boundary condition to estimate the elastic

mechanical properties of open foams. Eng Comput 2022;38:1767–85. https://doi.org/10.1007/s00366-021-01355-1.

[71]   Lomov S V., Ivanov DS, Verpoest I, Zako M, Kurashiki T, Nakai H, et al. Meso-FE modelling of textile composites: Road map, data flow and algorithms. Compos Sci Technol 2007;67:1870–91. https://doi.org/10.1016/j.compscitech.2006.10.017.

[72]   Jacques S, De Baere I, Van Paepegem W. Application of periodic boundary conditions on multiple part finite element meshes for the meso-scale homogenization of textile fabric composites. Compos Sci Technol 2014;92:41–54. https://doi.org/10.1016/j.compscitech.2013.11.023.

[73]   Schneider K, Klusemann B, Bargmann S. Fully periodic RVEs for technological relevant composites: Not worth the effort! J Mech Mater Struct 2017;12:471–84. https://doi.org/10.2140/JOMMS.2017.12.471.

[74]   Müzel SD, Bonhin EP, Guimarães NM, Guidi ES. Application of the finite element method in the analysis of composite materials: A review. Polymers (Basel) 2020;12. https://doi.org/10.3390/POLYM12040818.

[75]   Doitrand A, Fagiano C, Irisarri FX, Hirsekorn M. Comparison between voxel and consistent meso-scale models of woven composites. Compos Part A Appl Sci Manuf 2015;73:143–54. https://doi.org/10.1016/j.compositesa.2015.02.022.

[76]   Fang G, El Said B, Ivanov D, Hallett SR. Smoothing artificial stress concentrations in voxel-based models of textile composites. Compos Part A Appl Sci Manuf 2016;80:270–84. https://doi.org/10.1016/j.compositesa.2015.10.025.

[77]   Withers PJ, Bouman C, Carmignato S, Cnudde V, Grimaldi D, Hagen CK, et al. X-ray computed tomography. Nature Reviews Methods Primers 2021;1. https://doi.org/10.1038/s43586-021-00015-4.

[78]   Yang H, Wang WF, Shang JC, Wang PD, Lei H, Chen H sen, et al. Segmentation of computed tomography images and high-precision reconstruction of rubber composite structure based on deep learning. Compos Sci Technol 2021;213. https://doi.org/10.1016/j.compscitech.2021.108875.

[79]   Creveling PJ, Whitacre WW, Czabaj MW. A fiber-segmentation algorithm for composites imaged using X-ray microtomography: Development and validation. Compos Part A Appl Sci Manuf 2019;126. https://doi.org/10.1016/j.compositesa.2019.105606.

[80]   Eberhardt CN, Clarke AR. Automated reconstruction of curvilinear fibres from 3D datasets acquired by X-ray microtomography. J Microsc 2002;206:41–53. https://doi.org/10.1046/j.1365-2818.2002.01009.x.

[81]   Kopp R, Joseph J, Ni X, Roy N, Wardle BL. Deep Learning Unlocks X-ray Microtomography Segmentation of Multiclass Microdamage in Heterogeneous Materials. Advanced Materials 2022;34. https://doi.org/10.1002/adma.202107817.

[82]   Meister S, Wermes MAM, Stüve J, Groves RM. Review of image segmentation techniques for layup defect detection in the Automated Fiber Placement process: A comprehensive study to improve AFP inspection. J Intell Manuf 2021;32:2099–119. https://doi.org/10.1007/s10845-021-01774-3.

[83]   Thomas AJ, Barocio E, Pipes RB. A machine learning approach to determine the elastic properties of printed fiber-reinforced polymers. Compos Sci Technol 2022;220. https://doi.org/10.1016/j.compscitech.2022.109293.

[84]   Lionetto F, Montagna F, Natali D, De Pascalis F, Nacucchi M, Caretto F, et al. Correlation between elastic properties and morphology in short fiber composites by X-ray computed micro-tomography. Compos Part A Appl Sci Manuf 2021;140. https://doi.org/10.1016/j.compositesa.2020.106169.

[85]   Zhang Z, Friedrich K. Artificial neural networks applied to polymer composites: A review. Compos Sci Technol 2003;63:2029–44. https://doi.org/10.1016/S0266-3538(03)00106-4.

[86]   El Kadi H. Modeling the mechanical behavior of fiber-reinforced polymeric composite materials using artificial neural networks - A review. Compos Struct 2006;73:1–23. https://doi.org/10.1016/j.compstruct.2005.01.020.

[87]   Chen CT, Gu GX. Machine learning for composite materials. MRS Commun 2019;9:556–66. https://doi.org/10.1557/mrc.2019.32.

[88]   Bishara D, Xie Y, Liu WK, Li S. A State-of-the-Art Review on Machine Learning-Based Multiscale Modeling, Simulation, Homogenization and Design of Materials. Archives of Computational Methods in Engineering 2023;30:191–222. https://doi.org/10.1007/s11831-022-09795-8.

[89]   Jiang T, Gradus JL, Rosellini AJ. Supervised Machine Learning: A Brief Primer. 2020.

[90]   Usama M, Qadir J, Raza A, Arif H, Yau KLA, Elkhatib Y, et al. Unsupervised Machine Learning for Networking: Techniques, Applications and Research Challenges. IEEE Access 2019;7:65579–615. https://doi.org/10.1109/ACCESS.2019.2916648.

[91]   Li Y. Reinforcement Learning in Practice: Opportunities and Challenges 2022.

[92]   Abadi M, Barham P, Chen J, Chen Z, Davis A, Dean J, et al. TensorFlow: A system for large-scale machine learning. 12th USENIX Symposium on Operating Systems Design and Implementation (OSDI 16) 2016:265–83.

[93]   Alzubaidi L, Zhang J, Humaidi AJ, Al-Dujaili A, Duan Y, Al-Shamma O, et al. Review of deep learning: concepts, CNN architectures, challenges, applications, future directions. J Big Data 2021;8. https://doi.org/10.1186/s40537-021-00444-8.

[94]   Le BA, Yvonnet J, He QC. Computational homogenization of nonlinear elastic materials using neural networks. Int J Numer Methods Eng 2015;104:1061–84. https://doi.org/10.1002/nme.4953.

[95]   Yang C, Kim Y, Ryu S, Gu GX. Prediction of composite microstructure stress-strain curves using convolutional neural networks. Mater Des 2020;189:108509. https://doi.org/10.1016/j.matdes.2020.108509.

[96]   Wang K, Sun WC. A multiscale multi-permeability poroplasticity model linked by recursive homogenizations and deep learning. Comput Methods Appl Mech Eng 2018;334:337–80. https://doi.org/10.1016/j.cma.2018.01.036.

[97]   Guo K, Yang Z, Yu CH, Buehler MJ. Artificial intelligence and machine learning in design of mechanical materials. Mater Horiz 2021;8:1153–72. https://doi.org/10.1039/d0mh01451f.

[98]   Liu Z, Bessa MA, Liu WK. Self-consistent clustering analysis: An efficient multi-scale scheme for inelastic heterogeneous materials. Comput Methods Appl Mech Eng 2016;306:319–41. https://doi.org/10.1016/j.cma.2016.04.004.

[99]   Karniadakis GE, Kevrekidis IG, Lu L, Perdikaris P, Wang S, Yang L. Physics-informed machine learning. Nature Reviews Physics 2021;3:422–40. https://doi.org/10.1038/s42254-021-00314-5.

[100] Chun S, Roy S, Nguyen YT, Choi JB, Udaykumar HS, Baek SS. Deep learning for synthetic microstructure generation in a materials-by-design framework for heterogeneous energetic materials. Sci Rep 2020;10. https://doi.org/10.1038/s41598-020-70149-0.

[101] Wei H, Wu CT, Hu W, Su T-H, Oura H, Nishi M, et al. LS-DYNA Machine Learning–Based Multiscale Method for Nonlinear Modeling of Short Fiber–Reinforced Composites. J Eng Mech 2023;149. https://doi.org/10.1061/jenmdt.emeng-6945.

[102] Kamrava S, Tahmasebi P, Sahimi M. Enhancing images of shale formations by a hybrid stochastic and deep learning algorithm. Neural Networks 2019;118:310–20. https://doi.org/10.1016/j.neunet.2019.07.009.

[103] Mao Y, He Q, Zhao X. Designing complex architectured materials with generative adversarial networks. Sci Adv 2020;6. https://doi.org/10.1126/sciadv.aaz4169.

[104] Long J, Shelhamer E, Darrell T. Fully convolutional networks for semantic segmentation. Proceedings of the IEEE Computer Society Conference on Computer Vision and Pattern Recognition, vol. 07-12- June-2015, IEEE Computer Society; 2015, p. 431–40. https://doi.org/10.1109/CVPR.2015.7298965.

[105] Chen LC, Papandreou G, Kokkinos I, Murphy K, Yuille AL. DeepLab: Semantic Image Segmentation with Deep Convolutional Nets, Atrous Convolution, and Fully Connected CRFs. IEEE Trans Pattern Anal Mach Intell 2018;40:834–48. https://doi.org/10.1109/TPAMI.2017.2699184.

[106] Arganda-carreras I, Kaynig V, Rueden C, Eliceiri KW, Schindelin J, Cardona A, et al. Trainable Weka Segmentation : a machine learning tool for microscopy pixel classification. Bioinformatics 2018;33:2424–6. https://doi.org/10.1093/bioinformatics/btx180.

[107] Smith AG, Han E, Petersen J, Olsen NAF, Giese C, Athmann M, et al. RootPainter: deep learning segmentation of biological images with corrective annotation. New Phytologist 2022;236:774–91. https://doi.org/10.1111/nph.18387.

[108] Kopp R, Joseph J, Ni X, Roy N, Wardle BL. Deep Learning Unlocks X-ray Microtomography Segmentation of Multiclass Microdamage in Heterogeneous Materials. Advanced Materials 2022;34. https://doi.org/10.1002/adma.202107817.

[109] North Thin Ply Technology. N.T.P.T. ThinPreg, 736LT Data sheet. Renens, Switzerland 2017.

[110] Mitsubishi Chemical. GRAFIL™ 34-700 12K & 24K Product Data Sheet 2017.

[111] Breite C, Melnikov A, Turon A, de Morais AB, Bourlot C Le, Maire E, et al. A synchrotron computed tomography dataset for validation of longitudinal tensile failure models based on fibre break and cluster development. Data Brief 2021;39:107590. https://doi.org/10.1016/j.dib.2021.107590.

[112] Rueden CT, Schindelin J, Hiner MC, DeZonia BE, Walter AE, Arena ET, et al. ImageJ2: ImageJ for the next generation of scientific image data. BMC Bioinformatics 2017;18:529. https://doi.org/10.1186/s12859-017-1934-z.

[113] Mehdikhani M, Breite C, Swolfs Y, Wevers M, Lomov S V., Gorbatikh L. A dataset of micro-scale tomograms of unidirectional glass fiber/epoxy and carbon fiber/epoxy composites acquired via synchrotron computed tomography during in-situ tensile loading. Data Brief 2021;34:106672. https://doi.org/10.1016/j.dib.2020.106672.

[114] Guo R, Stubbe J, Zhang Y, Schlepütz CM, Rojas C, Mehdikhani M, et al. Unpaired fast- and slow-acquisition microCT scans of carbon-fibre-reinforced composites. Zenodo 2023;1. https://doi.org/https://doi.org/10.5281/zenodo.7632124.

[115] Maire E, le Bourlot C, Adrien J, Mortensen A, Mokso R. 20 Hz X-ray tomography during an in situ tensile test. Int J Fract 2016;200:3–12. https://doi.org/10.1007/s10704-016-0077-y.

[116] Mokso R, Schlepütz CM, Theidel G, Billich H, Schmid E, Celcer T, et al. GigaFRoST: The gigabit fast readout system for tomography. J Synchrotron Radiat 2017;24:1250–9. https://doi.org/10.1107/S1600577517013522.

[117] Vo NT, Atwood RC, Drakopoulos M. Radial lens distortion correction with sub-pixel accuracy for X-ray micro-tomography. Opt Express 2015;23:32859. https://doi.org/10.1364/oe.23.032859.

[118] Marone F, Stampanoni M. Regridding reconstruction algorithm for real-time tomographic imaging. J Synchrotron Radiat 2012;19:1029–37. https://doi.org/10.1107/S0909049512032864.

[119] Karamov R, Lomov S V, Sergeichev I, Swolfs Y, Akhatov I. Inpainting micro-CT images of fibrous materials using deep learning. Comput Mater Sci 2021;197:110551. https://doi.org/10.1016/j.commatsci.2021.110551.

[120] Tauber Z, Li ZN, Drew MS. Review and preview: Disocclusion by inpainting for image-based rendering. IEEE Transactions on Systems, Man and Cybernetics Part C: Applications and Reviews 2007;37:527–40. https://doi.org/10.1109/TSMCC.2006.886967.

[121] Bertalmio M, Sapiro G, Caselles V, Ballester C. Image inpainting. Proceedings of the ACM SIGGRAPH Conference on Computer Graphics, vol. 1, 2000, p. 417–24. https://doi.org/10.1145/344779.344972.

[122] Elharrouss O, Almaadeed N, Al-Maadeed S, Akbari Y. Image inpainting: a review. Neural Process Lett 2020;51:2007–28. https://doi.org/10.1007/s11063-019-10163-0.

[123] Zhu Y, Zhao M, Li H, Zhang P. Micro-CT artifacts reduction based on detector random shifting and fast data inpainting. Med Phys 2013;40:1–14. https://doi.org/10.1118/1.4790697.

[124] Pan Y, De Carlo F, Xiao X. Ring artifact removal for micro-tomography in synchrotron radiation. Medical Imaging 2012: Physics of Medical Imaging 2012;8313:831329. https://doi.org/10.1117/12.911578.

[125] Duan X, Zhang L, Xiao Y, Cheng J, Chen Z, Xing Y. Metal artifact reduction in CT images sinogram TV inpainting. IEEE Nuclear Science Symposium Conference Record 2008:4175–7. https://doi.org/10.1109/NSSMIC.2008.4774201.

[126] Kornilov A, Safonov I, Yakimchuk I. Inpainting of Ring Artifacts on Microtomographic Images by 3D CNN. Conference of Open Innovation Association, FRUCT 2020;2020-April:200–6. https://doi.org/10.23919/FRUCT48808.2020.9087422.

[127] Salmon PL, Liu X, Sasov A. A post-scan method for correcting artefacts of slow geometry changes during micro-tomographic scans. J Xray Sci Technol 2009;17:161–74. https://doi.org/10.3233/XST-2009-0220.

[128] Barbu T. Variational image inpainting technique based on nonlinear second-order diffusions. Computers and Electrical Engineering 2016;54:345–53. https://doi.org/10.1016/j.compeleceng.2016.04.012.

[129] Patel P, Prajapati A, Mishra S. Review of Different Inpainting Algorithms. Int J Comput Appl 2012;59:30–4. https://doi.org/10.5120/9650-4411.

[130] Barnes C, Shechtman E, Finkelstein A, Goldman DB. PatchMatch: A randomized correspondence algorithm for structural image editing. ACM Trans Graph 2009;28. https://doi.org/10.1145/1531326.1531330.

[131] Wu X, Xu K, Hall P. A survey of image synthesis and editing with generative adversarial networks. Tsinghua Sci Technol 2017;22:660–74. https://doi.org/10.23919/TST.2017.8195348.

[132] Lundervold AS, Lundervold A. An overview of deep learning in medical imaging focusing on MRI. Z Med Phys 2019;29:102–27. https://doi.org/10.1016/j.zemedi.2018.11.002.

[133] McCann MT, Jin KH, Unser M. Convolutional neural networks for inverse problems in imaging: A review. IEEE Signal Process Mag 2017;34:85–95. https://doi.org/10.1109/MSP.2017.2739299.

[134] Alqahtani H, Kavakli-Thorne M, Kumar G. Applications of generative adversarial networks (GANs): An updated review. Archives of Computational Methods in Engineering 2019. https://doi.org/10.1007/s11831-019-09388-y.

[135] Criminisi A, Pérez P, Toyama K. Region filling and object removal by exemplar-based image inpainting. IEEE Transactions on Image Processing 2004;13:1200–12. https://doi.org/10.1109/TIP.2004.833105.

[136] Pathak D, Krahenbuhl P, Donahue J, Darrell T, Efros AA. Context Encoders: Feature Learning by Inpainting 2016:1–9.

[137] Jiang Y, Xu J, Yang B, Xu J, Zhu J. Image inpainting based on generative adversarial networks. IEEE Access 2020;8:22884–92. https://doi.org/10.1109/ACCESS.2020.2970169.

[138] Iizuka S, Simo-Serra E, Ishikawa H. Globally and locally consistent image completion. ACM Trans Graph 2017;36. https://doi.org/10.1145/3072959.3073659.

[139] Yeh RA, Lim TY, Chen C, Schwing AG, Hasegawa-Johnson M, Do M. Image Restoration with Deep Generative Models. ICASSP, IEEE International Conference on Acoustics, Speech and Signal Processing - Proceedings 2018;2018-April:6772–6. https://doi.org/10.1109/ICASSP.2018.8462317.

[140] Yu J, Lin Z, Yang J, Shen X, Lu X, Huang TS. Generative image inpainting with contextual attention. Proceedings of the IEEE Conference on Computer Vision and Pattern Recognition (CVPR), vol. 1, 2018, p. 5505–14. https://doi.org/10.1109/CVPR.2018.00577.

[141] Liu G, Reda FA, Shih KJ, Wang TC, Tao A, Catanzaro B. Image Inpainting for Irregular Holes Using Partial Convolutions. Lecture Notes in Computer Science (Including Subseries Lecture Notes in Artificial Intelligence and Lecture Notes in Bioinformatics) 2018;11215 LNCS:89–105. https://doi.org/10.1007/978-3-030-01252-6_6.

[142] Demir U, Unal G. Patch-Based Image Inpainting with Generative Adversarial Networks. Proceedings of the IEEE Conference on Computer Vision and Pattern Recognition (CVPR), vol. 1, 2018.

[143] Cao YJ, Jia LL, Chen YX, Lin N, Yang C, Zhang B, et al. Recent Advances of Generative Adversarial Networks in Computer Vision. IEEE Access 2019;7:14985–5006. https://doi.org/10.1109/ACCESS.2018.2886814.

[144] Xie J, Xu L, Chen E. Image denoising and inpainting with deep neural networks. Adv Neural Inf Process Syst, vol. 1, 2012, p. 341–9.

[145] Yu Y, Huang Z, Li F, Zhang H, Le X. Point Encoder GAN: A deep learning model for 3D point cloud inpainting. Neurocomputing 2020;384:192–9. https://doi.org/10.1016/j.neucom.2019.12.032.

[146] Hu W, Fu Z, Guo Z. Local frequency interpretation and non-local self-similarity on graph for point cloud inpainting. IEEE Transactions on Image Processing 2019;28:4087–100. https://doi.org/10.1109/TIP.2019.2906554.

[147] Sharma A, Grau O, Fritz M. VConv-DAE: Deep volumetric shape learning without object labels. Lecture Notes in Computer Science (including subseries Lecture Notes in Artificial Intelligence and Lecture Notes in Bioinformatics), vol. 9915 LNCS, 2016, p. 236–50. https://doi.org/10.1007/978-3-319-49409-8_20.

[148] Wang W, Huang Q, You S, Yang C, Neumann U. Shape Inpainting Using 3D Generative Adversarial Network and Recurrent Convolutional Networks. Proceedings of the IEEE International Conference on Computer Vision, vol. 2017- Octob, 2017, p. 2317–25. https://doi.org/10.1109/ICCV.2017.252.

[149] Jain AK, Mao J, Mohiuddin KM. Artificial neural networks: A tutorial. Computer (Long Beach Calif) 1996;29:31–44. https://doi.org/10.1109/2.485891.

[150] Hirose Y, Yamashita K, Hijiya S. Back-propagation algorithm which varies the number of hidden units. Neural Networks 1991;4:61–6. https://doi.org/10.1016/0893-6080(91)90032-Z.

[151] Kingma DP, Ba J. Adam: A Method for Stochastic Optimization. 3rd International Conference on Learning Representations, ICLR 2015 - Conference Track Proceedings 2014:1–15.

[152] Zhao ZQ, Zheng P, Xu ST, Wu X. Object detection with deep learning: A review. IEEE Trans Neural Netw Learn Syst 2019;30:3212–32. https://doi.org/10.1109/TNNLS.2018.2876865.

[153] Le Q v. A tutorial on deep learning part 2: Autoencoders, convolutional neural networks and recurrent neural networks. Google Brain 2015:1–20.

[154] Talathi SS, Vartak A. Improving performance of recurrent neural network with relu nonlinearity 2015.

[155] Kim HJ, Lee JS, Yang HS. Human action recognition using a modified convolutional neural network. Lecture Notes in Computer Science (Including Subseries Lecture Notes in Artificial Intelligence and Lecture Notes in Bioinformatics) 2007;4492 LNCS:715–23. https://doi.org/10.1007/978-3-540-72393-6_85.

[156] Xu L, Ren JSJ, Liu C, Jia J. Deep convolutional neural network for image deconvolution. Adv Neural Inf Process Syst 2014;2:1790–8.

[157] Goodfellow IJ, Pouget-Abadie J, Mirza M, Xu B, Warde-Farley D, Ozair S, et al. Generative Adversarial Networks. Commun ACM 2014;63:139–44. https://doi.org/10.5555/2969033.2969125.

[158] Gui J, Sun Z, Wen Y, Tao D, Ye J. A review on generative adversarial networks: Algorithms, theory, and applications 2020;14:1–28.

[159] Wang X, Xu D, Gu F. 3D Model Inpainting Based on 3D Deep Convolutional Generative Adversarial Network. IEEE Access 2020;8:170355–63. https://doi.org/10.1109/access.2020.3024288.

[160] Xu B, Wang N, Chen T, Li M. Empirical Evaluation of Rectified Activations in Convolutional Network 2015.

[161] Ioffe S, Szegedy C. Batch Normalization: Accelerating Deep Network Training by Reducing Internal Covariate Shift. 32nd International Conference on Machine Learning, ICML 2015 2015;1:448–56.

[162] Yu F, Koltun V. Multi-Scale Context Aggregation by Dilated Convolutions. 4th International Conference on Learning Representations, ICLR 2016 - Conference Track Proceedings 2015.

[163] Wu J, Zhang C, Xue T, Freeman WT, Tenenbaum JB. Learning a Probabilistic Latent Space of Object Shapes via 3D Generative-Adversarial Modeling. Adv Neural Inf Process Syst 2016:82–90.

[164] Karamov R, Martulli LM, Kerschbaum M, Sergeichev I, Swolfs Y, Lomov S V. Micro-CT based structure tensor analysis of fibre orientation in random fibre composites versus high-fidelity fibre identification methods. Compos Struct 2020;235:111818. https://doi.org/10.1016/j.compstruct.2019.111818.

[165] Denos BR, Sommer DE, Favaloro AJ, Pipes RB, Avery WB. Fiber orientation measurement from mesoscale CT scans of prepreg platelet molded composites. Compos Part A Appl Sci Manuf 2018;114:241–9. https://doi.org/10.1016/j.compositesa.2018.08.024.

[166] Pinter P, Dietrich S, Bertram B, Kehrer L, Elsner P, Weidenmann KA. Comparison and error estimation of 3D fibre orientation analysis of computed tomography image data for fibre reinforced composites. NDT and E International 2018;95:26–35. https://doi.org/10.1016/j.ndteint.2018.01.001.

[167] Krause M, Hausherr JM, Burgeth B, Herrmann C, Krenkel W. Determination of the fibre orientation in composites using the structure tensor and local X-ray transform. J Mater Sci 2010;45:888–96. https://doi.org/10.1007/s10853-009-4016-4.

[168] Nelson LJ, Smith RA, Mienczakowski M. Ply-orientation measurements in composites using structure-tensor analysis of volumetric ultrasonic data. Compos Part A Appl Sci Manuf 2018;104:108–19. https://doi.org/10.1016/j.compositesa.2017.10.027.

[169] Advani SG, Tucker CL. The Use of Tensors to Describe and Predict Fiber Orientation in Short Fiber Composites. J Rheol (N Y N Y) 1987;31:751–84. https://doi.org/10.1122/1.549945.

[170] Jionghao W. UU-Nets Connecting Discriminator and Generator for Image to Image Translation. ArXiv 2019.

[171] Wang Z, She Q, Ward TE. Generative Adversarial Networks in Computer Vision. ACM Comput Surv 2021;54:1–38. https://doi.org/10.1145/3439723.

[172] Jianchao Yang, Wright J, Huang TS, Yi Ma. Image Super-Resolution Via Sparse Representation. IEEE Transactions on Image Processing 2010;19:2861–73. https://doi.org/10.1109/TIP.2010.2050625.

[173] Badel P, Vidal-Sallé E, Maire E, Boisse P. Simulation and tomography analysis of textile composite reinforcement deformation at the mesoscopic scale. Compos Sci Technol 2008;68:2433–40. https://doi.org/10.1016/j.compscitech.2008.04.038.

[174] Amenabar I, Mendikute A, López-Arraiza A, Lizaranzu M, Aurrekoetxea J. Comparison and analysis of non-destructive testing techniques suitable for delamination inspection in wind turbine blades. Compos B Eng 2011;42:1298–305. https://doi.org/10.1016/j.compositesb.2011.01.025.

[175] Centea T, Hubert P. Measuring the impregnation of an out-of-autoclave prepreg by micro-CT. Compos Sci Technol 2011;71:593–9. https://doi.org/10.1016/j.compscitech.2010.12.009.

[176] Schilling PJ, Karedla BPR, Tatiparthi AK, Verges MA, Herrington PD. X-ray computed microtomography of internal damage in fiber reinforced polymer matrix composites. Compos Sci Technol 2005;65:2071–8. https://doi.org/10.1016/j.compscitech.2005.05.014.

[177] Maire E, Withers PJ. Quantitative X-ray tomography. International Materials Reviews 2014;59:1–43. https://doi.org/10.1179/1743280413Y.0000000023.

[178] Wu SC, Xiao TQ, Withers PJ. The imaging of failure in structural materials by synchrotron radiation X-ray microtomography. Eng Fract Mech 2017;182:127–56. https://doi.org/10.1016/j.engfracmech.2017.07.027.

[179] Scott AE, Mavrogordato M, Wright P, Sinclair I, Spearing SM. In situ fibre fracture measurement in carbon-epoxy laminates using high resolution computed tomography. Compos Sci Technol 2011;71:1471–7. https://doi.org/10.1016/j.compscitech.2011.06.004.

[180] Li P, Li Z, Pang X, Wang H, Lin W, Wu W. Multi-scale residual denoising GAN model for producing super-resolution CTA images. J Ambient Intell Humaniz Comput 2022;13:1515–24. https://doi.org/10.1007/s12652-021-03009-y.

[181] You C, Cong W, Vannier MW, Saha PK, Hoffman EA, Wang G, et al. CT Super-Resolution GAN Constrained by the Identical, Residual, and Cycle Learning Ensemble (GAN-CIRCLE). IEEE Trans Med Imaging 2020;39:188–203. https://doi.org/10.1109/TMI.2019.2922960.

[182] Gu Y, Zeng Z, Chen H, Wei J, Zhang Y, Chen B, et al. MedSRGAN: medical images super-resolution using generative adversarial networks. Multimed Tools Appl 2020;79:21815–40. https://doi.org/10.1007/s11042-020-08980-w.

[183] Song TA, Chowdhury SR, Yang F, Dutta J. PET image super-resolution using generative adversarial networks. Neural Networks 2020;125:83–91. https://doi.org/10.1016/j.neunet.2020.01.029.

[184] Wang X, Yu K, Wu S, Gu J, Liu Y, Dong C, et al. ESRGAN: Enhanced Super-Resolution Generative Adversarial Networks. Computer Vision – ECCV 2018 Workshops ECCV 2018 2019:63–79. https://doi.org/10.1007/978-3-030-11021-5_5.

[185] Zhu J-Y, Park T, Isola P, Efros AA. Unpaired Image-to-Image Translation Using Cycle-Consistent Adversarial Networks. 2017 IEEE International Conference on Computer Vision (ICCV) 2017:2242–51. https://doi.org/10.1109/ICCV.2017.244.

[186] Park J, Hwang D, Kim KY, Kang SK, Kim YK, Lee JS. Computed tomography super-resolution using deep convolutional neural network. Phys Med Biol 2018;63. https://doi.org/10.1088/1361-6560/aacdd4.

[187] Zhang Y, Noack MA, Vagovic P, Fezzaa K, Garcia-Moreno F, Ritschel T, et al. PhaseGAN: A deep-learning phase-retrieval approach for unpaired datasets 2020. https://doi.org/10.1364/OE.423222.

[188] Wang Y, Teng Q, He X, Feng J, Zhang T. CT-image of rock samples super resolution using 3D convolutional neural network. Comput Geosci 2019;133. https://doi.org/10.1016/j.cageo.2019.104314.

[189] Jolicoeur-Martineau A. The relativistic discriminator: a key element missing from standard GAN 2018.

[190] Arjovsky M, Chintala S, Bottou L. Wasserstein GAN 2017.

[191] Micikevicius P, Narang S, Alben J, Diamos G, Elsen E, Garcia D, et al. Mixed Precision Training 2017.

[192] Greeshma MS, Bindu VR. Super-resolution Quality Criterion (SRQC): a super-resolution image quality assessment metric. Multimed Tools Appl 2020;79:35125–46. https://doi.org/10.1007/s11042-020-09352-0.

[193] Wang Z, Simoncelli EP, Bovik AC. Multi-scale structural similarity for image quality assessment. Conference Record of the Asilomar Conference on Signals, Systems and Computers, vol. 2, 2003, p. 1398–402. https://doi.org/10.1109/acssc.2003.1292216.

[194] Lucas AM, Ryder P V., Li B, Cimini BA, Eliceiri KW, Carpenter AE. Open-source deep-learning software for bioimage segmentation. Mol Biol Cell 2021;32:823–9. https://doi.org/10.1091/MBC.E20-10-0660.

[195] Weigert M, Schmidt U, Boothe T, Müller A, Dibrov A, Jain A, et al. Content-aware image restoration: pushing the limits of fluorescence microscopy. Nat Methods 2018;15:1090–7. https://doi.org/10.1038/s41592-018-0216-7.

[196] Segal MR. Machine Learning Benchmarks and Random Forest Regression. Biostatistics 2004:1–14.

[197] Manilich EA, Özsoyoğlu ZM, Trubachev V, Radivoyevitch T. Classification of large microarray datasets using fast random forest construction. J Bioinform Comput Biol 2011;9:251–67. https://doi.org/10.1142/S021972001100546X.

[198] Ronneberger O, Fischer P, Brox T. U-Net: Convolutional Networks for Biomedical Image Segmentation. Proceedings, Part III Medical Image Computing and Computer-Assisted Intervention-MICCAI 2015.

[199] Jane M, Bjorholm A, Andersen V. General rights Insegt Fibre: a user-friendly software for individual fibre segmentation. Downloaded from orbit.dtu.dk on, vol. 14, n.d., p. 2022.

[200] Tyrus JM, Gosz M, DeSantiago E. A local finite element implementation for imposing periodic boundary conditions on composite micromechanical models. Int J Solids Struct 2007;44:2972–89. https://doi.org/10.1016/j.ijsolstr.2006.08.040.

[201] Azhar Kamarudin K, Emran Ismail A. Periodic Boundary Condition Technique on Carbon Fibre Composites. J Phys Conf Ser, vol. 914, Institute of Physics Publishing; 2017. https://doi.org/10.1088/1742-6596/914/1/012045.

[202] Zinchenko AZ. Algorithm for random close packing of spheres with periodic boundary conditions. J Comput Phys 1994;114:298–307. https://doi.org/10.1006/jcph.1994.1168.

[203] Lomov S V. Mechanics of heterogeneous media IV . Asymptotic homogenisation in periodic media. 1989.

[204] Garoz D, Gilabert FA, Sevenois RDB, Spronk SWF, Van Paepegem W. Consistent application of periodic boundary conditions in implicit and explicit finite element simulations of damage in composites. Compos B Eng 2019;168:254–66. https://doi.org/10.1016/j.compositesb.2018.12.023.

[205] Wu W, Owino J, Al-Ostaz A, Cai L. Applying Periodic Boundary Conditions in Finite Element Analysis. n.d.

[206] Omairey SL, Dunning PD, Sriramula S. Development of an ABAQUS plugin tool for periodic RVE homogenisation. Eng Comput 2019;35:567–77. https://doi.org/10.1007/s00366-018-0616-4.

[207] Drugan WJ, Willis JR. A micromechanics-based nonlocal constitutive equation and estimates of representative volume element size for elastic composites. J Mech Phys Solids 1996;44:497–524. https://doi.org/10.1016/0022-5096(96)00007-5.

[208] Gitman IM, Askes H, Sluys LJ. Representative volume: Existence and size determination. Eng Fract Mech 2007;74:2518–34. https://doi.org/10.1016/j.engfracmech.2006.12.021.

[209] Khisaeva ZF, Ostoja-Starzewski M. On the size of RVE in finite elasticity of random composites. J Elast 2006;85:153–73. https://doi.org/10.1007/s10659-006-9076-y.

[210] ABAQUS/Standard User's Manual, Version 6.18 2018.

[211] Tabatabaei SA, Lomov S V. Eliminating the volume redundancy of embedded elements and yarn interpenetrations in meso-finite element modelling of textile composites. Comput Struct 2015;152:142–54. https://doi.org/10.1016/j.compstruc.2015.02.014.

[212] Karamov R, Breite C, Lomov S V., Sergeichev I, Swolfs Y. Super-resolution processing of synchrotron CT images for automated fibre break analysis of unidirectional composites. Polymers (in Submission) 2023.

[213] Tavares RP, Otero F, Baiges J, Turon A, Camanho PP. A dynamic spring element model for the prediction of longitudinal failure of polymer composites. Comput Mater Sci 2019;160:42–52. https://doi.org/10.1016/j.commatsci.2018.12.048.

[214] Guerrero JM, Mayugo JA, Costa J, Turon A. A 3D Progressive Failure Model for predicting pseudo-ductility in hybrid unidirectional composite materials under fibre tensile loading. Compos Part A Appl Sci Manuf 2018;107:579–91. https://doi.org/10.1016/j.compositesa.2018.02.005.

[215] Pimenta S. A computationally-efficient hierarchical scaling law to predict damage accumulation in composite fibre-bundles. Compos Sci Technol 2017;146:210–25. https://doi.org/10.1016/j.compscitech.2017.04.018.

[216] Swolfs Y, Verpoest I, Gorbatikh L. Issues in strength models for unidirectional fibre-reinforced composites related to Weibull distributions, fibre packings and boundary effects. Compos Sci Technol 2015;114:42–9. https://doi.org/10.1016/j.compscitech.2015.04.002.

[217] Swolfs Y, Fazlali B, Melnikov A, Mesquita F, Feyen V, Breite C, et al. State-of-the-art models for mechanical performance of carbon-glass hybrid composites in wind turbine blades. IOP Conf Ser Mater Sci Eng 2020;942:012005. https://doi.org/10.1088/1757-899X/942/1/012005.

[218] Mehdikhani M, Breite C, Swolfs Y, Wevers M, Lomov S V., Gorbatikh L. Combining digital image correlation with X-ray computed tomography for characterization of fiber orientation in unidirectional composites. Compos Part A Appl Sci Manuf 2021;142. https://doi.org/10.1016/j.compositesa.2020.106234.

[219] Stehman S V. Selecting and interpreting measures of thematic classification accuracy. Remote Sens Environ 1997;62:77–89. https://doi.org/10.1016/S0034-4257(97)00083-7.